



University of Kentucky  
UKnowledge

---

University of Kentucky Doctoral Dissertations

Graduate School

---

2009

## SPECIFIC HEAT MEASUREMENTS ON STRONGLY CORRELATED ELECTRON SYSTEMS

Vijayalakshmi Varadarajan  
*University of Kentucky*, [vijayavarada@gmail.com](mailto:vijayavarada@gmail.com)

[Right click to open a feedback form in a new tab to let us know how this document benefits you.](#)

---

### Recommended Citation

Varadarajan, Vijayalakshmi, "SPECIFIC HEAT MEASUREMENTS ON STRONGLY CORRELATED ELECTRON SYSTEMS" (2009). *University of Kentucky Doctoral Dissertations*. 805.  
[https://uknowledge.uky.edu/gradschool\\_diss/805](https://uknowledge.uky.edu/gradschool_diss/805)

This Dissertation is brought to you for free and open access by the Graduate School at UKnowledge. It has been accepted for inclusion in University of Kentucky Doctoral Dissertations by an authorized administrator of UKnowledge. For more information, please contact [UKnowledge@lsv.uky.edu](mailto:UKnowledge@lsv.uky.edu).

ABSTRACT OF DISSERTATION

Vijayalakshmi Varadarajan

The Graduate School  
University of Kentucky  
2009

SPECIFIC HEAT MEASUREMENTS ON STRONGLY CORRELATED ELECTRON  
SYSTEMS

---

ABSTRACT OF DISSERTATION

---

A dissertation submitted in partial fulfillment of the  
requirements for the degree of Doctor of Philosophy  
in the Department of Physics and Astronomy  
at the University of Kentucky

By

Vijayalakshmi Varadarajan

Lexington, Kentucky

Director: Dr. Joseph W. Brill, Professor of Physics

Lexington, Kentucky

2009

Copyright © Vijayalakshmi Varadarajan 2009

## ABSTRACT OF DISSERTATION

### SPECIFIC HEAT MEASUREMENTS ON STRONGLY CORRELATED ELECTRON SYSTEMS

Studies on strongly correlated electron systems over decades have allowed physicists to discover unusual properties such as spin density waves, ferromagnetic and antiferromagnetic states with unusual ordering of spins and orbitals, and Mott insulating states, to name a few.

In this thesis, the focus will be on the specific heat property of these materials exhibiting novel electronic ground states in the presence and absence of a field. The purpose of these measurements is to characterize the phase transitions into these states and the low energy excitations in these states. From measurements at the phase transitions, one can learn about the amount of order involved [i.e. entropy:  $\Delta S = \int \Delta c_p / T dT$ ], while measurements at low temperatures illuminate the excitation spectrum. In order to study the thermodynamic properties of the materials at their phase transitions, a high sensitive technique, ac-calorimetry was used. The ac-calorimeter, workhorse of our low dimensional materials lab, is based on modulating the power that heats the sample and measuring the temperature oscillations of the sample around its mean value. The in-house ac-calorimetry set up in our lab has the capability to produce a quasi-continuous readout of heat capacity as a function of temperature. A variety of single crystals were investigated using this technique and a few among them are discussed in my thesis.

Since many of the crystals that are studied by our group are magnetically active, it becomes useful for us to also study them in the presence of a moderate to high magnetic field. This motivated me to design, develop, and build a heat capacity probe that would

enable us to study the crystals in the presence of non-zero magnetic fields and at low temperatures. The probe helped us not only to revisit some of the studied materials and to draw firm conclusions on the previous results but also is vital in exploring the untouched territory of novel materials at high magnetic fields ( $\sim 14$  T).

**Keywords:** specific heat, ac-calorimetry, strongly correlated electrons, entropy, magnetic field

Vijayalakshmi Varadarajan

09/15/2009

SPECIFIC HEAT MEASUREMENTS ON STRONGLY CORRELATED ELECTRON  
SYSTEMS

By

Vijayalakshmi Varadarajan

Dr. Joseph W Brill

---

(Director of Dissertation)

Dr. Joseph W Brill

---

(Director of Graduate Studies)

09/15/2009

---

(Date)

## RULES FOR THE USE OF DISSERTATIONS

Unpublished dissertations submitted for the Doctor's degree and deposited in the University of Kentucky Library are as a rule open for inspection, but are to be used only with due regard to the rights of the authors. Bibliographical references may be noted, but quotations or summaries of parts may be published only with the permission of the author, and with the usual scholarly acknowledgements.

Extensive copying or publication of the thesis in whole or in part also requires the consent of the Dean of the Graduate School of the University of Kentucky.

A library that borrows this thesis for use by its patrons is expected to secure the signature of each user.

Name

Date

---

---

---

---

---

---

---

---

---

---

DISSERTATION

Vijayalakshmi Varadarajan

The Graduate School  
University of Kentucky  
2009



SPECIFIC HEAT MEASUREMENTS ON STRONGLY CORRELATED ELECTRON  
SYSTEMS

---

DISSERTATION

---

A dissertation submitted in partial fulfillment of the  
requirements for the degree of Doctor of Philosophy  
in the Department of Physics and Astronomy  
at the University of Kentucky

By

Vijayalakshmi Varadarajan

Lexington, Kentucky

Director: Dr. Joseph W. Brill, Professor of Physics

Lexington, Kentucky

2009

Copyright © Vijayalakshmi Varadarajan 2009

## DEDICATION

To my Parents Mr. S. Varadarajan and Mrs. V. Rajalakshmi and for all their support,  
guidance and encouragement

To my Late Uncle Mr. S. Venguswamy and Aunt Mrs. V. Vasantha for their  
unconditional love and support

To my husband Mr. L. Ganeshkumar for his indulgent love and encouragement

## ACKNOWLEDGEMENTS

I would like to thank all the people who have helped and inspired me during my doctoral study. Foremost, I would like to express my sincere gratitude to my advisor Prof. Joseph. W. Brill for his continuous support towards my Ph.D research. His perpetual energy and enthusiasm in research is a source of inspiration for me. He is always accessible and willing to help me with my research and offered emotional support during tough times; as a result research life is always smooth and rewarding for me. I also thank him for all the financial assistance that he bestowed me with during my three years of research. I am indebted to him more than he knows.

I am grateful to Dr. Gang Cao for his immense professional support. I wish to thank him for providing crystals for my research and allowing me to use the Liquid Helium Dewar with 14 T magnet in his laboratory for my measurements. His role as a Ph.D Advisory Committee member and as our collaborator is irreplaceable and I am much indebted to him for his valuable advice in science discussion and teaching.

I gratefully thank my Ph.D Advisory Committee member, Dr.Kwok-Wai Ng for the discussions I had with him, both in-class and informal, which inculcated the fundamentals of condensed matter theory. I would like to extend my thanks to Dr. J. P. Selegue for serving as an active member in my Ph.D Advisory Committee.

It is a pleasure to thank my collaborators Dr. Angst Manuel, Dr. Micheal McGuire and Dr. David Mandrus from the Oak Ridge National Laboratory for providing crystals for my research. Special thanks to Dr. Wolfgang Korsch for providing me with the Gaussmeter and Dr. Martin for the scientific discussions. I would like to thank Dr. Nancy Levenson, Dr. Marcus McEllistrem and Dr. Steve Yates for their support and guidance during my initial years of the Ph.D program.

My research would not have been possible at the first place without the exclusive support from the academic committee that played a role in my admission to the Graduate school. In particular, I owe a great deal to Dr. Tim Gorringer and Dr. Suketu Bhavsar for all their help during my admission.

I wish to acknowledge the help I got from the technical staff in the machine shop and the electronics shop. I would like to express my thanks particularly to Mr. James Morris for building the specific heat probe for field measurements, Mr. Herb Mefford for

building the probe for zero field measurements. The probe would not have existed without them. I am thankful to Mr. Gene Baber for his assistance with vacuum testing and prompt cryogenic fluid refill. I thank Mr. Bill Fuqua from the electronic shop for his timely help. Many thanks to Mr. Greg Porter for helping me with the BASIC program.

This thesis would never have become a reality without the help and suggestions of many supportive friends and colleagues. In this point of view, my biggest thanks should go to Dr. Vinobalan Durairaj, who was a source of inspiration for me to join the Ph.D program. I owe a great deal for all his help, suggestions and scientific discussions and particularly thank him for exploring with me the boundaries of professional friendship. Thanks to Shalinee Chikara, Dr. Xiunu Lin, Dr. Luis Ladino and Mr. Oleksandr Korneta for their cooperation, who helped me in one way or the other on the technical side of my research.

I convey special thanks to Mrs. Eva Ellis from the department office in dealing with the helium order complications and wish to acknowledge the administrative help I got from Laurie, Joanna, Sharon, Emily, Rick, Carol, Sarah and Diane.

My parents, Mr. Varadarajan Sundaram and Mrs. Rajalakshmi Varadarajan deserve a special mention for their perpetual support, blessings, motivation and encouragement. My due respects to my Uncle, (Late) Mr. Venguswamy Sundaram and Aunt Vasantha Venguswamy for showering me with their love and affection and showing me the joy of intellectual pursuit ever since I was a child. Thanks to my brother Ganeshkumar Varadarajan for being very supportive and caring. Words fail me to express my appreciation to my husband Ganeshkumar whose dedication, love and persistent confidence in me, has taken the load off my shoulder.

Finally I would like to thank National Science Foundation for making all our projects possible. To all the above individuals and several colleagues whose name I cannot continue listing and who have assisted me in one way or another, I feel very much indebted.

## TABLE OF CONTENTS

Acknowledgements.....	iii
List of Tables.....	ix
List of Figures.....	x
Chapter One: Introduction	1
Chapter Two: Theory	7
2.1 Introduction	7
2.1.1 Heat Capacity	7
2.1.2 Lattice specific heat	7
2.1.3 Electronic specific heat	9
2.1.4 Specific heat at a first order phase transition	9
2.1.5 Specific heat at a second order (continuous) phase transition	10
2.1.6 Magnetic specific heat	12
2.2 Theory of Magnetic interactions and ordering	13
2.2.1 Exchange interaction and ordering	13
2.2.2 Spin-Density Waves (SDW)	20
2.2.3 Mean Field calculation of specific heat on ferromagnets	21
2.2.4 The role of fluctuations	23
Chapter Three: AC-calorimetry Technique	26
3.1 Method of ac technique and its measuring conditions	26
3.2 Determination of Proper Chopping Frequency	32
Chapter Four: Experimental setup for measurement in the presence of magnetic field	34
4.1 Introduction	34
4.2 Apparatus	34
4.2(a) In zero magnetic field	34
4.2(b) In magnetic field	35
4.2.1 The Cryostat	35
4.2.2 The Variable Temperature Insert	35
4.2.3 Liquid Helium Meter	38

4.2.4	The Superconducting magnet	38
4.2.5	Sample Chamber	42
4.2.6	Sample setting	42
4.2.7	Temperature Controller	45
4.2.8	Basic Operation	45
4.2.9	Test Run	45
4.3	Thermometry	46
4.3.1	Temperature sensors for thermal bath	46
4.3.1(a)	In zero magnetic field	46
4.3.1(b)	In magnetic field	46
4.3.2	Temperature sensors for dc offset and ac temperature	48
4.3.2(a)	In zero magnetic field	48
4.3.2(b)	In magnetic field	49
4.3.3	Calibration of Cernox sensor	50
4.4	Addendum correction	50
4.5	Sources of heating, pick-up and noise	51
4.6	Challenges involved in the design and operation of the probe for the in-field setup	52
Chapter Five: Specific heat measurements in Zero magnetic field		54
5.1	Introduction	54
5.2	Specific heat of $(\text{Ca}_{1-x}\text{Sr}_x)_3\text{Ru}_2\text{O}_7$ single crystals	54
5.2.1	The physical properties of $\text{Ca}_3\text{Ru}_2\text{O}_7$	55
5.2.2	Motivation	57
5.2.3	Sample preparation	57
5.2.4	Magnetization data	59
5.2.5	Specific heat measurements	63
5.2.6	Results and Discussion	63
5.3	Specific heat of $\text{Fe}_2\text{OBO}_3$ crystals	68
5.3.1	The physical properties of $\text{Fe}_2\text{OBO}_3$	68
5.3.2	Motivation	69
5.3.3	Sample preparation and data	69

5.3.4 Results and Discussion	73
5.4 Conclusion	77
Chapter Six: Specific heat measurements in magnetic field	79
6.1. Introduction	79
6.2 Specific heat measurements on $\text{Sr}_4\text{Ru}_3\text{O}_{10}$	79
6.2.1 The physical properties of $\text{Sr}_4\text{Ru}_3\text{O}_{10}$	79
6.2.2 Motivation	81
6.2.3 Sample preparation and characterization	83
6.2.4 Magnetic susceptibility data	83
6.2.5 Zero field heat capacity data	84
6.2.5 (a) <i>c</i> -axis sample at the magnetic transition	84
6.2.5 (b) <i>ab</i> -plane sample at the magnetic transition	89
6.2.5 (c) <i>c</i> -axis and <i>ab</i> -plane sample at low temperature	92
6.2.6 Discussion	92
6.3 Specific heat measurements on $\text{LaFeAsO}$	94
6.3.1 The physical properties of $\text{LaFeAsO}$	94
6.3.2 Motivation	95
6.3.3 Sample preparation and characterization	96
6.3.4 Heat capacity data	97
6.3.5 Results and Discussion	100
6.4 Conclusion	108
Chapter Seven: Specific heat measurements on other Fe-As based systems	110
7.1 Introduction	110
7.2 SDW transition in $\text{PrFeAsO}$	111
7.2.1 The physical properties of $\text{PrFeAsO}$	111
7.2.2 Motivation	112
7.2.3 Sample preparation	112
7.2.4 Heat capacity data	112
7.2.5 Results and Discussion	114
7.3 Superconducting transition in $\text{SrFe}_{1.8}\text{Co}_{0.2}\text{As}_2$	117
7.3.1 The Physical properties of $\text{SrFe}_{1.8}\text{Co}_{0.2}\text{As}_2$	117

7.3.2 Motivation	117
7.3.3 Heat capacity data	117
7.3.4 Results and Discussion	119
7.4 Conclusion	121
Chapter Eight: Concluding Remarks	122
References.....	125
Vita.....	132



## LIST OF TABLES

Table 4.1  $\Delta T/T(\%)$  for Cernox 1050 temperature sensor at B (Tesla)

Table 4.2  $\Delta T/T(\%)$  for Type E thermocouples at B (Tesla)

LIST OF FIGURES

Figure 2.1 Illustration of (a) direct exchange (b) superexchange (c) indirect exchange.....16

Figure 2.2 A schematic representation of Superexchange in Transition Metal Oxides (TMO's).  $B^{n+}$  is the transition metal ion and  $O^{2-}$  is the Oxygen ion.....17

Figure 2.3 A schematic representation of exchange interaction favoring hopping if (a) neighboring ions are ferromagnetically aligned and not if (b) neighboring ions are antiferromagnetically aligned.....18

Figure 3.1 A schematic representation of a one dimensional heat flow situation when the sample is surrounded by helium gas..... 27

Figure 3.2 A schematic representation of the sample setting with thermocouple.....28

Figure 3.3 A schematic representation of ac temperature oscillation in the presence of a latent heat..... 31

Figure 4.1 Schematic of liquid nitrogen/helium glass Dewar..... 36

Figure 4.2 Schematic of the ac-alorimeter.....37

Figure 4.3 Schematic of a Vapo shield liquid helium Dewar..... 39

Figure 4.4 Schematic of the top portion of the Variable temperature insert (VTI).....40

Figure 4.5 Schematic of the Variable Temperature insert (VTI) that includes the sample space, inner vacuum space (IVC, inside the sample space) and radiation shield.....41

Figure 4.6 A schematic of the header designed for in-field setup..... 43

Figure 4.7 Sample setting with cernox sensor.....	44
Figure 4.8 The calibration curve of the Cernox (CX-1050-LR-1.4D) thermometer used as a temperature sensor for the thermal bath in the newly built header.....	47
Figure 4.9 A $\log T - \log R$ plot of the cernox (CX-1050-LR-1.4D) thermometer used as a temperature sensor for the thermal bath in the newly built header.....	48
Figure 4.10 Two chromel / constantan wires attached to Cernox sensor (S) by silver paint.....	50
Figure 5.1 (a) Crystal structure of $\text{Ca}_3\text{Ru}_2\text{O}_7$ , projected along the $c$ axis (top figure) and the $ab$ plane (bottom figure) (b) The TEM image depicts the double layered nature of the compound (c) Electron diffraction image reveals the anisotropic nature within the basal plane of $\text{Ca}_3\text{Ru}_2\text{O}_7$ .....	56
Figure 5.2 Temperature dependence of the magnetic moments (per formula unit) for the pure and strontium-substituted samples near the phase transitions with fields (0.5T) applied along the $a$ - axis and $b$ -axis.....	58
Figure 5.3 $fV_{AC}$ vs. $f$ curve for 0.36 mg $\text{Ca}_3\text{Ru}_2\text{O}_7$ sample at (a) $T = 295$ K (b) $T = 50$ K.....	60
Figure 5.4 $fV_{AC}$ vs. $f$ curve for 0.78 mg $\text{Ca}_3\text{Ru}_2\text{O}_7$ sample at (a) $T = 295$ K (b) $T = 100$ K.....	61
Figure 5.5 (a) The overall temperature dependence of specific heat, normalized to the gas constant $R = 8.31 \text{ J mol}^{-1} \text{ K}^{-1}$ , of $(\text{Ca}_{1-x}\text{Sr}_x)_3\text{Ru}_2\text{O}_7$ crystals measured with ac-calorimetry (solid curves); data for the $x = 0.15$ and $x = 0.58$ samples are vertically offset by 10 and 20 units, respectively. The open symbols show the PPMS results for the pure sample. (b)	

Enlargement of the low temperature specific heat, plotted as  $C_p /RT$  vs  $T^2$  for the same samples.....62

Figure 5.6 Effective specific heat (including distributed latent heat) for the pure samples, near the  $T_c$  structural transition, measured with different frequencies (ac-calorimetry) or temperature steps (PPMS measurements), as indicated.....64

Figure 5.7 Specific heats of the pure samples near their Neel transitions. The dashed line for the 0.36 mg sample shows the background used to estimate the change in entropy..66

Figure 5.8 Specific heat, measured with ac-calorimetry, of pure and Sr-substituted samples, near the phase transitions. Data for the  $x = 0.15$  and  $x = 0.58$  samples are vertically offset by  $0.4 \text{ K}^{-1}$  and  $0.8 \text{ K}^{-1}$ , respectively. The dashed lines show the extrapolated temperature dependences and background used to estimate the changes in specific heats (shown by the heavy vertical lines) and entropy, respectively, for the substituted samples as discussed in the section.....67

Figure 5.9 Crystal structure of  $\text{Fe}_2\text{OBO}_3$ . The unit cell is orthorhombic at high temperature. Structurally distinct  $\text{Fe}_{\text{I,II}}\text{O}_6$  octahedra build ( $\text{Fe}_{\text{II}}\text{-Fe}_{\text{I}}\text{-Fe}_{\text{I}}\text{-Fe}_{\text{II}}$  in the  $b$ - $c$  plane) ribbons of edge-sharing chains in the  $a$  direction.....68

Figure 5.10 Frequency dependence of the ac voltage for 0.31mg sample.....70

Figure 5.11 Specific heat of  $\text{Fe}_2\text{OBO}_3$  ( $m = 0.31\text{mg}$ ) over the entire measured temperature range in the units of  $R$  .....71

Figure 5.12 (a) Specific heat of  $\text{Fe}_2\text{OBO}_3$  ( $m = 0.31\text{mg}$ ) near the magnetic transition ( $T = 153 \text{ K}$ ) (b) Specific heat of the sample near the structural transition ( $T = 340 \text{ K}$ ).....72

Figure 5.13 (a) Temperature dependence of resistivity  $\rho$  along  $a$  indicating two phase transitions (b) heat flow of differential scanning calorimetry (c) estimated monoclinic

angle  $\beta$  (d) key parameters describing the Mossbauer spectra : fraction of the contribution to the spectra by Fe ions with no discernible electron hopping (■, left) and hopping frequency  $\nu$  of the remainder (○, right). Inset in (a) Crystal structure at 355 K..... 74

Figure 5.14 Specific heat of  $\text{Fe}_2\text{OBO}_3$  ( $m = 0.31\text{mg}$ ) single crystal between 260-320K showing no anomaly in (280/310 K) region..... 75

Figure 5.15 (a) The 2D lattice of chains consists of two sublattices offset from each other by  $a/2$ .  $\text{Fe}^{3+}$  and  $\text{Fe}^{2+}$  are drawn as filled and open circles respectively. Note that half the ion sites (e.g. sites II and IV on the bottom) remain intermediate valence and are not shown. Degeneracy of the two configurations leads to domain formation, with opposite sense of monoclinic distortion [41]. (b) Alternative “zigzag” CO with only slightly higher energy than the diagonal ground state. All other configurations are intermediate between diagonal and zigzag..... 76

Figure 6.1 Crystal structure of  $\text{Sr}_4\text{Ru}_3\text{O}_{10}$  projected along the  $c$  axis.....80

Figure 6.2 Specific heat divided by temperature ( $C/T$ ), as a function of  $T$  for (a)  $B // ab$  plane. (b)  $B // c$  axis (c)  $C/T$  for  $B // ab$  plane as a function of  $T^2$  for  $0 \leq B \leq 5T$ ; inset 1 shows  $C/T$  for  $B // a$  plane vs  $T$  for few representative fields; inset 2 shows  $C/T$  for  $B // ab$  plane vs  $T^2$  for  $5 \leq B \leq 9T$ ..... 82

Figure 6.3 Magnetization as a function of temperature for the  $c$ -axis and  $ab$ -plane at  $B = 0.01 T$ ..... 83

Figure 6.4 The  $fV_{AC}$  vs.  $f$  graph for  $c$ -axis at (a)  $T = 295 K$  and (b)  $T = 95 K$ .....85

Figure 6.5 Temperature dependence of  $C_p/R$  for the image furnace and floating zone samples near  $T_C \sim 102 K$ .....86

Figure 6.6 Temperature dependence of $C_p/R$ near $T_C \sim 102$ K for the flux grown sample along the $c$ axis. The blue line is the measurement using the old header in our lab and the red line is the measurement in the in-field setup using the new header.....	87
Figure 6.7 Temperature dependence of $C_p/R$ near $T_C = 102$ K for $B // c$ axis. Data for $B = 0.05$ T, $B = 0.1$ T, $B = 0.25$ T, $B = 0.5$ T and $B = 1$ T are vertically offset by 0.5, 1, 1.5, 2 and 2.5 respectively.....	88
Figure 6.8 The $fV_{AC}$ vs. $f$ graph for $ab$ plane at (a) $T = 88$ K and (b) $T = 295$ K for 0.44mg sample.....	90
Figure 6.9 The $fV_{AC}$ vs. $f$ graph at $T = 88$ K and $T = 295$ K for mass = 0.22mg sample...91	
Figure 6.10 Temperature dependence of $C_p/R$ near $T_C \sim 102$ K for the flux grown sample ( $m=0.288$ mg) along the $c$ axis.....	93
Figure 6.11 The structure of LaFeAsO consisting of alternating Fe-As and La-O layers. Fe and O atoms sits at the center of slightly distorted As and La tetrahedral.....	95
Figure 6.12 Specific heat measurement using PPMS on the LaFeAsO sample in which the two anomalies could not be resolved.....	96
Figure 6.13 Frequency dependence of the ac voltage for 3.18 mg sample at a) $T = 295$ K and b) $T = 103$ K.....	97
Figure 6.14 Specific heat of LaFeAsO ( $m = 3.18$ mg) over the temperature range 120 K – 180 K in units of R.....	98
Figure 6.15 Frequency dependence of the ac voltage for 13.45 mg sample at a) $T = 180$ K and b) $T = 130$ K.....	99

Figure 6.16 The specific heat of LaFeAsO (m = 13.45 mg) using our newly built header in zero magnetic field and in the presence of 11 T magnetic field.....	100
Figure 6.17 The specific heat of LaFeAsO (m = 3.18 mg) with the background (solid black line). The background was estimated by a polynomial fit to the data above and below the transition region.....	102
Figure 6.18 (a) The subtracted data of LaFeAsO (m=3.18 mg) show two peaks, one associated with the structural transition centered at 155 K and the other due to the magnetic transition centered at 143 K. (b) The entropy change of LaFeAsO determined by integration of the subtracted heat capacity data.....	103
Figure 6.19 The temperature dependence of the electrical resistivity with no applied magnetic field and with an applied field of 8 T. The inset shows the magnetoresistance calculated from the resistivity data.....	105
Figure 6.20 Results of Hall-effect measurements on LaFeAsO showing the remarkable decrease in inferred carrier concentration and high mobility at low temperatures is shown in the top panel. The measured Hall coefficient and inferred carrier concentration is shown in the top panel inset. The bottom panel shows the Hall mobility calculated from the carrier concentration.....	106
Figure 6.21 Thermal and thermoelectric transport properties of LaFeAsO. The thermal conductivity measured in zero applied magnetic field and in a field of 8 T, shows an abrupt change in slope (inset a) as the structure transforms from tetragonal to orthorhombic upon cooling. Inset (b) shows the dramatic changes in the Seebeck coefficient that occur below the transition temperatures.....	107
Figure 6.22 A comparison of the $\Delta C_p$ results for the LaFeAsO sample using ac calorimetry setup in our lab and PPMS results by McGuire et al.....	108

Figure 7.1 Lattice and magnetic structure of PrFeAsO a) The three dimensional antiferromagnetic structures of Fe as determined by neutron diffraction data b) The magnetic structure of Fe in the FeAs plane.....111

Figure 7.2 (a) The temperature dependence of specific heat normalized to the gas constant  $R = 8.314 \text{ J mol}^{-1}\text{K}^{-1}$  of PrFeAsO sample. The black line shows the background used to estimate the change in entropy. (b) The subtracted data of PrFeAsO show two peaks, one associated with the structural transition centered at 143 K and the other due to the magnetic transition centered at 137 K.....113

Figure 7.3 The specific heat of LaFeAsO (black curve) and PrFeAsO (red curve) samples over the temperature range 110 K – 190 K in the units of R. PrFeAsO is normalized to LaFeAsO at  $T = 130 \text{ K}$ .....114

Figure 7.4 The temperature derivative of the resistivity ( $d\rho/dt$ ) and the background subtracted heat capacity ( $\Delta c_p$ ), of the RFeAsO series measured with a PPMS calorimeter.....115

Figure 7.5 A comparison of the  $\Delta C_p$  results for the PrFeAsO sample using ac calorimetry setup in our lab (bottom) and PPMS results by McGuire et al (top).....116

Figure 7.6 A plot of  $C_p/T$  vs  $T^2$  using the old and new header for the 0.62 mg sample. (Inset) The specific heat measured using our old header and new header over the temperature range 4 K to 18 K, in the units of R, ( $R = 8.31 \text{ J/ mol K}$ ).....118

Figure 7.7 The low temperature specific heat, plotted as  $C_p/RT$  vs.  $T^2$  for the  $\text{SrFe}_{1.8}\text{Co}_{0.2}\text{As}_2$  sample. The intercept of the solid black line gives the  $\gamma$ .....119

Figure 7.8 A plot of  $C_p/T$  vs  $T^2$  using new header. The blue and black data are measurements using our new header for two different runs.....120



# Chapter 1

## Introduction

There exists a family of solids, in which the electron-electron interaction plays a substantial role so that the independent-electron approximation fails. This family is known as the Strongly Correlated Electron System (SCES)<sup>1</sup>. The last two decades have witnessed a revival in the study of SCES. The subtle coupling and competition between electron, lattice, orbital and spin degrees of freedom are the essence of those systems. The interaction between the spin, orbit, lattice and electrons lead to the emergence of exciting novel ground states and phase transitions where a new picture of quasiparticles needs to be defined. The electronic correlations can cause striking many-body effects like electronic localization, magnetism and charge ordering that cannot be described in the generally very successful independent particle picture. Strong correlation effects are seen in transition metal compounds, mainly oxides, rare earth and actinide-based materials and also in organic metals and carbon-based compounds such as carbon nanotubes. The interplay of the *d* orbital electron internal degrees of freedom-spin, charge and orbital moment, makes transition metal oxides extremely sensitive to small external perturbations such as temperature, pressure or substitution. The drastic effects can range from huge changes in resistivity inducing a metal-insulator transition to influencing exceptionally high transition temperatures. A few such compounds are discussed in this Thesis. The focus will be on the specific heat of strongly correlated electron materials.

In order to study the thermodynamic properties of the materials at their phase transitions, a high sensitive technique, ac-calorimetry<sup>2,3,4</sup> is used. In this technique, the sample is illuminated with light chopped at frequency  $\omega$ . The temperature oscillation is then measured. In the experimental condition  $\tau_2 \ll 1/\omega \ll \tau_1$ , where  $\tau_1$  and  $\tau_2$  are the external and internal thermal time constants of the sample, the total heat capacity of the sample and its addenda is inversely proportional to the amplitude of the temperature oscillation, which is measured with a thermocouple or cernox resistor attached to the sample with a small amount of glue (varnish/silver paint). Using this technique, the heat capacity of sub-milligram crystals is measured in the presence and absence of magnetic fields. A detailed description about this technique is discussed in chapter three. For zero

field measurements, an established ac-calorimetry setup in our lab was used. The ac-calorimetry equipment used for Zero field measurements in our lab operates between room temperature and  $\sim 3\text{K}$ . For field measurements, we designed and built a new header that could be used in a Vapo-shield Liquid Helium Dewar that has a 14 T magnet (in Dr. Gang Cao's lab). Commercial instruments to measure heat capacity of materials, such as the Quantum Design Physical Property Measurement System (PPMS)<sup>5</sup> can operate at 9 T and temperature range 1.9 K – 400 K but require fairly large crystals (e.g.  $> 1\text{ mg}$ ) for reliable measurements. The new header that we designed and built to measure the heat capacity of sub-milligram crystals can be used at high magnetic fields ( $\sim 14\text{ T}$ ) and the temperature range 1.5 K – 350 K. Chapter four briefly discusses the setup in our lab and elaborates in detail the setup for field measurements.

Several materials investigated in this Thesis belong to the broad category of strongly correlated electrons and show interesting physical phenomena, such as Mott-like transitions, spin density waves (SDW), charge ordering, and superconductivity. First, I investigated the specific heat property of  $\text{Ca}_3\text{Ru}_2\text{O}_7$  and strontium substituted  $\text{Ca}_3\text{Ru}_2\text{O}_7$  from the Ruddlesden-Popper ruthenate family in the absence of a field. In  $\text{Ca}_3\text{Ru}_2\text{O}_7$ , special emphasis was placed on the characterization of the Neel ( $T_N = 56\text{ K}$ ) and structural ( $T_C = 48\text{ K}$ ) phase transitions. Previous measurements with relaxation-time calorimeters could resolve the  $T_N$  transition in  $\text{Ca}_3\text{Ru}_2\text{O}_7$  but the anomaly was too small for quantitative measurements<sup>6,7</sup>. On the other hand, relaxation-time calorimetry is not necessarily a reliable method for measuring latent heats at first order transitions, although all or part of the latent heat ( $L$ ) may appear in a peak in the measured specific heat. In our work, we used both relaxation-time calorimetry<sup>8</sup> and ac-calorimetry to examine the specific heat anomalies at the phase transitions. While ac-calorimetry may also not be a reliable method for obtaining latent heats, we have compared the specific heat peaks obtained under different experimental conditions and for different samples, concluding that most of the latent heat is in fact appearing in this peak. In addition, we have quantitatively measured the mean-field like step at  $T_N$  for the first time; its size is intermediate between what would be expected for an antiferromagnetic transition of itinerant (e.g. a SDW) and localized spins. We also studied the evolution of these anomalies in strontium-substituted  $\text{Ca}_3\text{Ru}_2\text{O}_7$ .

Having studied a material from the Ruddlesden-Popper ruthenate family, the material I studied next was a member from the oxyborate family. Charge Ordering (CO)<sup>9</sup> is an important phenomenon in conducting metal oxides. Fe<sub>2</sub>OBO<sub>3</sub>, has been proposed to exhibit a unique charge-ordering mechanism<sup>10</sup>. A striking feature of the low temperature monoclinic Fe<sub>2</sub>OBO<sub>3</sub> structure is an equal distribution of Fe<sup>2+</sup> and Fe<sup>3+</sup> over the two structurally distinct octahedral Fe sites. Two phase transitions have been found in Fe<sub>2</sub>OBO<sub>3</sub>. It orders ferrimagnetically below T<sub>C</sub> =155 K and a second transition assigned to charge-ordering is found at T<sub>CO</sub> =317K<sup>10</sup>. Differential Scanning Calorimetry (DSC) results from Oak ridge National Laboratory indicated some feature at higher temperature (340 K) than the reported charge ordering. DSC and relaxation time calorimetry are not reliable methods to explore specific heats of sub milligram crystals, so we used ac-calorimetry to examine the specific heat closely near the transition temperatures in the absence of a field.

Sr<sub>4</sub>Ru<sub>3</sub>O<sub>10</sub>, another member of the Ruddlesden-Popper series is a ferromagnet with a Curie temperature T<sub>C</sub> =105 K<sup>5,11</sup>. This material is poised between an itinerant metamagnetic state and an itinerant ferromagnetic state<sup>12,13</sup>. A previous thermodynamics study of this material showed unusual properties at low temperatures in the presence and absence of the field<sup>12</sup>. We found this material to be an interesting candidate to measure the specific heat with our newly built header at low temperature (~1.5K) and high magnetic field (~14T). However, although we succeeded in measuring the heat capacity of this material near the transition region with the application of magnetic field for B // *c* axis with our new header, we were not able to measure the heat capacity for B // *ab* plane, including low temperature measurements.

The next material studied using our new header was LaFeAsO, a member of the family of lanthanide iron pnictide-oxides. The discovery of superconductivity at 28 K in fluorine doped LaFeAsO<sup>14</sup> and the subsequent reports of transition temperatures up to ~50 K in some of the related rare-earth materials has generated great interest in this family of compounds. The undoped material LaFeAsO is not a superconductor but is reported to undergo a SDW transition at 150 K<sup>14,15</sup>. We studied the specific heat of this material in the presence and absence of magnetic field to examine the SDW transition.

Later, we extended our specific heat studies in the absence of a field on  $\text{PrFeAsO}^{16}$  and  $\text{SrFe}_{1.8}\text{Co}_{0.2}\text{As}_2^{17}$  that belong to the same pnictide family.

This thesis is divided into eight chapters. An introduction to SCES and the materials investigated were given in this chapter (Chapter one). In chapter two, I have included a theoretical discussion that delineates the basics of specific heat. A brief description about the exchange interaction and magnetic ordering in solids is also reviewed. Chapter three gives a description of the ac-calorimetry technique. Chapter four briefly describes the set-up for zero field measurements and elaborates the in-field setup in detail. The observed results of our experiments in the absence and presence of a field are discussed in Chapter five through Chapter seven. In these chapters, the physical properties of the materials studied, motivation for investigating the sample and the discussion of the heat capacity results will be described in detail. Chapter eight summarizes some important conclusions drawn from the results.

## Chapter 2

### Theory

#### 2.1 Introduction

In this section I will first discuss about heat capacity and other variables derived using the laws of thermodynamics. In the study of heat capacity of solids, phonons and electrons play an important role. So, I will discuss their heat capacities and give a brief review about first and second order transitions.

##### 2.1.1 Heat Capacity

The heat capacity of a system is defined as the amount of heat that enters a system divided by the temperature change of the system given by<sup>18</sup>

$$C \equiv \frac{\Delta Q}{\Delta T} \quad (2.1)$$

where  $\Delta Q$  is the amount of heat which is added to the system to raise its temperature by an amount  $\Delta T$ . The heat capacity could be measured either at constant pressure ( $p$ ) or at constant volume ( $v$ );

$$C_i = \left(\frac{\partial Q}{\partial T}\right)_i, \quad \text{where } i = p, v \quad (2.2)$$

Heat capacity is related to the internal energy of a system and can be derived from the first law of thermodynamics. According to the first law of thermodynamics<sup>18</sup>,

$$dQ = dU + dW \quad (2.3)$$

where  $dQ$  is the amount of heat added to a substance,  $dU$  is the internal energy of the system and  $dW$  is the external work done. If the external work consists only of work done by the system in increasing its volume  $V$  against an external pressure  $P$ , then

$$dW = PdV, \quad (2.4)$$

Taking 2.3 and 2.4,

$$dQ = dU + PdV \quad (2.5)$$

Taking 2.5 and 2.2a

$$C_v = \left(\frac{\partial U}{\partial T}\right)_v \quad (2.6)$$

Other properties of specific heat follow from second law of thermodynamics<sup>18</sup>. The second law of thermodynamics states that for a process with reversible heat exchange in a system that stays in equilibrium with its surroundings throughout the transition,

$$dQ = TdS \quad (2.7)$$

Heat capacities  $C_p$  and  $C_v$ , in terms of the entropies, are written as

$$C_i = T \left( \frac{\partial S}{\partial T} \right)_i \quad \text{where } i = p, v \quad (2.8)$$

Using equations 2.3, 2.4 and 2.6,

$$dU = TdS - PdV \quad (2.9)$$

Other useful thermodynamic quantities, depending on which variables are being held constant and which variables are changing during an experiment are

$$dF = -SdT - PdV \quad \text{Helmholtz Free Energy} \quad (2.10)$$

$$dH = TdS + VdP \quad \text{Enthalpy} \quad (2.11)$$

$$dG = -SdT + VdP \quad \text{Gibbs Free Energy} \quad (2.12)$$

From equations 2.10, 2.8 and 2.12,

$$C_v = -T \left( \frac{\partial^2 F}{\partial T^2} \right)_v \quad (2.13)$$

$$C_p = -T \left( \frac{\partial^2 G}{\partial T^2} \right)_p \quad (2.14)$$

Equation 2.13 is a very useful equation, since the Helmholtz free energy is more easily calculated than the Gibbs free energy. Most experiments done in the lab are at constant pressure as it is very difficult to measure  $C_v$  directly. The relation between  $C_p$  and  $C_v$  is given by the following equation<sup>18</sup>

$$C_p - C_v = \left( \frac{9\alpha_L^2 V}{K_T} \right) T, \quad (2.15)$$

where

$\alpha_L = \left( \frac{dL}{dT} \right)_p$  is the linear expansion coefficient

$V$  is the molar volume

$K_T = - \left( \frac{dV}{VdP} \right)_T$  the isothermal compressibility

It is worth noting that for solids at the pressures and temperatures under which we perform our experiments, there is very little difference between  $C_p$  and  $C_v$ .

From here on, I will use  $C_p$  and  $C_v$  to signify the heat capacities per mole (i.e.  $C/n$ )

### 2.1.2 Lattice specific heat

The Dulong and Petit law predicts that the molar heat capacity of solids is approximately a constant,  $\sim 3R$  near room temperature, where  $R = 8.314 \text{ J/mol K}$  is the ideal gas constant. This classical law fails to explain the decrease of the lattice specific heat with decreasing temperature. In order to explain this discrepancy, Einstein applied Bose statistics to phonons (lattice vibrations) to explain why the heat capacity of all materials goes to zero as the absolute temperature goes to zero. He proposed that the thermal energy of a system of  $N$  atoms vibrating with a common frequency  $\nu_E$  in 3 dimensions is given by<sup>19</sup>;

$$U = 3N(\langle n \rangle + \frac{1}{2}) h\nu_E, \quad (2.16)$$

where

$$\langle n \rangle = (\exp(\frac{h\nu_E}{kT}) - 1)^{-1} \quad (2.17)$$

where  $k$  is the Boltzmann constant and  $h$  is Planck's constant.

Now,

$$C_v = (\frac{dU}{dT}), \quad (2.18)$$

Hence by taking appropriate derivatives of energy

$$C_v = 3R(\frac{\Theta_E}{T})^2 \frac{\exp(\frac{\Theta_E}{T})}{[\exp(\frac{\Theta_E}{T}) - 1]^2}, \quad (2.19)$$

where

$$\Theta_E = \frac{h\nu_E}{k} \quad (2.20)$$

is the Einstein temperature. For  $T \gg \Theta_E$ , the molar specific heat reduces to the  $3R$  limit. This model works well for the optical (high energy) phonons in a system because

these are within narrow frequency bands but fails to quantitatively explain the low temperature behavior.

Debye improved on Einstein's theory by treating the solid as an isotropic elastic continuum. Only acoustic modes are considered. Debye's model is not exact since it assumes a simple linear dispersion of sound waves, but the theory does accurately capture the behavior of the heat capacity of solids at low temperature. In the Debye approximation, the angular frequency  $\omega$  of a harmonic wave is related to the wave vector  $q$  and the wave velocity  $v$  through

$$\omega = vq \quad (2.21)$$

where  $v$  is a constant so, the density of phonon states in 3-dimension is given by

$$D(\omega) = \frac{3V\omega^2}{2\pi^2v^3} \quad (2.22)$$

Given  $D(\omega)$ , the calculation of the energy and hence  $C_v$  is straightforward. The average total vibrational thermal energy is

$$U = \int_0^{\omega_D} D(\omega) \frac{\hbar\omega}{e^{\hbar\omega/kT} - 1} d\omega \quad (2.23)$$

The integral is evaluated up to the Debye cutoff frequency  $\omega_D$ ,

$$\omega_D^3 = 6\pi^2v^3 \frac{N}{V} \quad (2.24)$$

where  $N$  is the number of atoms in the sample and  $V$  is the volume. The appropriate derivative of  $U$  gives<sup>19</sup>

$$C_v = 9R \left( \frac{T}{\Theta_D} \right)^3 \int_0^{\frac{\Theta_D}{T}} dx \frac{x^4 e^x}{(e^x - 1)^2} \quad (2.25)$$

where  $x = \hbar\omega/kT$ ,

$\Theta_D$  is the Debye characteristic temperature: ( $\Theta_D = \hbar\omega_D/k$ ). At a very low temperature the upper limit of the integral can be taken to be infinity. Then

$$C_v = \frac{12\pi^4 R}{5} \left( \frac{T}{\Theta_D} \right)^3 \equiv \beta T^3 \quad (2.26)$$



### 2.1.3 Electronic specific heat

In an ideal metal, electrons can be viewed as a non-interacting Fermi gas. Therefore Fermi-Dirac statistics play an important role in determining the temperature dependence of the electronic contribution to the specific heat. As the characteristic temperature for an electron Fermi gas is in the thousands of Kelvin for most metals, the free electron states are nearly completely filled with two electrons per state (one spin up and one spin down) until the electron Fermi energy (the highest energy) is reached. There is some smearing of the population around the Fermi energy due to thermal energy. To a first approximation ( $T \ll T_F$ ), the electronic heat capacity expressed as<sup>19</sup>,

$$C_{el} = \frac{\pi^2}{3} N(\varepsilon_F) k^2 T \equiv \gamma T \quad (2.27)$$

where  $N(\varepsilon_F)$  is the density of states at the Fermi surface for both spins and  $\gamma$  is the Sommerfield constant. This linear dependence of temperature of the electron heat capacity holds for normal metals at sufficiently low temperatures.

At temperatures much below the Debye temperature and the Fermi temperature, the heat capacity of metals may be written as the sum of electron and phonon contributions,

$$C = \gamma T + \beta T^3 \quad (2.28)$$

Since, many of the heat capacity experiments we do are at low temperatures, equation (2.28) is very useful for us. Experimental results are usually analyzed by fitting the values of  $C_p/T$  vs  $T^2$  to a straight line. The intercept gives the  $\gamma$  term from which we acquire information about the density of electron states. The slope gives the  $\beta$  term from which we can get the Debye temperature  $\Theta_D$ .

### 2.1.4 Specific heat at a first order phase transition

A first order phase transition is characterized by a latent heat, a finite change in volume and hysteresis. At a first order transition, the entropy change  $\Delta S$  is related to the volume change  $\Delta V$  according to the Clausius-Clapeyron equation<sup>18</sup>

$$\Delta S = \Delta V \frac{dP}{dT} \quad (2.29)$$

Discontinuity in the entropy implies a latent heat (i.e.  $T_c \Delta S$ ). There is a discontinuity in the entropy because the different phases have a different energy modes and disorder. Theoretically an entropy discontinuity will produce infinity in the specific heat because

there is no temperature change as heat enters the system. In practice, we do not observe infinity because the heat capacity measured is over a finite temperature interval, the latent heat may be small, there is a spread in  $T_c$ 's due to inhomogeneities in the sample, and the experimental parameters do not allow for an infinite measurement. It is therefore often difficult to distinguish between a first order transition and a lambda shaped continuous phase transition. In such cases, hysteresis is a useful tool to help distinguish a first and continuous phase transition.

### 2.1.5 Specific heat at a second order phase transition

Any higher order transition that has a singularity or discontinuity in the specific heat is termed a continuous transition. A second order phase transition is a continuous transition characterized by discontinuity in the specific heat. It involves neither latent heat nor hysteresis, unlike a first order phase transition. Superconductivity is the best example of a second order phase transition. A formal approach to understand the discontinuous step in  $c_p$  is well described by Ginzburg-Landau (GL) theory<sup>20</sup> [4].

The theory postulates the existence of a macroscopic quantum wavefunction  $\psi$ , which was equivalent to an order parameter. The Gibbs free energy  $G$  is expanded in terms of the order parameter ( $\psi$ ) which vanishes above the critical temperature  $T_c$  and is non-zero below  $T_c$ <sup>20</sup>.

$$G = G_o(T) + a(T - T_c) |\psi|^2 + b |\psi|^4 + \frac{\hbar^2}{2m^*} |\nabla \psi|^2 \quad (2.30)$$

$a$  and  $b$  are coefficients independent of temperature and  $m^*$  is the effective mass. In the above expansion  $\psi$  is assumed to be small (near the transition).  $\psi$  vanishes above the transition and must vary slowly over space because of the gradient term.

The spatially uniform solution for the order parameter is found by omitting the gradient term and minimizing the free energy  $G$  with respect to the order parameter  $\psi$ ;

$$\psi = 0, \quad T > T_c \quad (2.31)$$

$$\psi = \left(\frac{a}{2b}\right)^{1/2} (T_c - T)^{1/2}, \quad T < T_c \quad (2.32)$$

Neglecting the higher order terms, the entropy is given by

$$S = S_o(T) \quad T > T_c \quad (2.33)$$

$$S = S_0 - \left(\frac{a^2}{2b}\right)(T - T_c) \quad T < T_c \quad (2.34)$$

Below the transition temperature, the entropy decreases linearly with temperature and the entropy is continuous at the transition point.

The heat capacity is obtained by taking the derivative,

$$C_p = C_{po}(T) \quad T > T_c \quad (2.35)$$

$$C_p = C_{po} + \left(\frac{a^2}{2b}\right)T \quad T < T_c \quad (2.36)$$

Thus the heat capacity is discontinuous at the transition point.

Although GL theory gives a fairly good qualitative description for superconductors, the parameters  $a$ ,  $b$ ,  $m^*$  are not given within any microscopic framework. The BCS theory is such a framework and gives values for these coefficients which set the scale for all quantities calculable from the GL free energy. The BCS theory<sup>21</sup> is based on pairing of the superconducting electrons mediated by phonons. BCS is a mean field theory where all interactions on one particle are treated as an average field. This theory works well if the coherence length is long and the coherence volume contains many particles. A modified form of BCS theory works well for many second order transitions in particular; the thermodynamics of the CDW state closely resembles that of a superconducting ground state<sup>22</sup>.

One of the results of BCS theory is a prediction of the transition temperature  $T_{MF}$ ;

$$kT_{MF} = 1.13 \hbar\omega_D \exp\left(-\frac{1}{N(\epsilon_F)V}\right) \quad (2.37)$$

where  $\omega_D$  is the Debye cut off frequency and  $V$  is the coupling potential. The energy gap at  $T=0$  is given by

$$E_g = 2 \Delta(0) = 3.52 kT_{MF} \quad (2.38)$$

The zero temperature gap parameter  $\Delta(0)$  is related to the heat capacity jump  $\Delta C_{MF}$  at the transition temperature. In the weak coupling limit, the mean-field heat capacity jump  $\Delta C_{MF}$  is given by<sup>21</sup>

$$\Delta C_{MF} = 4.7 N(\epsilon_F) k^2 T_{MF} \quad (2.39)$$

Above equation can also be written in terms of the electronic heat capacity,

$$\Delta C_{MF} = 1.43 \gamma T_{MF} = 1.43 C_e \quad (2.40)$$

where the Sommerfield constant  $\gamma$  is

$$\gamma = \frac{\pi^2}{3} N(\varepsilon_F) k^2 \quad (2.41)$$

A heat capacity step exists because the entropy drops continuously when a material goes through a transition into a more ordered state.

Quantum and thermal fluctuations are very important and need to be considered when evaluating the heat capacity of a material. The role of fluctuations is discussed in section 2.1.7.

### 2.1.6 Magnetic specific heat

Consider a unit volume of magnetic material and assume that it is uniformly magnetized by an applied field  $H_a$  so that it has a magnetization  $M$ . Inside the material the field seen by the moments is not the applied field but the internal field  $H=H_a+H_d$ , where  $H_d$  is the demagnetizing field. For simplicity, let us consider an elongated bar. Inside an elongated bar  $H_d = 0$ , so that  $H= H_a$ .  $M$  and  $H$  are related to the magnetic induction vector  $B$  through<sup>23</sup> [101]

$$B = \mu_0(H+M) = B_0+\mu_0M \quad (2.42)$$

where  $\mu_0 = 4\pi \times 10^{-7} \text{ N/A}^2$  is the permeability of free space. The above relation is valid at any point in space, both inside the material and outside where the magnetization is zero. If the value of the field is increased from  $H$  to  $H+dH$ , so that it produces an increase  $dM$  in the value of the magnetization, then the work required to achieve this is given by

$$dW = \mu_0HdH+\mu_0HdM \quad (2.43)$$

The first term in the above equation is the work done to increase the value of the field over the volume occupied by the sample. This work must be done whether the body is present or not and may be included in the internal energy which shall be designated as  $E'$ . The second term in the above equation is the energy required to increase the magnetization of the sample from  $M$  to  $M+dM$ . If this is indicated by  $dW_M$  then

$$dW_M = \mu_0HdM \quad (2.44)$$

The first law of thermodynamics now reads

$$dE' = TdS-PdV+\mu_0HdM \quad (2.45)$$

Now, the heat capacity at constant magnetization,  $C_M$  and the heat capacity at constant field  $C_H$  is given by<sup>23</sup>

$$C_M = \left(\frac{dQ}{dT}\right)_M = T\left(\frac{dS}{dT}\right)_M = \left(\frac{dU}{dT}\right)_M \quad (2.46)$$

$$C_H = \left(\frac{dQ}{dT}\right)_H = T\left(\frac{dS}{dT}\right)_H = \left(\frac{dU}{dT}\right)_M \quad (2.47)$$

For the difference  $C_H - C_M$  making use of the correspondence from equation 2.15  $P \leftrightarrow \mu_0 H$  and  $V \leftrightarrow -M$

$$C_H - C_M = -TV_m \mu_0 \left(\frac{\partial H}{\partial T}\right)_M \left(\frac{\partial M}{\partial T}\right)_H \quad (2.48)$$

We measure  $C_H$ .

## 2.2 Theory of Magnetic Interactions and Ordering

Since most of the samples investigated by me were part of the strongly correlated electron systems (SCES), it is important to understand magnetic interactions that happen via different mechanisms. In this section, I will confine myself to only those types of magnetic interactions, which are important in the context of my dissertation.

### 2.2.1 Exchange Interaction and ordering

Exchange interactions are quantum mechanical effects that are electrostatic interactions which increase or decrease the expectation value of the energy of two or more particles when their wave functions overlap. In order to understand the origin of exchange, let us consider a simple case of a two electron system. As explained in reference [22], the Hamiltonian of the pair is given by

$$H = -\frac{\hbar^2}{2m} \nabla_1^2 - \frac{\hbar^2}{2m} \nabla_2^2 + V(r_1) + V(r_2) + \frac{e^2}{r_{12}} \quad (2.49)$$

where  $r_1$  and  $r_2$  refer to the spatial coordinates of the two electrons and  $r_{12}$  is the separation of the two electrons.

For electrons, the overall wavefunction must be antisymmetric so the spin part of the wavefunction must either be an antisymmetric singlet state  $\chi_S$  ( $S=0$ ) in the case of a symmetric spatial state or a symmetric triplet state  $\chi_T$  ( $S=1$ ) in the case of an antisymmetric spatial state. The wavefunction for the singlet case  $\psi_S$  and triplet case  $\psi_T$  is given by

$$\Psi_S = \frac{1}{\sqrt{2}}[\Psi_a(r_1)\Psi_b(r_2) + \Psi_a(r_2)\Psi_b(r_1)]\chi_S \quad (2.50)$$

$$\Psi_T = \frac{1}{\sqrt{2}}[\Psi_a(r_1)\Psi_b(r_2) - \Psi_a(r_2)\Psi_b(r_1)]\chi_T \quad (2.51)$$

The energies of the two possible states are

$$E_S = \int \Psi_S^* \hat{H} \Psi_S dr_1 dr_2 \quad (2.52)$$

$$E_T = \int \Psi_T^* \hat{H} \Psi_T dr_1 dr_2 \quad (2.53)$$

For a singlet state  $S_1 \cdot S_2 = -\frac{3}{4}$ , while for a triplet state  $S_1 \cdot S_2 = \frac{1}{4}$

Hence the Hamiltonian can be written in the form of an effective Hamiltonian

$$\hat{H}_{eff} = \frac{1}{4}(E_S + 3E_T) - (E_S - E_T)S_1 \cdot S_2 \quad (2.54)$$

The exchange constant (or exchange integral) J is defined by

$$J = \frac{E_S - E_T}{2} = \int \Psi_a^*(r_1)\Psi_b^*(r_2)\hat{H}\Psi_a(r_2)\Psi_b(r_1)dr_1 dr_2 \quad (2.55)$$

The spin dependent term in the effective Hamiltonian can be written as

$$\hat{H}_{eff}^{spin} = -2JS_1 \cdot S_2 \quad (2.56)$$

If  $J > 0$ ,  $E_S > E_T$  and the triplet state  $S=1$  is favored

If  $J < 0$ ,  $E_S < E_T$  and the singlet state  $S=0$  is favored

In reality, there are many atoms in the solid and usually more than one magnetic electron on each atom. For all the cases we are interested in, the Heisenberg Hamiltonian is simply the form for the two-spin system, summed over all pairs of ions given by<sup>22</sup>

$$\hat{H}_{eff} = -\sum_{i \neq j} J_{ij} S_i \cdot S_j \quad (2.57)$$

A positive J favors parallel spins ( $E_T$  has lower energy than  $E_S$ ) and thus ferromagnetic ordering is preferred, while a negative J favors antiparallel spins ( $E_S$  has lower energy than  $E_T$ ) and thus antiferromagnetic ordering is preferred.

In compounds that have magnetic ions as neighbors, the magnetic moments interact via an exchange interaction known as direct exchange. As the name indicates, the exchange interaction proceeds directly without the need for an intermediary. For

compounds, where the magnetic ion sits in an environment of non-magnetic ions, the interaction, if at all is possible, happens only through mediating ions.

In metals, for instance, the exchange interaction between magnetic ions can be mediated by the conduction electrons as shown in Figure 2.1(c). The exchange interaction is thus indirect because it does not involve direct coupling between magnetic moments. It is also known as the RKKY interaction<sup>9</sup> (itinerant exchange). The interaction is long range and has an oscillatory dependence on the distance between the magnetic moments.

Another important indirect interaction in ionic solids is superexchange<sup>9</sup>. It can be defined as an indirect exchange interaction between non-neighboring magnetic ions mediated by a non-magnetic ion which is localized in between the magnetic ions as shown in Figure 2.1 (b). In transition metal oxides (TMO), where antiferromagnetism is a common occurrence, the origin of the exchange interaction between moments on the transition metal ions is described by superexchange. The spin in one transition metal ion ( $B^{n+}$ ) polarizes neighboring oxygen ( $O^{2-}$ ) which in turn interacts with the other neighboring transition-metal ion as shown in Figure 2.2. Materials like  $Sr_4Ru_3O_{10}$ ,  $Ca_3Ru_2O_7$  measured in our lab favors this mechanism. This type of interaction is normally short ranged.

The double exchange mechanism<sup>9</sup> is an exchange interaction that occurs because the magnetic ion can show mixed valency. For example, Mn ions can exist in oxidation states as  $Mn^{3+}$  or  $Mn^{4+}$ . The  $e_g$  electron on a  $Mn^{3+}$  ion can hop to a neighboring site only if there is a vacancy there of the same spin. If the neighbor is a  $Mn^{4+}$  which has no electrons in its  $e_g$  shell, there should be no problem. However, due to Hund's rule<sup>9</sup> number 1, the exchange interaction between the  $e_g$  electron and the three electrons in the  $t_{2g}$  level tends to keep them all aligned. Thus it is not energetically favorable for an  $e_g$  electron to hop to a neighboring ion in which the  $t_{2g}$  spins will be antiparallel to the  $e_g$  electron (Fig 2.3 b). Ferromagnetic alignment of neighboring ions is therefore required to maintain the high spin arrangement on both the donating and receiving ion. Because the ability to hop gives a kinetic energy saving, allowing the hopping process as shown in Figure 2.3 (a) reduces the overall energy. Thus the system ferromagnetically aligns to save energy. Moreover, the ferromagnetic alignment then allows the  $e_g$  electrons to hop through the crystal and the material becomes metallic. Double exchange is also found in

magnetite ( $\text{Fe}_3\text{O}_4$ ) which contains an equal mixture of  $\text{Fe}^{2+}$  ( $3d^6$ ) and  $\text{Fe}^{3+}$  ( $3d^5$ ) ions. A detailed study about iron oxyborate ( $\text{Fe}_3\text{BO}_4$ ) will be discussed in chapter 4.

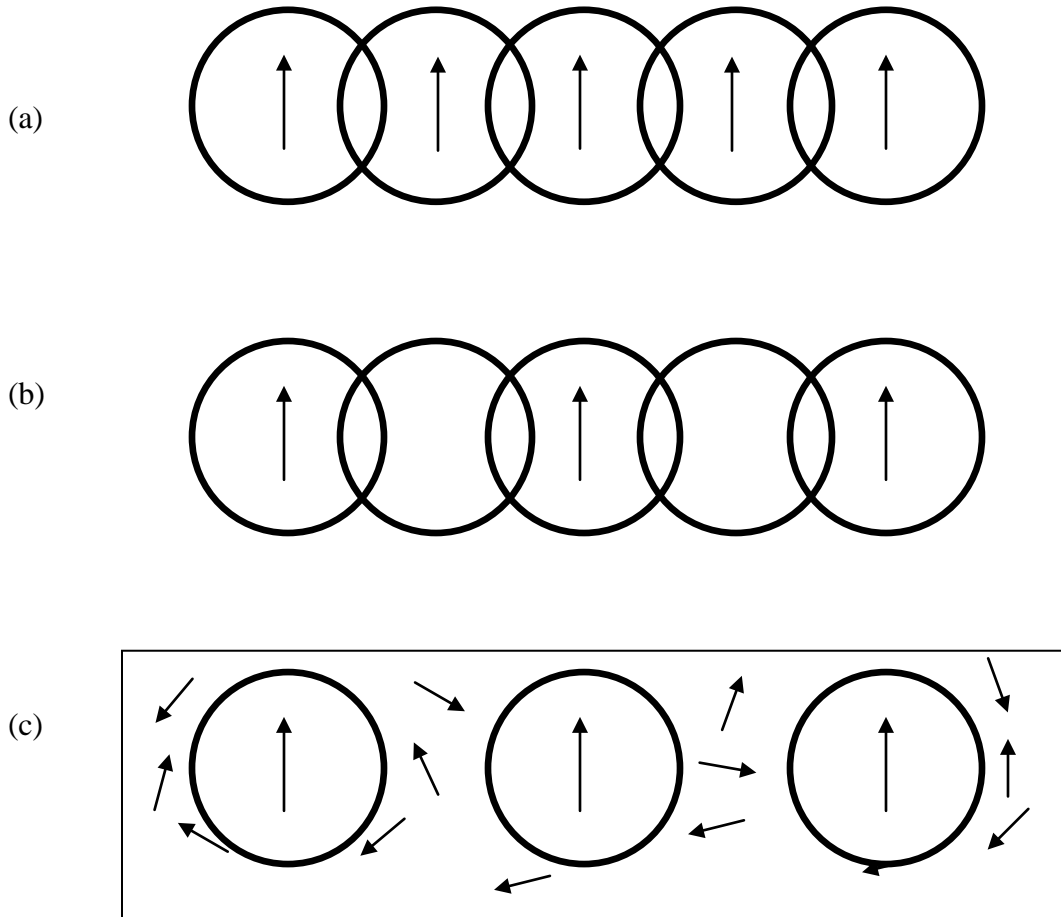


Figure 2.1 (a) direct exchange - the magnetic ions interact because their charge distributions overlap; (b) superexchange - magnetic ions with non-overlapping charge distributions interact because both have overlap with the same non-magnetic ion; and (c) indirect exchange - in the absence of overlap, a magnetic interaction is mediated by interactions with the conduction electrons<sup>29</sup>.



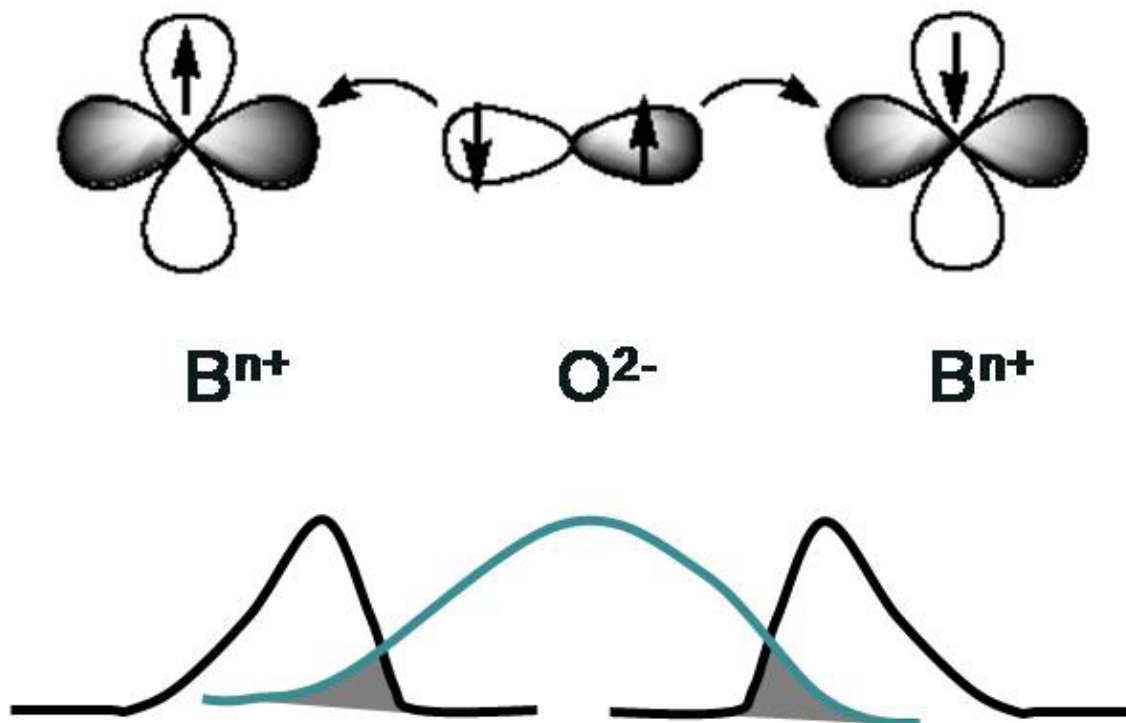


Figure 2.2 A schematic representation of Superexchange in Transition Metal Oxides (TMO's).  $B^{n+}$  is the transition metal ion and  $O^{2-}$  is the Oxygen ion<sup>9</sup>.

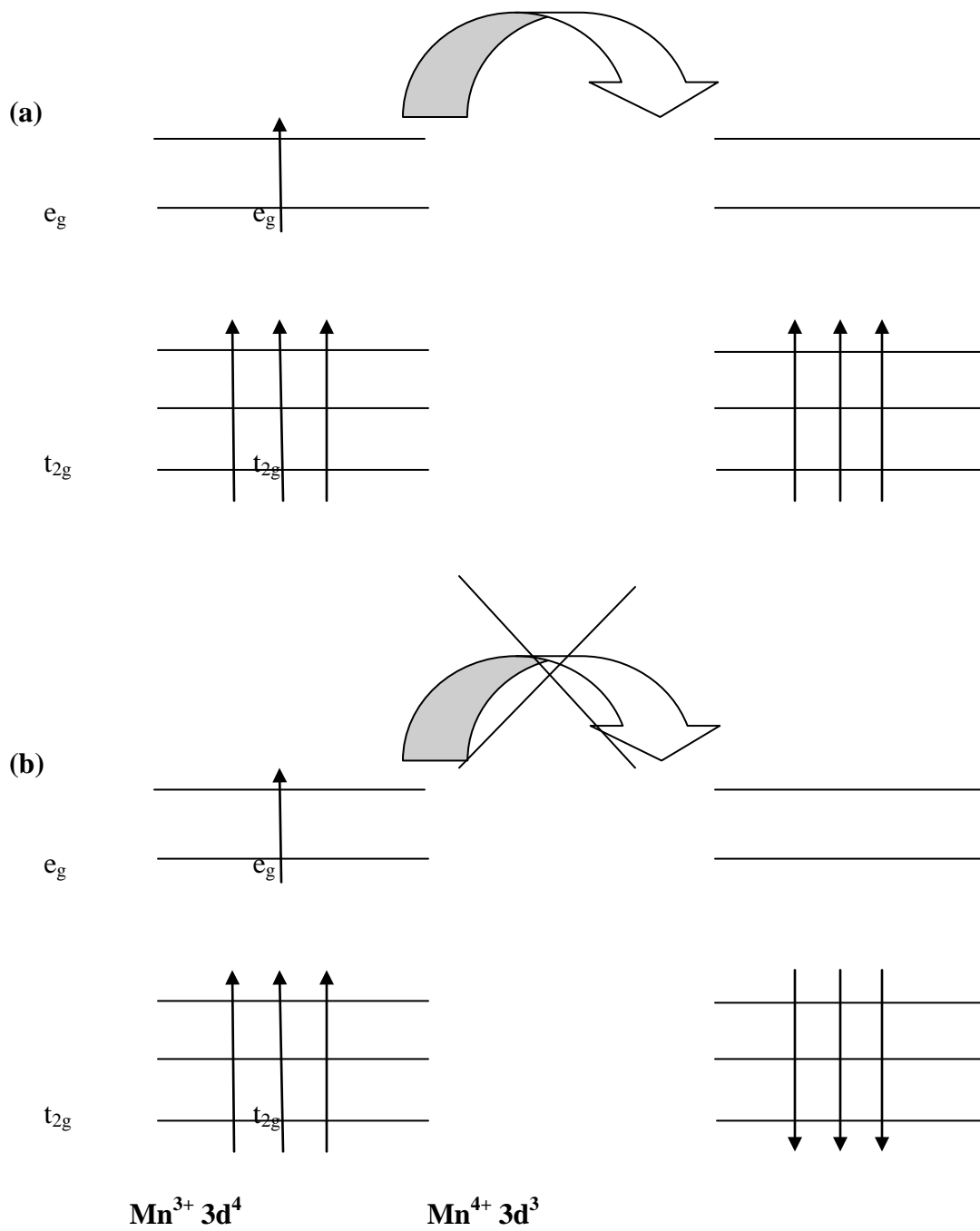


Figure 2.3: Exchange interaction favors hopping if (a) neighboring ions are ferromagnetically aligned and not if (b) neighboring ions are antiferromagnetically aligned<sup>24</sup>.

In transition metals, a complication lies in the itinerant nature of d electrons that are not strictly localized on particular ions but lie in states that overlap from atom to atom to form a narrow band. In the case of typical ferromagnetic metals such as Fe, the atomic spins are ferromagnetically coupled with the exchange integral  $J > 0$ . If all 3d electrons are localized at each atom, the magnetic moment per atom must be an integer multiple of the Bohr magneton  $\mu_B$ . However, the observed magnetic moment of Fe is a non integer and equal to  $2.2\mu_B$ . This non-integral value is not possible to understand on the basis of localized moments of atoms and is a strong evidence of band ferromagnetism. To solve this, Stoner<sup>25</sup> employed the molecular field approximation to treat the exchange interaction between the 3d electrons and assumed the molecular field or exchange integral  $J$  to be independent of the wave vector of the Bloch wave<sup>1</sup> (the wavefunction of an electron in a periodic potential). The magnetization arises by shifting the spin-up band relative to the spin-down band. Electrons must be transferred from the spin-down band to the spin-up band so as to have the Fermi level between the two sub-bands coincides. The transfer of electrons results in an increase in the kinetic energy. The total change in energy associated with the generation of magnetization is given by<sup>24</sup>

$$\Delta E = \frac{1}{2} N(E_F) (\delta E)^2 (1 - UN(E_F)) \quad (2.58)$$

where  $U$  is a measure of the Coulomb energy and  $N(E_F)$  is the density of states.

Spontaneous ferromagnetism is possible if  $\Delta E < 0$  which implies that

$$UN(E_F) \geq I, \quad (2.59)$$

which is known as the Stoner criterion. When systems meet this criterion, electron correlation, i.e. the interaction energy, dominates the kinetic energy and hence leads to magnetic ordering in metals. If the Stoner criterion is not satisfied, then spontaneous ferromagnetism will not occur, but the susceptibility may be altered. The magnetic susceptibility  $\chi$  is given by<sup>24</sup>

$$\chi = \frac{\chi_P}{1 - UN(E_F)} \quad (2.60)$$

where  $\chi_P$  is the Pauli susceptibility

### 2.2.2 Spin-Density waves (SDW)

The Stoner criterion demonstrates that the electron gas is unstable against spontaneous ferromagnetism if  $UN(E_F)$  becomes large enough and that the magnetic susceptibility can be enhanced by a factor  $(1-UN(E_F))^{-1}$ . It turns out that the q-dependent susceptibility given by<sup>9</sup>

$$\chi_q^0 = \chi_P f(q/2k_F) \quad (2.61)$$

is also enhanced by the Coulomb interactions and becomes

$$\chi_q = \frac{\chi_P f(q/2k_F)}{1-UN(E_F)f(q/2k_F)} = \frac{\chi_0^q}{1-\alpha\chi_0^q} \quad (2.62)$$

where  $\alpha = U / \mu_0 \mu_B^2$ . It may occur that  $\chi_q^0$  has a maximum at some value of  $q$  not equal to zero. In this case the interactions, parametrized by  $\alpha$ , can make the susceptibility diverge at this value of  $q$  if  $\alpha\chi_q^0$  reaches unity. Hence an oscillatory static magnetization could spontaneously develop in the sample. If  $q=0$  this would correspond to ferromagnetic order, if  $|q| = \pi/a$  then antiferromagnetic order could develop. According to Overhauser<sup>26</sup>, the ground state of a SDW is within the framework of mean field theory, if  $U \ll E_F$  (which is equivalent to the weak coupling limit for superconductors). Under the weak coupling limit, the phase transition at temperature  $T_{SDW}$  is defined by<sup>27</sup>

$$\frac{U\chi_0(2k_F, T)}{2\mu_B^2} = UN(E_F) \ln \frac{1.14E_0}{k_B T} = 1 \quad (2.63)$$

This gives

$$k_B T_{SDW} = 1.14E_0 \exp(-1/\lambda_e) \quad (2.64)$$

where  $\lambda_e = UN(E_F)$  is the dimensionless electron-electron coupling constant.

The relationship of the critical temperature to the  $T=0$  gap is the same as in the BCS theory of weak coupling superconductivity given by<sup>26</sup>

$$2\Delta(T=0) \approx 3.53k_B T_{SDW} \quad (2.65)$$

The SDW order makes a finite contribution to the specific heat, where it vanishes in a step-like fashion. The prediction of such a step anomaly is a signature of weak coupling mean-field calculations. The discontinuity at  $T_{SDW}$  is given by<sup>26</sup>

$$C_V(T = T_{SDW} - 0) - C_V(T = T_{SDW} + 0) = \frac{16\pi^2}{7\xi(3)} k_B^2 g(E_F) T_{SDW} \quad (2.66)$$

According to a more general description for the SDW in the magnetic field based on mean-field theory [104,105], the magnetic field dependence of  $T_{SDW}$  is described by<sup>28</sup>

$$\ln \left[ \frac{T_{SDW}(B)}{T_{SDW}(0)} \right] \cong \sum_{L=-\infty}^{\infty} J_L^2 \left( \frac{\varepsilon_0}{\omega_b} \right) \times \left\{ \text{Re} \psi \left( \frac{1}{2} + \frac{iL\omega_b}{2\pi T_{SDW}} \right) - \psi \left( \frac{1}{2} \right) \right\} \quad (2.67)$$

where  $J_L$  and  $\psi$  are Bessel and digamma functions, respectively.  $\omega_b = v_F e b B$  is the cyclotron frequency along the  $b'$  axis and  $e$  is the electron charge,  $v_F$  is the Fermi velocity. In an applied field  $B$ , the anomaly should broaden by  $\delta T \sim \hbar \omega_b / k_B$  (i.e.  $\hbar \omega_b / k_B$  is the effective moment). The specific heat jump at the critical temperature  $T_{SDW}(B)$  using the mean-field description is given by Montambaux<sup>29</sup>,

$$\left. \frac{\Delta C}{C} \right|_{T_{SDW}(B)} = \left. \frac{\Delta C}{C} \right|_{T_{SDW}} \left[ 1 + g(\beta) \frac{\omega_b^2}{(t_b^*)^2} \right] \quad (2.68)$$

where  $g(\beta)$  is a negative function of the parameter  $\beta = \frac{t_b'}{t_b}$ ;  $t_b' = \frac{t_b^2 \cos ak_F}{4t_a \sin^2 ak_F}$ ;

$t_b^* = \frac{t_{b0}'}{1 - 32(t_{b0}'/t_b)^2}$ ;  $t_{b0}' = \frac{T_{SDW}^0}{1.13}$ ;  $T_{SDW}^0$  is the transition temperature when  $t_b' = 0$ ,  $k_F$  is

the Fermi momentum and  $t_a$  is the transfer integral.

### 2.2.3 Mean Field calculation of specific heat of ferromagnets

A ferromagnet has a spontaneous magnetization even in the absence of an applied field. All the magnetic moments lie along in a single unique direction. This effect is generally due to exchange interactions mentioned in section 2.2.1. For a ferromagnet in an applied field  $B$ , the appropriate Hamiltonian to solve is

$$H = - \sum_{ij} J_{ij} S_i \cdot S_j + g \mu_B \sum_j S_j \cdot B \quad (2.69)$$

The first term is the Heisenberg exchange energy; the second term is the Zeeman energy. The critical temperature above which magnetic ordering vanishes is known as the Curie temperature ( $T_C$ ) in ferromagnets. The concept of a molecular field<sup>9</sup> in magnetic materials was proposed by Weiss in 1906 and predates the recognition of the exchange as the mechanism capable of aligning spins. The molecular field model is a mean-field model and predicts that the specific heat rises to a maximum value at  $T_C$  and then drops to zero discontinuously. Despite some limitations<sup>30</sup>, the mean field or Weiss model allows a first approximation of the magnetic contribution to the total specific heat. In the absence of an external field, the specific heat in the Weiss molecular field approximation is given by<sup>31</sup>

$$C_M = -V_m \frac{\lambda}{2} \frac{d}{dT} [M(T)^2], \quad (2.70)$$

where  $V_m$  is the molar Volume,  $\lambda$  is the molecular field constant and  $M(T)$  is the magnetization as a function of temperature. As  $T \rightarrow 0$ ,  $M(T) \rightarrow M(0)$ , a constant and hence  $C_M(0) \rightarrow 0$ . In contrast, when  $T$  approaches  $T_C$ ,  $|d[M(T)^2]/dT|$  increases, reaching its largest value just below  $T_C$ . Since for  $T > T_C$ ,  $M = 0$ , the molecular field model predicts that the specific heat rises to a maximum value at  $T_C$  and then drops to zero discontinuously. This is actually not what is observed since thermodynamic fluctuations near  $T_C$  broaden the mean-field step and give a sharper (e.g. lambda-shaped) peak in the specific heat. Section 2.1.7 explains the role of fluctuations in the heat capacity.

In an applied field  $H$ , the mean-field specific heat per mole may be expressed as<sup>32</sup>,

$$\frac{C_M}{R} = -\frac{3J}{2(J+1)} \frac{d[M(T)/M(0)]^2}{d(T/T_C)} \quad (2.71)$$

where  $M$  is the magnetization and  $\frac{M(T)}{M(0)} = B_J(x)$ ;  $M(0) = Ng\mu_B J$

$B_J(x)$  is the Brillouin function given by

$$B_J(x) = \frac{2J+1}{2J} \coth \frac{2J+1}{2J} x - \frac{1}{2J} \coth \frac{x}{2J} \quad (2.72)$$

where

$$x = \frac{Jg\mu_B}{kT} (H + \lambda M) \quad (2.73)$$

and,

$$T_C = \frac{Ng^2 \mu_B^2 J(J+1)}{3k} \lambda \quad (2.74)$$

In equation 2.72,  $H$  is the applied field,  $k$  is the Boltzmann constant and  $\lambda$  is the molecular field constant.

Let us consider for example  $J = 1/2$ ,  $g = 2$ , then, the specific heat is given by

$$\frac{C_M}{R} = -\frac{1}{2} \frac{d[M(T)/M(0)]^2}{d(T/T_C)} \quad (2.75)$$

where

$$M(T)/M(0) = \frac{\tanh[M(T)/M(0)]^2}{T/T_C} \quad (2.76)$$

For  $T \approx T_C$

$$\frac{C_M}{R} = \frac{3}{2} \left(3 - \frac{2T_C}{T}\right) \quad (2.77)$$

### 2.1.7 The role of fluctuations

In the Ginzburg-Landau theory discussed in section 2.1.5, the fluctuations in the order parameter were neglected. The Gaussian approximation is a first order correction to mean-field theory, valid outside a critical temperature interval near  $T_C$ . This approximation is obtained from equation 2.30 by keeping the order parameter term up to  $|\Psi^2|$  and the gradient term. In general, fluctuation contribution to the heat capacity is given by<sup>33</sup>

$$C_{fl} = C_{fl}^{\pm} |t|^{-\alpha} \quad (2.78)$$

where  $C_{fl}^{\pm}$  is the amplitude above  $T_C$ ,  $t$  is the reduced temperature ( $t \equiv T/T_C - 1$ ) and,

$$\alpha = 2 - d\nu \quad (2.79)$$

where  $d$  is the effective dimensionality of the system and  $\nu$ , the critical exponent.

For the Gaussian approximation ( $\nu = 1/2$ ), the ratio of the amplitudes above and below  $T_C$  has a universal value related to the number of components of the order parameter,  $n_0$ , through<sup>32</sup>;

$$\frac{C_{fl}^+}{C_{fl}^-} = \frac{n_O}{2^{d/2}} \quad (2.80)$$

The Gaussian approximation is only good when fluctuations are small. As the temperature approaches  $T_C$ , fluctuations may become large and the Gaussian approximation breaks down. One needs to include higher order gradient terms in the free energy<sup>34</sup>. With closer approach to  $T_C$ , even this approach breaks down.

The critical region where fluctuations are dominant may be estimated by the Ginzburg criterion<sup>20</sup>. The reduced Ginzburg temperature  $t_G$  is written explicitly as<sup>32</sup>

$$t_G \equiv \frac{T_G}{T_C} = \frac{1}{32\pi^2} \left( \frac{k}{\Delta C_{MF} \xi_0^3} \right)^2 \quad (2.81)$$

where  $T_G$  is the temperature region where fluctuations dominate and  $\xi$  is the coherence length. The fact that  $t_G \propto \xi_0^{-6}$ , implies that it is very difficult to observe the critical fluctuations except in systems with very short coherence length. This is why conventional superconductors are well described by mean field theory.

In CDW and SDW materials, one frequently observes specific heat anomalies much larger than their mean-field estimates at their phase transitions<sup>35,36</sup>. McMillan developed a finite temperature theory<sup>37</sup> based on a short coherence length. When the coherence length is short, the phonon spectrum will be significantly modified, suppressing the transition temperature  $T_C$  and increasing the heat capacity anomaly. While a precise value depends on the phonon spectrum, one roughly expects the phonon contribution to the specific heat  $\Delta C_{PH}$ <sup>38</sup>,

$$\frac{\Delta C_{PH}}{R} \sim 1.67 k N_{PH} \sim \frac{abc}{\pi^3 \xi^a \xi^b \xi^c} \quad (2.82)$$

where  $N_{PH}$  is the number of participating phonon modes, a, b and c are the lattice constants and  $\xi^a, \xi^b, \xi^c$  are the coherence lengths.

For a one-dimensional system, Lee et.al found that fluctuations suppress the transition temperature to a temperature of approximately one quarter of the mean field transition<sup>39</sup>;



$$T_C \sim \frac{T_{MF}}{4} \quad (2.83)$$

the expected heat capacity anomaly from equation (2.39) is

$$\frac{\Delta C_P}{R} \sim 38N(\varepsilon_F)kT_C \quad (2.84)$$

The above effects will increase the size of the specific heat jump, but keep its mean-field like shape. Gaussian and critical fluctuations may cause an additional divergence or cusp in the heat capacity at the transition. Therefore fluctuations often need to be considered when evaluating the heat capacity of a material.

## Chapter 3

### AC-Calorimetry Technique

#### 3.1 Introduction

The ac-calorimetry technique is based on modulating the power that heats the sample and measuring the temperature oscillations of the sample around its mean value. This can be done by using a lock-in amplifier tuned to the modulating frequency. The advantages of using this technique over the conventional adiabatic method are 1) it is suitable for sub-milligram crystals 2) small changes of heat capacity of materials at their phase transitions can be studied with great precision 3) it provides a quasi-continuous readout of heat capacity as a function of various external parameters (temperature, magnetic field etc). However, the shortcomings of the ac method are that latent heat is difficult or impossible to measure<sup>40</sup> in the case of hysteresis and the absolute value of heat capacity is not easily determined if a modulated light heat source is used.

Using this technique, I measured the heat capacity of samples in the presence and absence of magnetic field. In section 3.2, I will briefly review the method of ac-calorimetry technique. In section 3.3, I will discuss the determination of appropriate range of chopping frequencies.

#### 3.2 Method and measuring conditions of ac technique

Consider a One dimensional heat flow problem as shown in Figure 3.1. The sample to be studied is attached with GE 7031 varnish (or silver paint) to a flattened, crossed thermocouple junction (or a Cernox thin film sensor) which provides the sample rigid support to the sample holder as shown in Figure 3.2.

When modulated light is incident on the front face of the sample, the temperature of the sample will oscillate ( $T_{ac}$ ) around a constant increment ( $T_{dc}$ ) over the temperature of the thermal bath. Within an appropriate range of chopping frequencies,  $T_{ac}$  is inversely proportional to the heat capacity of the sample. We can prove this relationship, by solving the one dimensional heat flow differential equation by applying the appropriate boundary conditions. A detailed derivation is discussed in reference<sup>41</sup>.

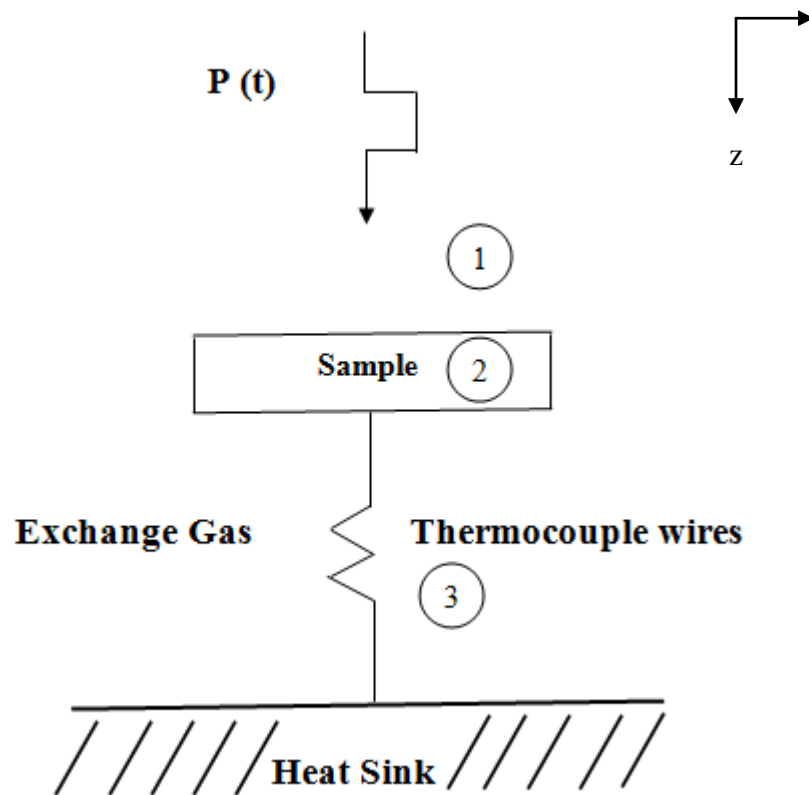


Fig 3.1. The One dimensional heat flow situation. The sample is surrounded by helium gas<sup>40</sup>.

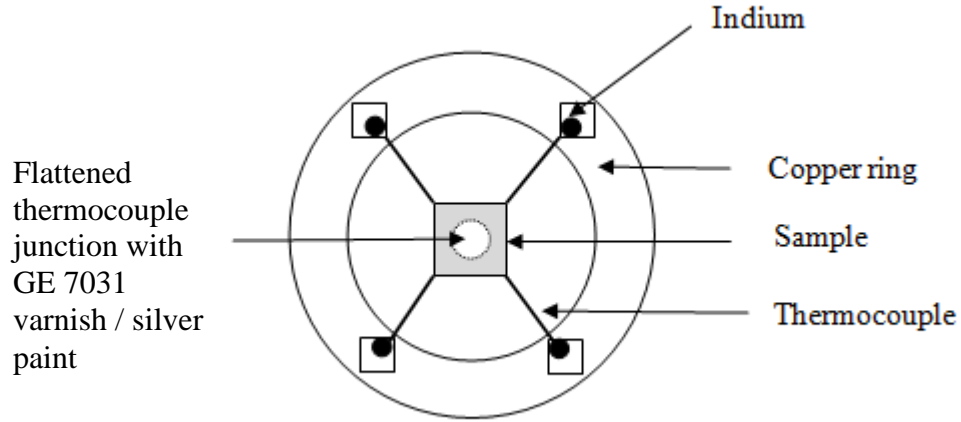


Fig 3.2 A schematic representation of the sample setting with thermocouple<sup>40</sup>.

In terms of  $\omega = 2\pi f$ , the relationship between  $T_{ac}$  and the heat capacity of the sample  $C_s$  is given by<sup>42,43,44,45</sup>

$$T_{ac} = \frac{2P_0}{\pi\omega C_s D(\omega)} e^{-i\theta} \quad (3.2)$$

where

$$D(\omega) = \sqrt{1 + \omega^2 \tau_2^2 + \frac{1}{\omega^2 \tau_1^2} + \sqrt{40} \frac{\tau_2}{\tau_1}} \quad (3.3)$$

and  $\tau_1, \tau_2$  are the external and internal relaxation times, defined below.

The phase shift of the ac signal with respect to the reference is

$$\theta = \sin^{-1} \left[ \frac{1 - \frac{4\omega^2 \tau_2^2}{3} + \sqrt{40} \frac{\tau_2}{\tau_1}}{1 + \frac{1}{\omega^2 \tau_1^2} + \omega^2 \tau_2^2 + \sqrt{40} \frac{\tau_2}{\tau_1}} \right] \quad (3.4)$$

The offset temperature shift to the bath temperature,  $\Delta T_{dc}$ , is given by

$$\Delta T_{dc} = \frac{P_0 \tau_1}{2C_s} = \frac{P_0}{2K_g}, \quad (3.5)$$

where  $K_g$  is the thermal conductance of the helium gas and/or connecting wires.

Two important characteristic time constants,  $\tau_1$  and  $\tau_2$  in equations (3.3) (3.4) (3.5) are defined as the following.

- (1) The external relaxation time constant  $\tau_1$  is the ratio of the heat capacity of the sample to the thermal conductance between the sample and thermal bath,

$$\tau_1 = \frac{C_s}{K_g} \quad (3.6)$$

This time constant characterizes the time for the sample temperature to come to equilibrium through the external thermal linkage after a thermal energy is supplied to the sample. We need the chopping frequency  $\omega$  to be much higher than  $1/\tau_1$ , so that the ac component of the sample temperature isn't dissipated.

- (2) The internal relaxation time constant  $\tau_2$  is given by

$$\tau_2 = \frac{l_s^2 C_s / V}{10K_s} \quad (3.7)$$

Where  $l_s$  is the thickness of the sample,  $V$  is the volume of the sample and  $K_s$  is the thermal conductivity of the sample (the quantity  $C_s / VK_s$  is defined as the diffusivity of the sample). This time constant characterizes the necessary time for the sample to obtain a uniform temperature after application of thermal energy. Therefore, in this case, the chopping frequency must be chosen so that  $\omega$  is much slower than  $1/\tau_2$ ; then the sample temperature is uniform in the sample when ac heat is applied.

If the chopping frequency  $\omega$  is chosen such that the internal relaxation time of the sample  $\tau_2$  is short relative to the period  $\tau_0 (=2\pi/\omega)$  and the external relaxation time  $\tau_1$  is much longer than  $\tau_0$ , i.e.

$$\tau_2 \ll \frac{1}{\omega} \ll \tau_1 \quad (3.8)$$

then equations (3.2) and (3.4) become

$$\Delta T_{ac} = \frac{2P_0}{\pi\omega C_s} \quad (3.9)$$

and

$$\theta = \frac{\pi}{2} \quad (3.10)$$

Equation (3.9) implies that the temperature oscillation  $T_{ac}$  is inversely proportional to the heat capacity of the sample because  $D(\omega) \sim 1$  under condition (3.8)

By combining equations (3.5) and (3.9) we obtain

$$\tau_1 = \frac{4 T_{dc}}{\pi \omega T_{ac}} \quad (3.11)$$

In inequality (equation 3.8), the lower frequency bound is determined by the external relaxation time constant  $\tau_1$ . Experimentally, we can control  $\tau_1$  by controlling the amount of helium gas in the sample chamber.  $\tau_1$  should not be too large, as larger  $\tau_1$  results in larger  $T_{dc}$ , i.e. a temperature gradient in the sample which can be a problem especially at low temperatures. On the other hand, the upper frequency bound is determined by the internal relaxation time constant  $\tau_2$ . The thinner the sample, the higher the bound of the measuring frequency. However, the contribution of addenda to the total heat capacity increases in a thinner sample. Therefore, all the experimental conditions have to be carefully considered and compromised in order to ensure a reliable result.

At a first order transition, for which there is a latent heat  $L$ , equation (3.2) must be modified. When there is a latent heat  $L$  at  $T = T_0$ , the sample temperature does not change until an amount of heat equal to  $L$  has been provided by the surroundings. The change in the time dependence of  $T$  for square wave heat pulses is discussed by Garnier and Salamon<sup>46</sup>, in which it is assumed that the latent heat is absorbed or emitted at a constant rate; i.e. there is no time constant associated with the latent heat. As shown in Figure 3.3, we expect a plateau on the  $T(t)$  curve with a duration  $\Delta t$  given by<sup>40</sup>

$$\Delta t = \frac{2L}{P_0}, \quad (3.12)$$

which corresponds to a decrease  $\Delta T$  in the peak to peak temperature oscillation, where  $\Delta T$  is given by

$$\Delta T = \frac{L}{C_s} \quad (3.13)$$

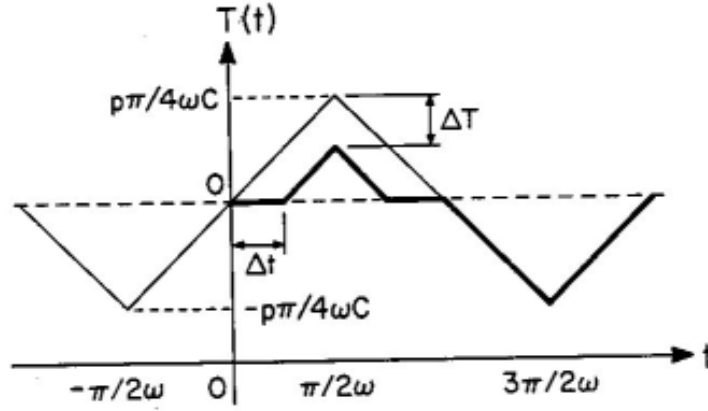


Fig 3.3 Ac temperature oscillation in the presence of a latent heat  $L$  (shown by thick solid line)<sup>40</sup>.

Fourier analyzing gives

$$\Delta T_{ac} \sim \frac{2P_0}{\pi\omega C_s} \left[ 1 - \frac{1}{2} \sin\left(\frac{2L\omega}{P_0}\right) \right] \quad (3.14)$$

In the case of the  $\text{Ca}_3\text{Ru}_2\text{O}_7$  sample discussed in chapter 5, due to sample defects,  $L$  appears to be distributed over a finite temperature interval, so that as the temperature oscillates, the latent heat sampled is given by<sup>40</sup>

$$\Delta L = \left(\frac{dL}{dT}\right) \Delta T, \quad (3.15)$$

where  $\Delta L$  depends on  $\Delta T_{ac}$  by

$$\Delta L = \frac{\pi}{2} \left(\frac{dL}{dT}\right) \Delta T_{ac} \quad (3.16)$$

where  $\pi/2$  is a prefactor from the Fourier series. If we include  $\tau_1$  and  $\tau_2$  effects, equation (3.14) changes to

$$\Delta T_{ac} \sim \frac{2P_0}{\pi\omega C_s D(\omega)} \left[ 1 - \frac{1}{2} \sin\left(\frac{\pi\omega\Delta T_{ac}}{P_0} \frac{dL}{dT}\right) \right] \quad (3.17)$$

If the sine term is small, then

$$\tilde{C} \equiv \frac{2P_0}{\pi\omega\Delta T_{ac}} \approx C_s D(\omega) + \frac{dL}{dT} \quad (3.18)$$

where  $\tilde{C}$  is the effective heat capacity. If the chopping frequency is chosen appropriately, i.e.  $D(\omega) \sim 1$  then the effective specific heat is given by<sup>40</sup>

$$\tilde{C} \sim C_s + \frac{dL}{dT} \quad (3.19)$$

If the latent heat has an intrinsic time dependence different from that of the other thermal degrees of freedom of the crystal, then there is an additional relaxation time<sup>40</sup>, e.g.

$$\tau_L = \tau_{L0} \exp\left(\frac{E_{act}}{KT}\right) \quad (3.20)$$

In such a case equation (3.19) is modified as

$$\tilde{C} = \frac{2P}{\pi\omega\Delta T(\omega)} \sim CD(\omega) + (1 + \omega^2\tau_L^2)^{-1/2} \frac{dL}{dT} \quad (3.21)$$

Latent heat can only be observed if a) on the time scale that we are changing the (average) temperature there is no hysteresis and b) the latent heat can enter/leave the sample during the chopping period. If there is a wide hysteresis in a transition, ac-calorimetry would not have seen it, as in this technique, we repeatedly heat and cool the sample by a few mK at a few Hz and measure the average oscillating temperature for a given power. The latent heat would only appear in the first oscillation and would not be measured. If one observes a hysteretic ac anomaly, it must be associated with specific heat, not latent heat. In that case, some (even most) of the entropy will be hiding in the unobserved latent heat. Hence we cannot observe hysteretic latent heat with ac measurements.

### 3.3 Determination of Proper Chopping Frequency

The ac-calorimetry experiment can be carried out when the inequality condition  $\tau_2 \ll 1/\omega \ll \tau_1$  (equation 3.8) is satisfied. Experimentally, the sample temperature will be stabilized at several temperatures (especially at low temperature where time constants change quickly with temperature). At each temperature  $T_{ac}$  (proportional to  $V_{ac}$  read from a lock-in amplifier) is measured as a function of frequency. The proper chopping frequency range at a particular temperature is then determined by



finding the frequency range for which  $T_{ac}$  is proportional to  $1/f$ . The horizontal part of a  $f$  \*  $V_{ac}$  vs.  $f$  curve shows the proper chopping frequency range at each temperature.

At room temperature, the heat capacity of the sample is relatively large. As a result, both  $\tau_1$  and  $\tau_2$  are relatively large. Typically  $\tau_1$  is several seconds at room temperature, so  $f > 0.1$  Hz, while  $\tau_2$  is typically several tens of millisecond for a 0.02 cm thick sample at room temperature, so  $f < 10$  Hz. The heat capacity of the sample normally reduces by three or four orders of magnitude from room temperature to liquid helium temperature. This results in  $\tau_1$  a reduction by two or three orders of magnitude, thereby pushing the lower frequency bound up to several tens of Hz. As the thermal conductivity of the sample normally does not change much with temperature, (except for pure metals like copper or silver, for which  $\kappa$  can go up by a factor of 10 from room temperature to liquid helium temperature) the huge decrease of sample heat capacity from room temperature to liquid helium temperature is not a problem for  $\tau_2$ .

The two time constants  $\tau_1$  and  $\tau_2$  play important roles in determining the appropriate experimental conditions. If we are not able to experimentally control these time constants to satisfy the inequality condition described in equation (3.8), then we cannot perform ac calorimetry to measure the specific heat capacity of the sample.

## Chapter 4

### Experimental Setup

#### 4.1 Introduction

I used two experimental setups to measure the heat capacity of the samples using ac-calorimetry technique. One is for zero magnetic field measurements and the other one for measurements in the presence of magnetic field. The ac-calorimetry equipment used for zero field measurements in our lab operates between room temperature and  $\sim 3$  K. The new header that we designed and built can be used at high magnetic fields ( $\sim 14$  T) and temperature range 1.5 K– 350 K.

Commercial instruments to measure heat capacity of materials such as the Quantum Design Physical Property Measurement System (PPMS)<sup>5</sup> can operate at 9 T and temperature range 1.9 K– 400 K but requires fairly big crystals (e.g.  $> 1$  mg) for reliable measurements. Since we wanted to perform measurements on sub-milligram crystals at fields  $> 9$  T, we designed and built a header that can be used in a Vapo-shield Liquid Helium Dewar that has a 14 T magnet in Dr. Cao's lab. A non-magnetic stainless steel material was used to build the header and machine shop personnel assisted us with the construction. Section 4.1.5 discusses in detail the design of the header and section 4.5 discusses the challenges involved in designing the header.

The apparatus used for measurements in the absence and presence of magnetic field are reviewed in section 4.1(a),(b). Thermometry and addendum corrections are detailed in section 4.2 and 4.3.

#### 4.2 Apparatus

##### 4.2(a) In zero magnetic field

The apparatus mainly includes an ac-calorimeter probe, a cryostat, light system and a lock-in amplifier. The heat capacity measurements were performed in a liquid nitrogen/helium glass Dewar, depicted in Figure 4.1. Figure 4.2 shows a schematic picture of the ac calorimeter. A detailed description of the cryostat, sample chamber, light system are discussed in reference<sup>39,40</sup>.

Light from a quartz halogen lamp, chopped at frequency  $f$ , irradiates the front surface of the sample. The chopped light works as an ac heat source. For

temperatures above ~12 K, the temperature oscillations were measured using a thermocouple mounted on the sample. The ac signal is measured using a SR 830 lock-in amplifier following x100 amplification using a low noise PAR 190 transformer, along with a reference signal directly from the light chopper. The dc signal is measured using a Hewlett Packard (model 34401A) digital voltmeter. Temperature measurements were measured using a Lake Shore temperature controller (model DRC-91CA). This also provides the current to the heater wrapped around the sample chamber. The heating/cooling rates are controlled by the temperature controller. All the data processing is performed by means of a computer through GPIB (IEEE-488 bus) with program written in QBASIC.

For temperatures below ~12 K, a Cernox sensor is used. Section 4.2.6 details the low temperature measurements using a Cernox sensor.

#### **4.2(b) In magnetic field**

##### **4.2.1 The Cryostat**

The heat capacity measurements in the presence of magnetic field were performed in Vapo-shield liquid Helium Dewar<sup>47</sup> (manufactured by Precision Cryogenic systems) as depicted in Figure 4.3. A NbTi superconducting solenoid magnet<sup>48</sup> (manufactured by Oxford instruments) inside the Dewar flask provides a maximum magnetic field up to 14 T. A variable temperature insert (VTI) supported from the top plate of the liquid helium Dewar provides a low temperature sample environment.

##### **4.2.2 The Variable Temperature Insert**

The variable temperature insert (VTI) operates over the temperature range 1.5 K TO 300 K, using dynamic flow of liquid helium through a heat exchanger below the sample position<sup>49</sup>. Figure 4.4 and Figure 4.5 shows the top portion and a full view of the VTI respectively. Temperatures between 1.5 K and 4.2 K may be obtained by reducing the vapor pressure of liquid helium after it has passed through the Dewar needle valve. Temperatures between 4.2 K and 300 K are achieved by setting the helium flow rate, using the VTI needle valve and gas flow pumping system. The sample space in the VTI is thermally insulated from the helium bath by an inner vacuum space (IVC).

Surrounding the sample space over most of its length is a radiation shield. The sample space extends up through the Dewar to the top plate where samples are loaded.

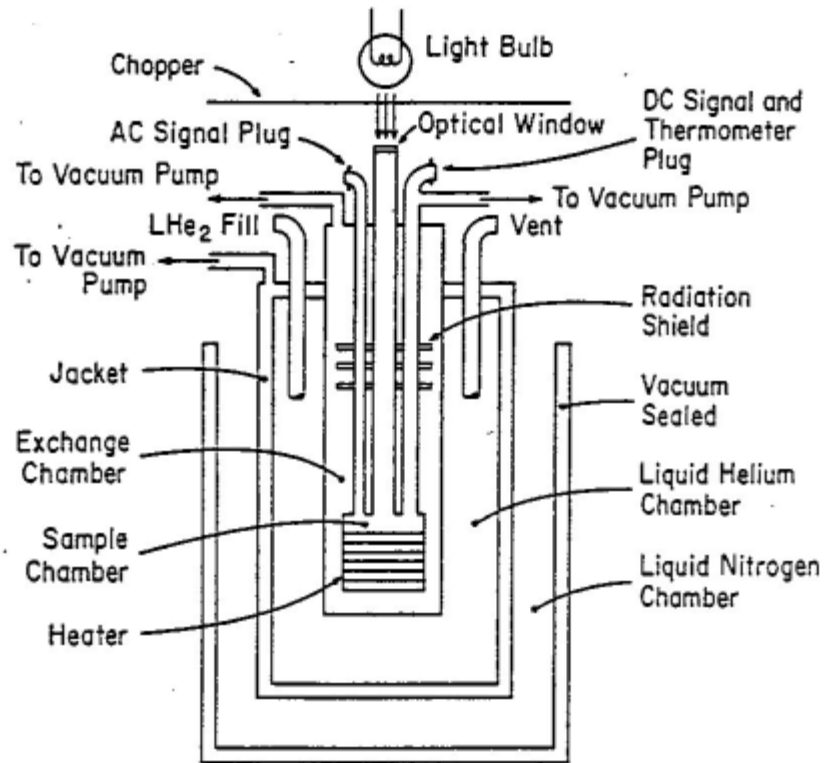


Fig 4.1 Schematic of our liquid nitrogen/helium glass Dewar<sup>40</sup>.

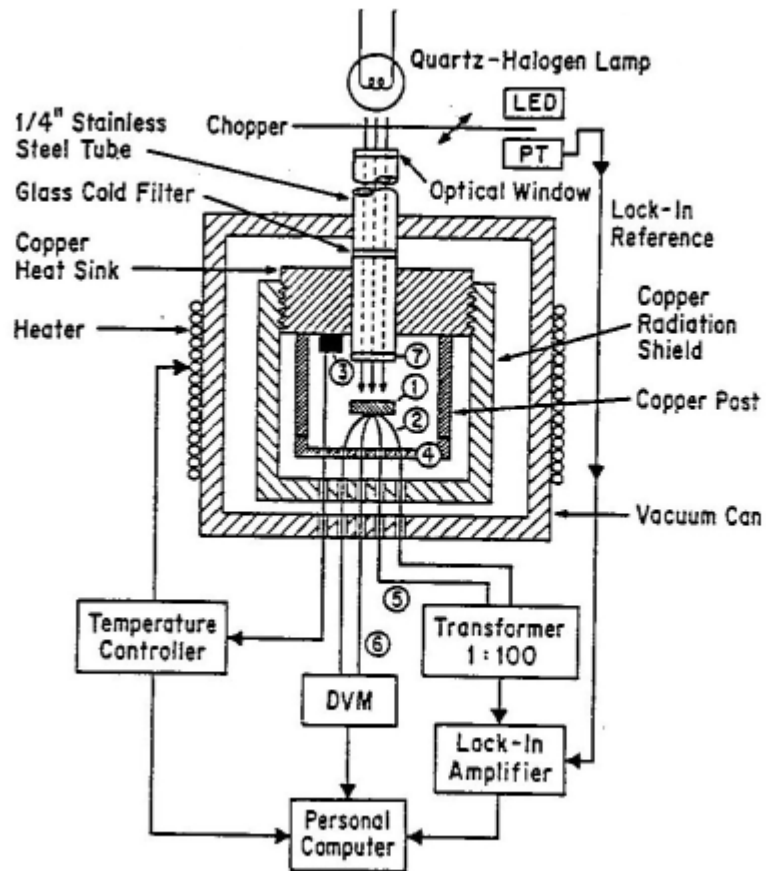


Fig 4.2 Schematic of the ac calorimeter: 1) sample 2) thermocouple wires 3) Si diode thermometer 4) Cu ring 5) ac thermocouple leads 6) dc thermocouple leads 7) lens<sup>40</sup>.

### **4.2.3 Liquid Helium Meter**

The instrument monitors the liquid helium level in a cryostat by means of a vertical superconductive wire dipping into the liquid. With a suitable current flowing, the portion of the wire above the liquid remains in the resistive (non-superconducting) state, whilst the wire immersed in the liquid is in the superconducting state. Under these conditions a measurement of the voltage developed across the wire will indicate what fraction of the wire is above the liquid surface. To reduce the power dissipated in the cryostat, the current is not passed through the wire continuously, instead the current is switched on for about a second and a reading stored within the instrument. This is then displayed on the meter until the next current pulse<sup>48</sup>.

### **4.2.4 The Superconducting magnet**

Niobium–Titanium superconducting wire is used for the magnet coils. The magnet is equipped with two superconducting switches. The superconducting switches consist of a length of superconducting wire noninductively wound with a wire electrical heater. The superconducting switch has the length of superconductor wire in parallel with the magnet sections to be energized. The superconducting wire is made resistive by raising its temperature using the heater. The switch is then in its open state and current due to a voltage across the magnet terminals will flow in the superconducting magnet windings in preference to the resistive switch element. The switch is in its closed state when the heater is turned off and the switch element becomes superconducting again<sup>47,50</sup>.

The process of establishing persistent mode operation of the magnet consists of energizing the magnet to give the required field with both switches in the open state. The switches can then be closed and the current flowing through the leads reduced to zero, leaving the magnet in its previously energized state. The current flowing in the magnet windings remain constant as the magnet lead current is reduced<sup>47,49</sup>.

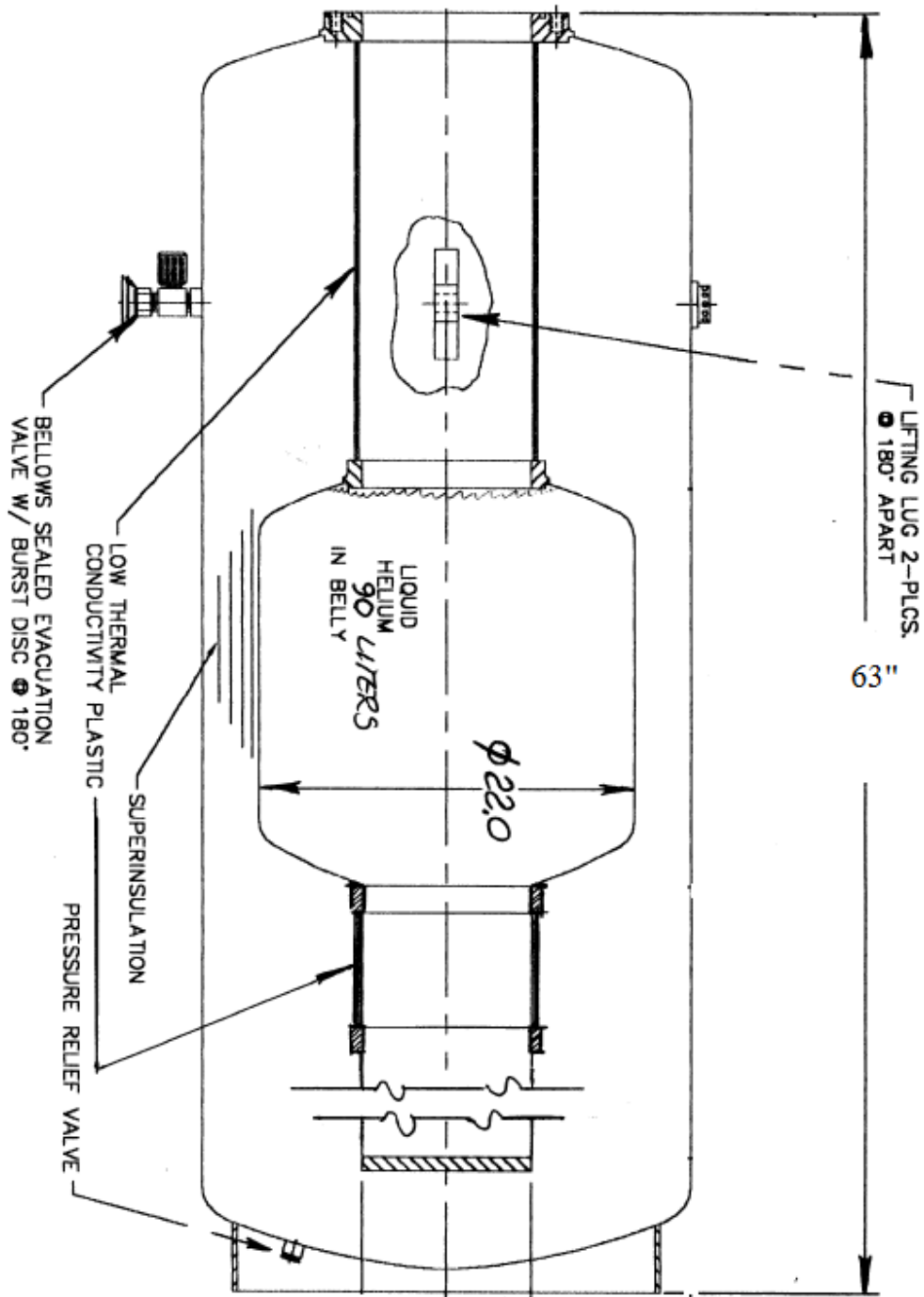


Fig 4.3 Schematic of a Vapo-shield liquid Helium Dewar<sup>48</sup>.

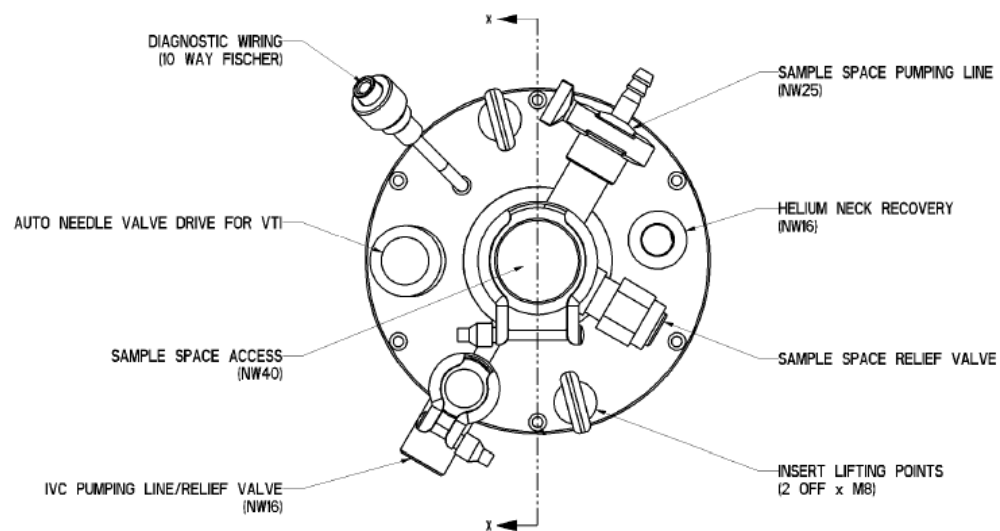


Fig 4.4 Schematic of the top portion of the Variable temperature insert (VTI)<sup>48</sup>.



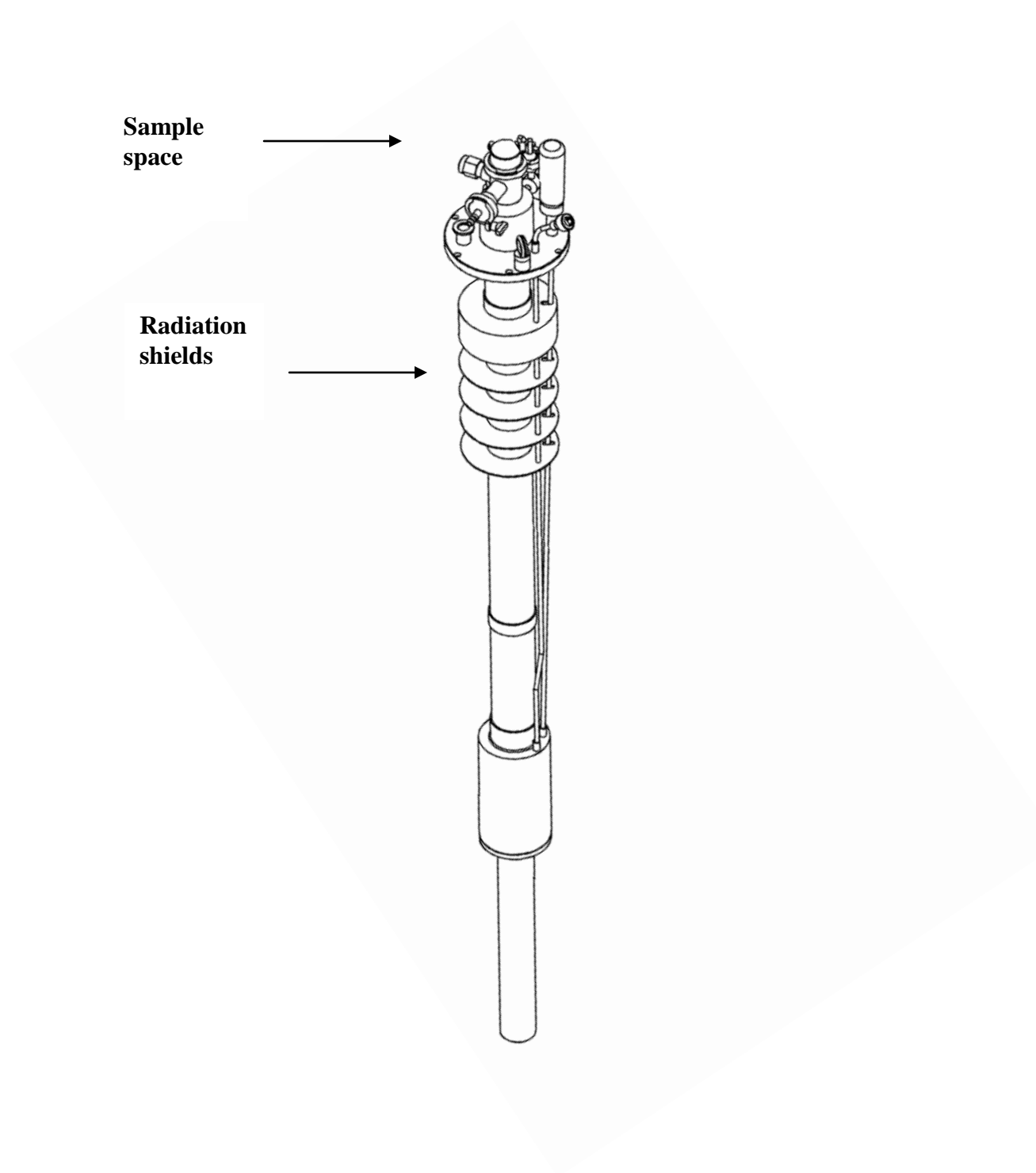


Figure 4.5 Schematic of the Variable Temperature insert (VTI) that includes the sample space, inner vacuum space (IVC, inside the sample space) and radiation shield<sup>48</sup>.

#### 4.2.5 Sample Chamber

In order to fit the sample inside the uniform part of magnetic field, a non-magnetic stainless steel tube (header) of total length 66" is used. The first piece, 62" long and 1/2" in diameter, is connected to the second piece made of copper, which is 2 3/4" long and 3/4" in diameter as shown in Figure 4.6. Manganin wire of resistance 62  $\Omega$  wound around the copper piece serves as the heater. The copper piece is connected to the third piece of length 1 3/8" and 3/8" in diameter. The Cernox thermometer used to measure the temperature of the bath and the connectors to which the wirings are soldered must be squeezed into the small area (1/8" diameter). The sample, held by 2 pairs of thermocouple wires/Cernox leads is screwed to the third piece as shown in Figure 4.6. A 3/8" diameter non magnetic stainless tube of length 64 3/4" running down the middle of the header is used for the light to pass through. The sample is shielded by a copper can 1" high to reduce temperature gradients. Four radiation shields attached to the stainless steel tube using epoxy decrease the energy radiated from the room temperature. Once the sample holder is screwed to the header, it is placed inside a 1' diameter, 68" long vacuum jacket and inserted into the sample space of the Dewar. The length of the tube resulted in a factor of 2.5 reduction of light transmission and signal using a 3ft optical fiber compared to the old header in our lab. It is important to align the sample holder at the exact center for the light to fall on the sample uniformly.

#### 4.2.6 Sample setting

The sample is held by two pairs of thermocouple wires and is used as ac and dc temperature monitor for temperatures above 20K. For low temperature, a Cernox sensor is used for its low magnetoresistive temperature errors. Figure 3.2 in chapter 3 shows the sample when held by thermocouple wires. The sample holder is an annular-shaped copper ring (5/8" od). Four sapphire plates with indium spots soldered to them for electrical connections were attached to the copper ring with varnish, providing heat sinks and serving as reference junctions for the thermocouple.

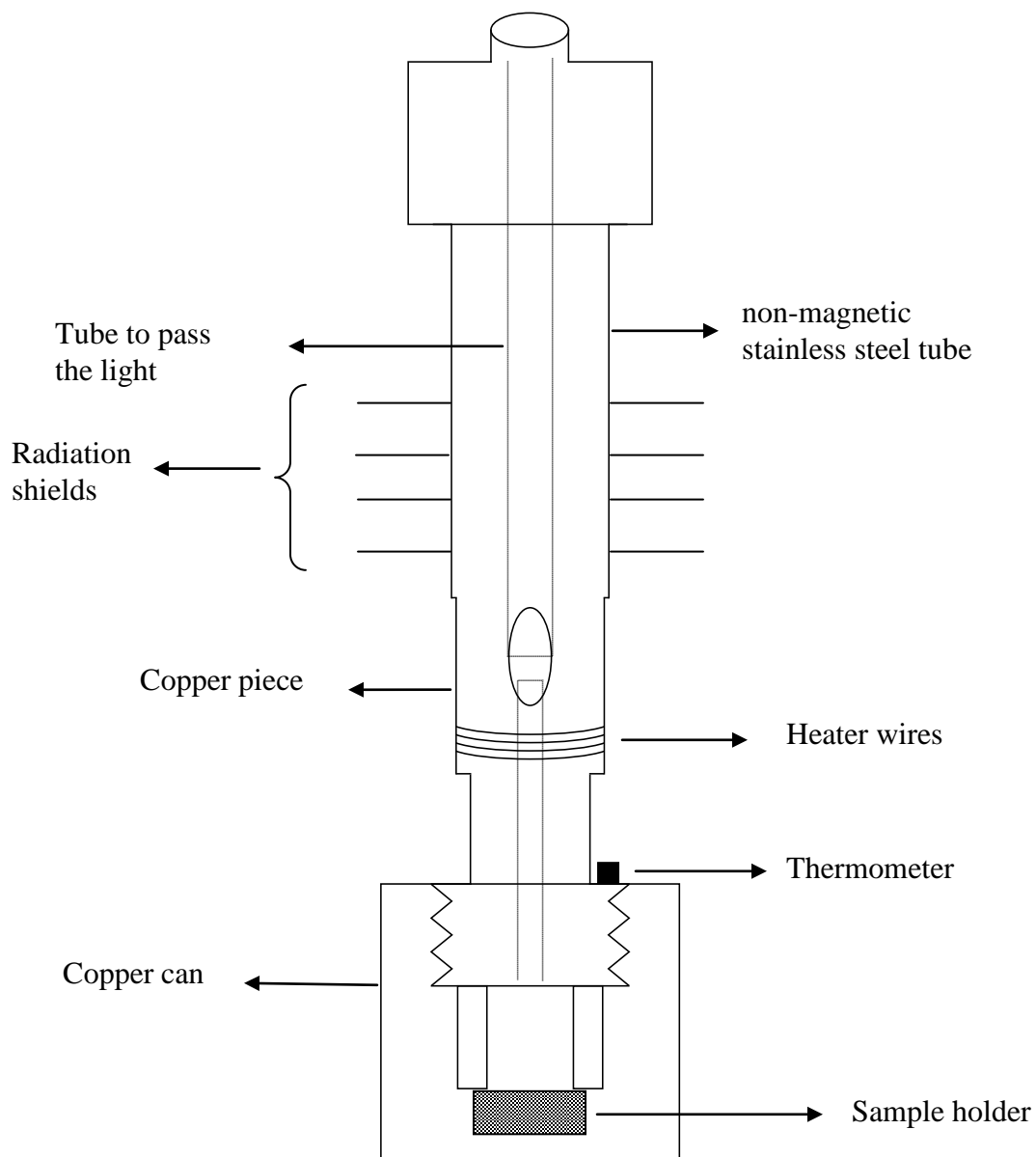


Figure 4.6 A schematic of the header designed for in-field setup.

One thermocouple is connected to a digital voltmeter (model 34401A, manufactured by Hewlett Packard) which is used to detect the electric potential differences  $V_{dc}$  between the sample and the thermal bath. The other thermocouple is connected to a low noise ( $\times 100$ ) transformer which is used to amplify and impedance match the small temperature oscillations ( $V_{ac}$ ) of the sample. A lock-in amplifier (model SR 830, manufactured by Stanford Research Systems) is used to capture the chopping frequency data and the ac signal data magnified by the transformer. All the data processing is performed by means of a computer through GPIB (IEEE-488 BUS). The light system used for measurements in the in-field setup is the same as used for zero field measurements in our lab.

In order to obtain low temperature measurements ( $< 20$  K), a Cernox 1050 BC type thin film resistance sensor is used to measure the average and oscillating sample temperatures. The sample is attached to the sensor using a small amount of GE 7031 varnish (or silver paint) as shown in Figure 4.7. The heat capacity measurement is performed by applying a constant current across the current leads and measuring the amplitude of temperature oscillations (ac voltage) from one of the voltage leads and determining the sample temperature (dc voltage) from the other voltage leads.

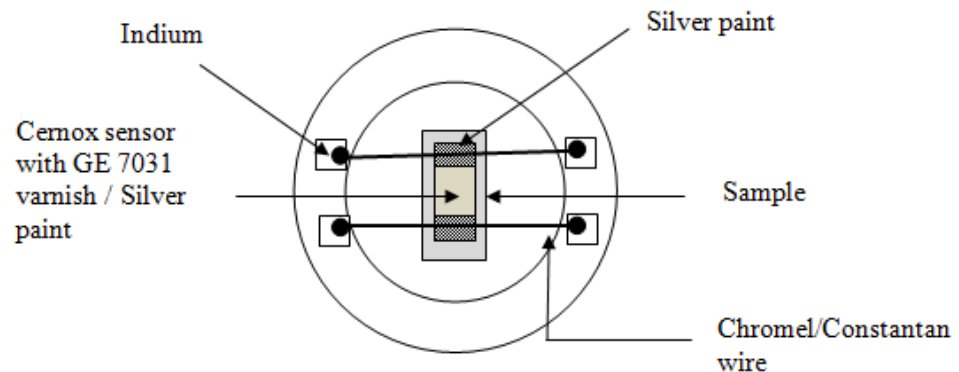


Fig 4.7 Sample setting with Cernox sensor (sample is above the Cernox sensor).

#### 4.2.7 Temperature Controller

The bath temperature was measured with a Conductus temperature controller (model LTC 21, by Neocera). This also provides the current to the heater wrapped around the sample chamber. The heating/cooling rates are controlled by an external voltage controller. The calibration file uploaded in the temperature controller corrects for the resistance errors of the temperature controller as  $R_{\text{correct}} = R' * f$  where  $f = 1.0128$  and  $R'$  is the measured Cernox resistance. The factor  $f$  was obtained by stabilizing at different temperature and recording the voltage (V) and resistance (R) displayed by the temperature controller.

#### 4.2.8 Basic Operation

Before transferring liquid helium, the Dewar and the magnet is cooled with liquid nitrogen. Once the Dewar is cold, liquid nitrogen is removed by blowing nitrogen gas for 3-4 hours and then blowing with helium gas for about 30-40 minutes. This is done to ensure that there is no liquid nitrogen inside the Dewar; otherwise formation of frozen nitrogen can waste liquid helium and possibly, damage the system. Liquid helium is then transferred into the Dewar. A temperature below 77 K is achieved by opening the needle valve and controlling the pumping system. Once the liquid helium meter shows 40 percent helium level, the magnet can be switched on. Higher fields (~11 T) can be applied at 60 percent helium level.

The pressure in the sample space is usually maintained at 500 mtorr of helium gas, which gives useful values of  $\tau_1$ .

#### 4.2.9 Test Run

A test run was performed in the header by loading  $\text{Ca}_3\text{Ru}_2\text{O}_7$  sample, for which the specific heat in the temperature range 13 K-280 K was already known using the ac-calorimetry set up in our lab. A few data runs taken by warming the sample in zero field in the in-field setup showed that the specific heat was consistent with previous measurements.

### 4.3 Thermometry

#### 4.3.1 Temperature sensors for thermal bath

The main characteristics in selecting a thermometer are accuracy, reproducibility on thermal cycling, long-term calibration, drift, magnetic-field dependence, sensor size and cost. Based on these characteristics, out of the vast array of thermometer sensors available, we chose temperature sensors appropriate for the measurements in our lab which are discussed below.

##### 4.3.1 (a) In zero magnetic field

For the temperature measurement of the thermal bath, a Si diode (DT-470, Lake Shore Inc) is used which we calibrated against a standard thermometer by Lake Shore Inc diode. The temperature measurements were made using a four-wire configuration to avoid errors associated with the lead resistance. The sensitivity of the DT-470 is 2.4 mV/K at 305K, 1.9 mV/K at 77K and 33 mV/K at 4.2K<sup>51</sup>.

##### 4.3.1 (b) In magnetic field

In the presence of magnetic field, a Cernox (CX-1050-LR-1.4D, Lake Shore Inc) resistance temperature sensor is used. The Cernox sensor has a relatively small magnetoresistance and high sensitivity at Liquid helium temperature. The magnetoresistance is negligibly small above 30 K and not significantly affected by orientation relative to the magnetic field. The typical magnetic field dependent temperature errors are shown in Table 4.1<sup>50</sup>.

**Table 4.1  $\Delta T/T(\%)$  for Cernox 1050 temperature sensor at B(Tesla)**

T(K)	2.5 T	8 T	14 T	19 T
2	1.3	3.1	3.9	5
4.2	0.1	-0.15	-0.85	-0.8
10	0.04	-0.4	-1.1	-1.5
20	0.04	0.02	-0.16	-0.2
30	0.01	0.04	0.06	0.11
77	0.002	0.022	0.062	0.11
300	0.003	0.004	0.004	0.006

The Cernox sensor was calibrated by Lake Shore Inc from 119K to liquid helium temperature in zero field. Since we wanted calibration data from room temperature to 86 K, we calibrated the Cernox sensor against the Si diode (DT-470, Lake Shore Inc) in our lab. There is a  $3/4$  °K error associated with our sensor calibration data with respect to the standard calibration from Lake Shore. The calibration curve of the Cernox LR type sensor is shown in Figure 4.8 and Figure 4.9

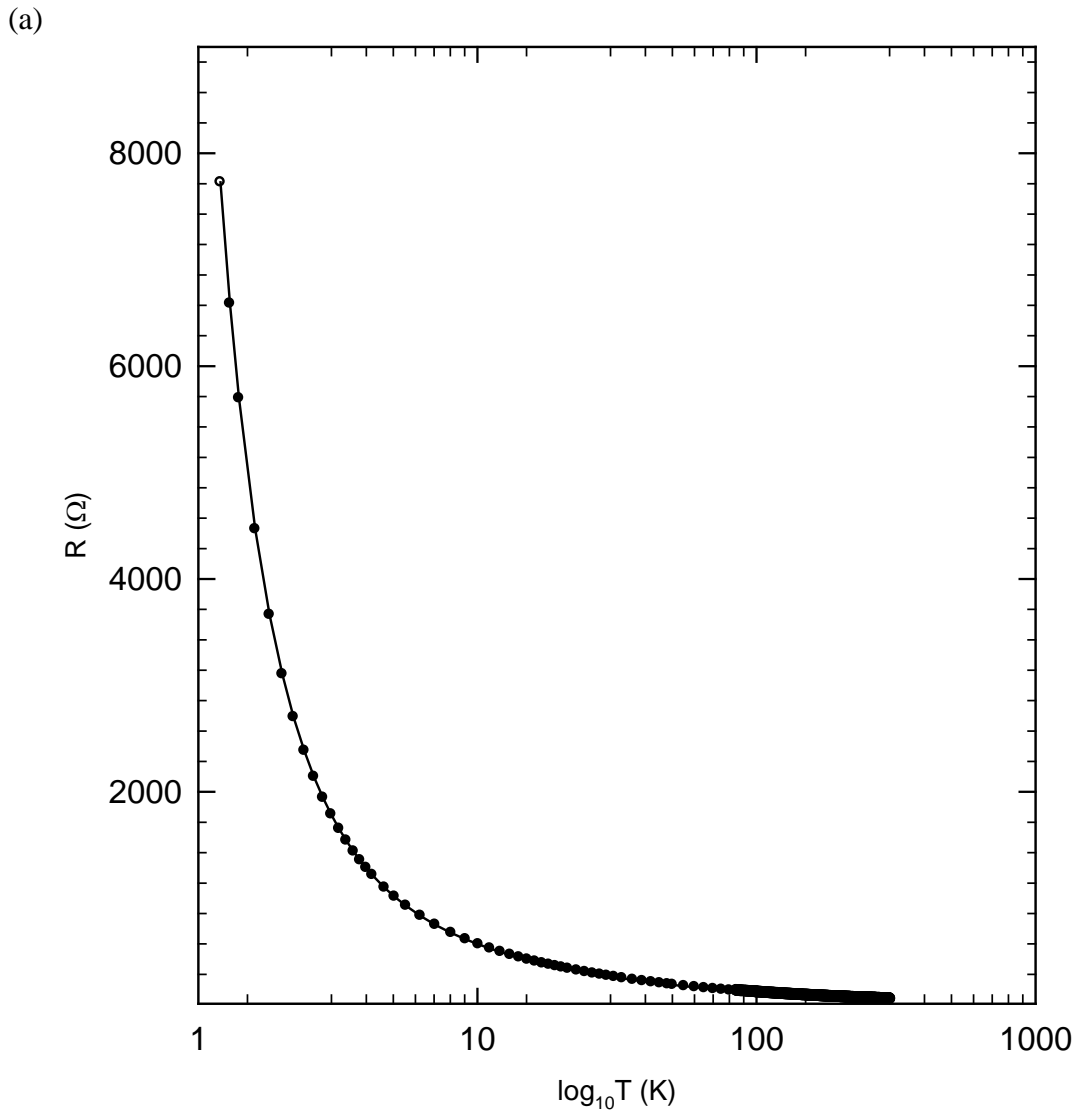


Figure 4.8 The calibration curve of the Cernox (CX-1050-LR-1.4D) thermometer used as a temperature sensor for the thermal bath in the newly built header.

(b)

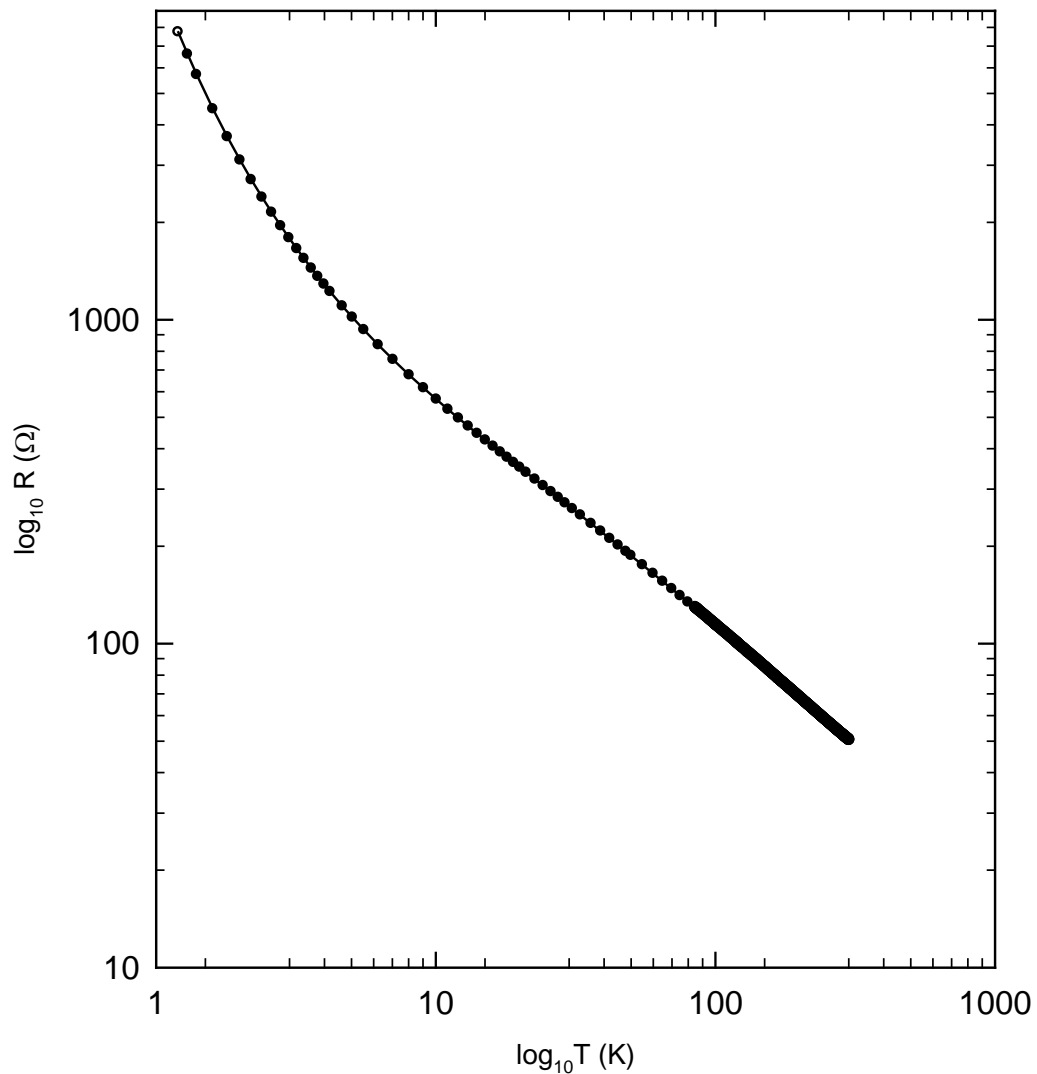


Figure 4.9 A  $\log T - \log R$  plot of the cernox (CX-1050-LR-1.4D) thermometer used as a temperature sensor for the thermal bath in the newly built header.

### 4.3.2 Temperature sensors for dc offset and ac temperature

#### 4.3.2 (a) In zero magnetic field

Thermocouples are excellent choices to measure the small temperature differences between the sample and thermal bath, because of their small size (less addendum contribution), fast response time and satisfactory accuracy. The type E thermocouple (chromel-constantan) is ideally suited for measurements above 10 K because of its high



sensitivity at high temperature. At low temperatures, thermocouples are used less commonly than the other thermometers because their temperature sensitivity is poor below 10 K. Since the temperature region of interest for most of the samples measured were above 10 K, I used type E thermocouples. The sensitivity of the type E thermocouple is  $8.5 \mu\text{V/K}$  at 20 K <sup>52</sup>.

#### 4.3.2 (b) In magnetic field

In addition to their poor sensitivities, thermocouples are generally difficult to use as low temperature thermometers in the presence of magnetic field. The failure of low sensitivity thermocouples as thermometers in magnetic field at low temperature required us to use a temperature sensor which has smaller field- induced errors. The Cernox thin film resistance temperature sensors (CX 1050 BC) manufactured by Lake Shore Inc., are excellent for use in magnetic fields and are extremely sensitive at low temperature. They have the advantages of very low magnetic field-induced errors, excellent stability and fast characteristic thermal response times ( $1.5\text{ms}$  at  $4.2 \text{ K}$ )<sup>50</sup> which is crucial for ac response monitors. Another advantage of this Cernox sensor over thermocouples is that one can actually control the sensitivity ( $dV/dT$ ) by controlling the excitation current, where the sensitivity of thermocouples is fixed at a particular temperature.

I used type E thermocouple for measuring the phase transition in LaFeAsO and  $\text{Sr}_4\text{Ru}_3\text{O}_{10}$  samples in the presence of magnetic field, since the region of interest was above 100K for these samples and the thermocouple has a very low magnetic field dependent temperature error at high temperatures. The typical magnetic field dependent temperature errors are shown in Table 4.2 <sup>50</sup>.

**Table 4.2  $\Delta T/T(\%)$  for Type E thermocouples at B(Tesla)**

T(K)	2.5 T	8 T	14 T
10	1	3	7
20	<1	2	4
455	<1	<1	2

### 4.3.3 Calibration of Cernox sensor

The CX 1050 BC type thin film resistance temperature sensor was calibrated against a Si diode in zero field in the temperature range in which it is used (below 20 K). A “semi-four probe” configuration was used to calibrate the sensor as shown in Figure 4.10.

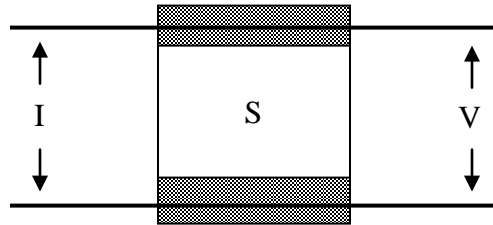


Figure 4.10 Two chromel / constantan wires (thick black lines) attached to Cernox sensor (S) by silver paint (grey areas)

Two chromel / constantan wires were attached to two ends of the thin film Cernox resistor by small amounts of silver paint. A constant dc current was applied across one side of two leads while the voltage was measured across the other side of the leads. During calibration, the measuring power was kept small enough to eliminate self-heating. Also a considerable amount (more than 1 torr) of exchange gas was put inside the cryostat to ensure good thermal contact between the Cernox sensor and Si diode.

### 4.4 Addendum correction

In an ac-calorimetry measurement, the total heat capacity includes that of the thermocouple wires or Cernox thermometer and connecting wires and GE 7031 varnish / silver paint. For a sub-milligram crystal, the addendum heat capacity may not be negligible, it is therefore necessary to correct for it. However, it is difficult to determine addenda contribution accurately, due to mass uncertainties. We therefore tried to keep the addenda heat capacity less than 10 percent of the total.

The method which we use to correct for addenda is as follows. In this section, I term  $C$  as the total heat capacity.  $C_A$  is the total capacity of the addenda involved in the

experiment which is the sum of the individual heat capacity of the thermocouple wires/cernox sensor and glue (GE 7031 varnish or silver paint).  $C_S$  is the heat capacity of the sample.  $C_T$  is the total heat capacity, which is inversely proportional to the  $T_{ac}$  that we measure.  $C_T$  is given by

$$C_T = C_S + C_A \quad (4.1)$$

We pick a temperature  $T_0$  where we want to normalize our ac data; then the proportionality constant  $b$  can be defined by

$$b = T_{ac}(T_0) \cdot C_T(T_0) = T_{ac}(T_0) \cdot [M_S \cdot c_s(T_0) + C_A(T_0)] \quad (4.2)$$

where  $M_S$  is the mass of the sample,  $c_s(T_0)$  is the specific heat (i.e. heat capacity per kilogram) of the sample given by published data or PPMS measurements at temperature  $T_0$ . The specific heat of the sample at other temperatures is then found from

$$\begin{aligned} c_s(T) &= C_S(T)/M_S = [C_T(T) - C_A(T)] / M_S \\ &= [b/T_{ac}(T) - C_A(T)] / M_S. \end{aligned} \quad (4.3)$$

The specific heats of type E thermocouple, Cernox thin film temperature sensor and GE 7031 varnish/silver paint are available from previous measurements<sup>40,53</sup> measured using ac-calorimetry to the lowest possible temperatures, and we measured and estimated the addenda masses as well as we could.

#### 4.5 Sources of heating, pick-up and noise

Radiative heating is a significant problem in most cryogenic measurements because of the large temperature gradients that exist in cryostats. It is minimized in our setup by using few radiation shields and shielding the sample with a copper holder. Self-heating from the sensor measuring current can cause significant errors in temperature readings. The effects are usually greatest at liquid-helium temperature and below, where thermal-contact boundary resistances are high. Self-heating is corrected by using a low sensor current. A few other sources of heat important in low temperature are vibrational heating and the joule heating in the wire leads and thermometer. Vibrational sources of heating can be produced due to people walking around, mechanical pumps working near the experiment, etc. We did not see any substantial heating of the sample due to these vibrations. Joule heating in connecting leads and in thermometers, give rise to a heat

input  $Q = I^2R$ . In our experiment using the newly built header, there was  $0.25^\circ$  K offset in temperature due to Joule heating. Eddy current heating is another unwanted heat source which presents a serious problem in calorimetry where nanowatts are significant. Eddy currents did not produce any significant effect in our measurements.

Pick-up and noise were especially important to us because we were looking for nanovolt signals. Pick-up and noise came in many forms. There was pick-up of the ac signal from the pumping system and the power supply of the magnet. To solve these problems, we did not run at or near 60 Hz or 120 Hz and we shielded every wire. This included the use of coaxial cabling with the outer shield attached to the ground. We grounded the header so that all metal components near the sample holder were grounded. All of the leads running down into the header were twisted together to minimize any pick-up. The pump was switched off when measurements were taken.

#### **4.6 Challenges involved in the design and operation of the probe for the in-field setup**

There were a number of factors we had to take into consideration when we built this header for the in-field setup. The sample space in the Dewar is only 1" in diameter, therefore we had to design a header with a 1/2" diameter that could effectively fit the thermometer and connectors. This posed a major challenge. With only a small space left, the thermometer and connectors had to be squeezed in a small area (3/8" diameter).

For the electrical connections, there were 10 copper wires each of length 6" that ran down the header from room temperature. They were thermally anchored to the copper piece with varnish. Extreme care had to be taken to secure them well within the header and connect them to the connectors. Since the wires are fragile, breaking a wire would require us to disassemble the entire setup and rebuild the connections from the start.

Another major concern we had was in using the light-chopper assembly. The light for the periodic heating of the sample is provided by a quartz-halogen lamp (the same setup used in our lab for zero field measurements). A home-made chopper using a turntable placed between the lamp and the optical fiber cable is used for data acquisition. We were concerned if the chopper would be affected by the magnetic field, so we decided to use a longer optical cable (9 ft) and keep the light-chopper assembly at a distance unaffected by the magnetic field. But we found that the 9ft optical fiber cable resulted in

a factor of 4.5 reduction of light transmission. The experiment could not be performed with so little light hitting the sample as the ac signal would be too noisy. Having decided to continue using the 3 ft optical fiber, we switched on the magnet by placing the light-chopper assembly at a reasonable distance. Magnetic fields as high as 13 T did not affect the chopper frequency, stability or performance. Hence we fixed the position of the light-chopper assembly and used the 3 ft optical fiber for light transmission.

From a monetary view, it requires 100 Liters liquid helium to cool the magnet and 100 Liters to perform measurement at high magnetic field (~ 14 T) and the cost of liquid helium is high. Though it is a challenge to work with a small area and the cost of liquid helium is expensive, the header is a useful tool to measure heat capacity at low temperatures and high magnetic field.

## Chapter 5

### Specific heat Measurements in Zero Magnetic Field

#### 5.1 Introduction

In this chapter, the results of the specific heat measurements on various materials at their phase transitions will be presented. The materials discussed in this chapter are  $\text{Ca}_3\text{Ru}_2\text{O}_7$ , Sr substituted  $\text{Ca}_3\text{Ru}_2\text{O}_7$  and  $\text{Fe}_2\text{OBO}_3$ .

This chapter is partitioned into two sections. In section 5.1, I will discuss the specific heat of  $(\text{Ca}_{1-x}\text{Sr}_x)_3\text{Ru}_2\text{O}_7$  single crystals by briefly reviewing the physical properties of  $\text{Ca}_3\text{Ru}_2\text{O}_7$  (section 5.1.1), motivation for doing heat capacity measurements on  $(\text{Ca}_{1-x}\text{Sr}_x)_3\text{Ru}_2\text{O}_7$  crystals (section 5.1.2) and sample preparation (5.1.3). Magnetic and transport property measurements are presented in section 5.1.4. Results will be discussed in section 5.1.6. The  $\text{Ca}_3\text{Ru}_2\text{O}_7$  and Sr substituted  $\text{Ca}_3\text{Ru}_2\text{O}_7$  samples were provided by Dr. G. Cao from University of Kentucky and magnetic and transport property measurements were performed in his lab.

In section 5.2, I will discuss the specific heat of  $\text{Fe}_2\text{OBO}_3$  crystals. The physical properties of  $\text{Fe}_2\text{OBO}_3$  (section 5.2.1), motivation for doing the measurements (5.2.2), sample preparation and data (5.2.3) will briefly be presented. Section 5.2.4 discusses the results from heat capacity measurements.  $\text{Fe}_2\text{OBO}_3$  samples were provided by Dr. Angst Manuel from Oak Ridge Laboratory. Differential Scanning Calorimetry (DSC) and resistivity measurements were performed in his lab.

#### 5.2 Specific heat of $(\text{Ca}_{1-x}\text{Sr}_x)_3\text{Ru}_2\text{O}_7$ single crystals

##### 5.2.1 The physical properties of $\text{Ca}_3\text{Ru}_2\text{O}_7$

The Ruddelston-Popper ruthenates  $(\text{Ca}_{1-x}\text{Sr}_x)_{n+1}\text{Ru}_n\text{O}_{3n+1}$  ( $n$  = number of Ru-O layers per unit cell) [21] are a class of correlated electron materials showing a rich variety of properties. The physical properties of the ruthenates are critically linked to 'n' and to the cation (Ca or Sr) which lead to different ground states and inter and intra layer magnetic couplings. The Ru ions are surrounded by O ions forming a distorted octahedra so that the two Ru ions interact only through O ions.

$\text{Ca}_3\text{Ru}_2\text{O}_7$  is a double layered compound ( $n=2$ ) of the multilayer RP series and has two layers of Ru-O octahedral per unit cell. It crystallizes in an orthorhombic structure with lattice parameters of  $a = 5.3720 \text{ \AA}$ ,  $b = 5.5305 \text{ \AA}$ ,  $c = 19.572 \text{ \AA}$  with space group  $A2_1ma$ <sup>54</sup>. A schematic of the crystal structure is shown in Figure 5.1 (a), where the  $\text{RuO}_6$  layers are indicated as red octahedra. TEM image in Figure 5.1 (b) shows the double layered nature of the compound. The dark grey spots in the image represent the Ru-O layers and the lighter ones the Ca-O. The crystal structure is severely distorted by a tilt of the  $\text{RuO}_6$  octahedra as seen in Figure 5.1 (a). The tilt projects primarily onto the  $ac$  plane ( $153.22^\circ$ ), while it only slightly affects the  $bc$  plane ( $172.0^\circ$ )<sup>55</sup>.  $\text{Ca}_3\text{Ru}_2\text{O}_7$  is an intermediate between the bad metal  $\text{CaRuO}_3$  ( $n = \infty$ ) and the Mott insulator  $\text{Ca}_2\text{RuO}_4$  ( $n = 1$ ). Because of the borderline nature of properties bi-layered calcium ruthenate will be a useful window to probe the physics of materials near metal insulator transition.

The spin structure of the double layered compound ( $n=2$ ) is especially unusual. In the pure strontium (i.e.  $x = 1$ ) salt, there is no resulting long range spin order at ambient pressure but longitudinal strain can induce a ferromagnetic state<sup>56,57</sup>. In the pure calcium salt ( $x = 0$ ), the spins order ferromagnetically within the bilayers but the inter layer ( $c$  axis) interactions are predominantly antiferromagnetic leading to a Neel transition at  $T_N = 56\text{K}$  with spin polarization along the  $b$  axis<sup>58,59,60,61</sup>. With further cooling, the spin polarization rotates within the plane towards the  $a$  axis<sup>6,58</sup>. There is a second, more unusual, phase transition at  $T_C = 48 \text{ K}$ <sup>6,58</sup>; here all components of the susceptibility drop abruptly upon cooling through  $T_C$ , which has been suggested to be due to the formation of a charge-density wave<sup>62</sup> while the lattice contracts along  $c$  axis by  $\sim 0.1\%$ <sup>60,63</sup>.

## 5.2.2 Motivation

Previous measurements with relaxation time calorimeters could resolve the  $T_N$  transition in the pure material but the anomaly was too small for quantitative measurements<sup>6,7</sup>. On the other hand, relaxation time calorimetry is not necessarily a reliable method for measuring latent heats at first order transitions, although all or part of the latent heat may appear in a peak in the measured specific heat. In this work we use both relaxation time calorimetry<sup>8</sup> and ac calorimetry<sup>3,39,64</sup> to examine the specific heat anomalies at the phase transitions. While ac-calorimetry may also not be a reliable method for obtaining latent heats<sup>2,45</sup> (discussed in chapter 3), we have compared the

specific heat peaks obtained under different experimental conditions and for different samples, concluding that most of the latent heat is in fact appearing in this peak, in agreement with the conclusion of Reference [6]. In addition we have quantitatively measured the mean field like step at  $T_N$  for the first time, its size is intermediate between what would be expected for an antiferromagnetic transition of itinerant (e.g. a spin density wave) and localized spins. Also the evolution of these anomalies with strontium substitution is discussed.

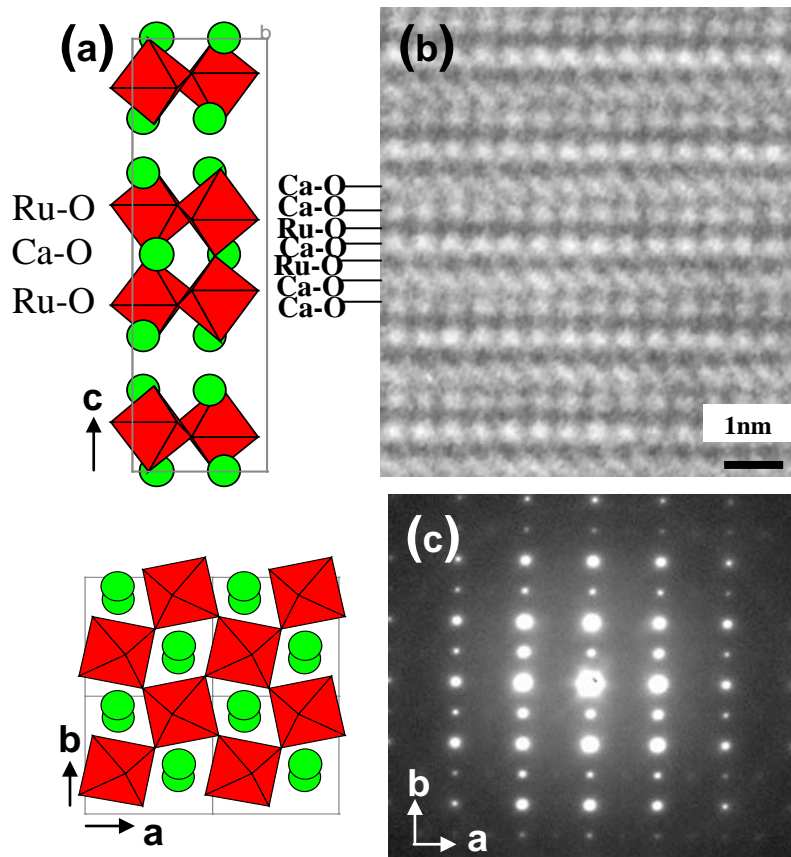


Figure 5.1 (a) Crystal structure of  $\text{Ca}_3\text{Ru}_2\text{O}_7$ , projected along the  $c$  axis (top figure) and the  $ab$  plane (bottom figure) (b) The TEM image depicts the double layered nature of the compound (c) Electron diffraction image reveals the anisotropic nature within the basal plane of  $\text{Ca}_3\text{Ru}_2\text{O}_7$  <sup>54</sup>.



### 5.2.3 Sample preparation

Single crystals of  $(\text{Ca}_{1-x}\text{Sr}_x)_3\text{Ru}_2\text{O}_7$  were grown using flux techniques by G Cao et al.<sup>65</sup>. All single crystals were grown in Pt crucibles from off-stoichiometric quantities of  $\text{RuO}_2$ ,  $\text{CaCO}_3$  ( $\text{SrCO}_3$ ) and  $\text{CaCl}_2$  ( $\text{SrCl}_2$ ) mixtures, with  $\text{CaCl}_2$  ( $\text{SrCl}_2$ ) being self flux. The mixtures were first heated to 1480 °C in a Pt crucible covered by a Pt cover, soaked for 25h, slowly cooled at 2-3 °C h<sup>-1</sup> to 1380 °C and finally cooled to room temperature at 100 °C h<sup>-1</sup>. The starting Ca:Ru ratio and the thermal treatments are critical and delicately balanced for the formation of perovskite crystals, as the nucleation of its sister compounds  $(\text{Ca}, \text{Sr})\text{RuO}_3$  and  $(\text{Ca}, \text{Sr})_2\text{RuO}_4$  is also energetically favorable. By carefully changing the ratio and thermal treatments we have successfully grown crystals of  $\text{Ca}_{n+1}\text{Ru}_n\text{O}_{3n+1}$  and  $\text{Sr}_{n+1}\text{Ru}_n\text{O}_{3n+1}$  with  $n = 1, 2, 3$  and  $\infty$ <sup>63,58,66</sup>. All crystals studied were characterized by single crystal or powder x-ray diffraction, EDS and TEM indicating good crystal quality with no impurities or intergrowths or significant clustering of the strontium ions. All crystals grown by flux method such as that mentioned here become nonmetallic below  $T_C$ <sup>58</sup>, but for those grown in a floating zone furnace only the c axis resistivity becomes activated, so the transition appears to correspond to a change from three-dimensional to two dimensional transport<sup>7,62</sup>. It is not yet clear which type of growth yields more defect-free (e.g. oxygen-stoichiometric) crystals.

### 5.2.4 Magnetization Data

Magnetic and transport properties were measured using a Quantum Design MPMS XL 7T magnetometer. The results of ab-plane magnetization measurements measured with a small field ( $B = 0.5$  T) is shown in Figure 5.2. For the pure  $x = 0$  sample, the  $T_N = 56$  K transition appears as a peak in  $M_b$  and cusp in  $M_a$ , while  $M_a$  falls at the  $T_C = 48$  K transition, as previously observed<sup>58</sup>.

“Light” ( $x = 0.15$ ) strontium substitution increases  $T_N$  and decreases  $T_C$ , decreases the size of the magnetic anomalies (with  $M_b$  developing a minimum between the two transitions) and makes the overall magnetic susceptibility more isotropic. A transition to a nonmetallic state is also observed in the resistance (not shown) between 40 K and 50 K. For the  $x = 0.58$  sample, the susceptibility is almost isotropic in the ab plane (suggesting that the  $\text{RuO}_6$  octahedra are almost “untilted”, as in the pure strontium compound) with

peaks in  $M$  at  $T_N \sim 50$  K, followed by weak minima ( $T \sim 40$  K) and relatively high susceptibilities at lower temperatures. Only small anomalies are observed in the resistance at these temperatures, and the shape of the magnetic anomalies suggests that the spin ordering is complex but incomplete. A more complete discussion of the substitution dependence of the resistance and magnetization, including their field dependences is not discussed here.

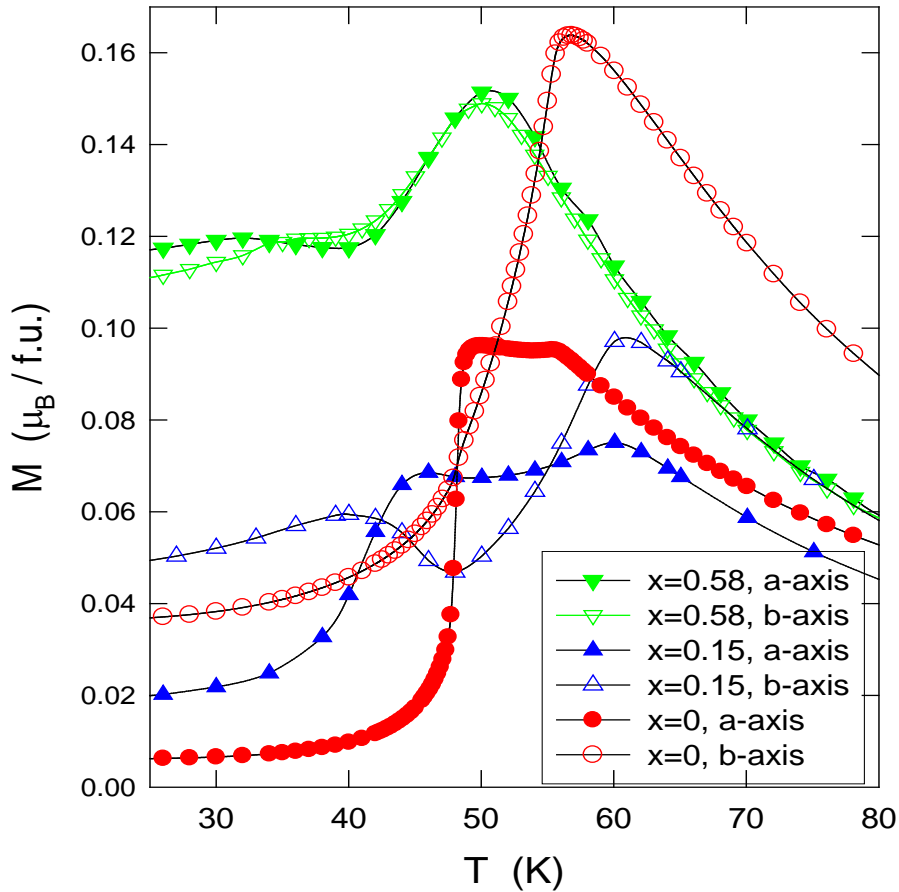


Figure 5.2 Temperature dependence of the magnetic moments (per formula unit) for the pure and strontium-substituted samples near the phase transitions with fields (0.5 T) applied along the  $a$ -axis and  $b$ -axis<sup>66</sup>.

### 5.2.5 Specific Heat measurements

Using ac-calorimetry we measured the specific heat of flux grown pure and Sr-substituted single crystals. For the  $\text{Ca}_3\text{Ru}_2\text{O}_7$  crystals, the measurements were made on crystals of masses 0.36mg and 0.40mg. For the Sr- substituted samples, the masses were 0.43mg ( $x = 0.15$ ) and 0.54 mg ( $x = 0.58$ ). The samples were attached with silver paint to a flattened, 25  $\mu\text{m}$  diameter type- E thermocouple junction. The chopping frequency used was  $\omega/2\pi \sim 6$  Hz (with resulting  $\Delta T(\omega) \sim 3$  mK). The  $fV_{\text{AC}}$  vs.  $f$  graph at 295 K and 50 K for 0.36mg sample is shown in Figure 5.3 (a) (b). Measurements were taken at several frequencies near the phase transitions where the temperature drift rate,  $|dT / dt|$  was kept under 0.1 K/min.

AC-calorimetry measurements only yield relative data as discussed in chapter 3. The results for the pure ( $x = 0$ ) samples were normalized at  $T=130\text{K}$  and corrected for addenda contributions ( $\sim 10\%$  at low temperatures) to the data taken on a pure 0.78mg sample with a Quantum Design PPMS relaxation time calorimeter<sup>8</sup> as shown in Figure 5.5. We were not able to obtain quantitative results on this sample with ac-calorimetry because it had a relatively long internal time constant, presumably because of an interlayer crack. The  $fV_{\text{AC}}$  vs.  $f$  graph at 295 K and 100 K is shown in Figure 5.4 (a) (b). On the other hand, PPMS results on the smaller ac samples were also not quantitative. The 0.76mg sample heat capacity was only  $\sim 10\%$  of the PPMS platform heat capacity for temperatures  $>20$  K so our normalizing data should be considered only approximate. However, our PPMS results are within 10% of the results of Yoshida, et al.<sup>7</sup>, except at the lowest temperatures.

A fit of our low temperature PPMS results (Fig 5.5 (b)) to  $C_p = \gamma T + \beta T^3$  for  $10 \text{ K} < T < 40 \text{ K}$  gives values of  $\gamma/R \sim 1.3 \times 10^{-3} \text{ K}^{-1}$  and  $\beta / R \sim 4.8 \times 10^{-5} \text{ K}^{-3}$  (corresponding to a Debye temperature of  $\Theta = 388 \text{ K}$ ), intermediate between the values of Yoshida, et al.<sup>7</sup> and Mc Call, et al.<sup>6</sup>

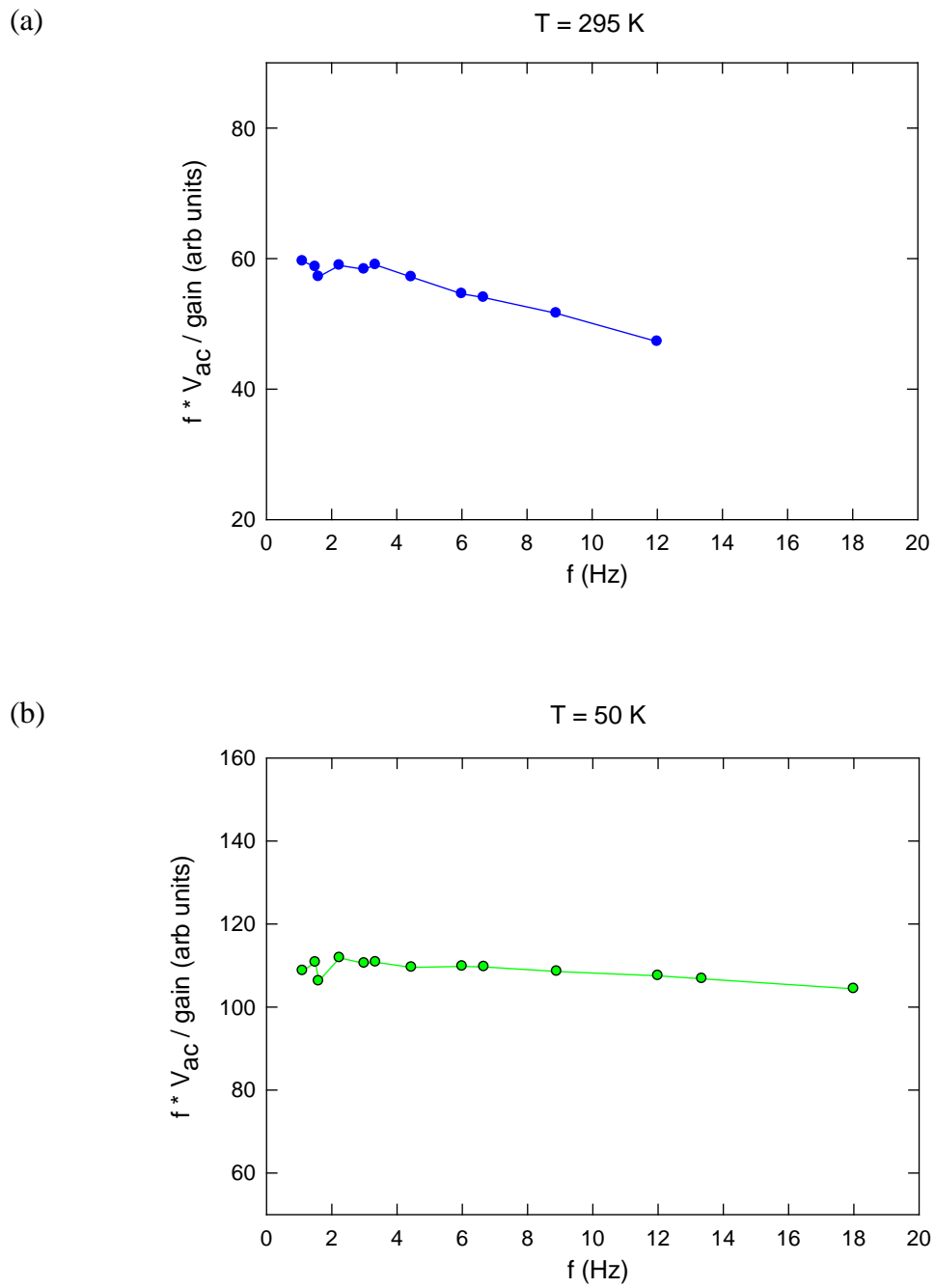
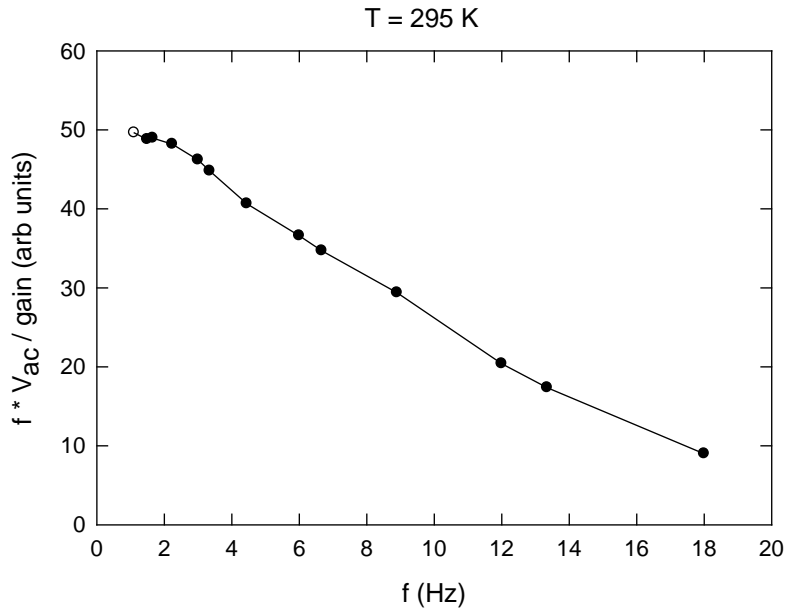


Figure 5.3  $fV_{AC}$  vs.  $f$  curve for 0.36 mg  $\text{Ca}_3\text{Ru}_2\text{O}_7$  sample at (a)  $T = 295 \text{ K}$  (b)  $T = 50 \text{ K}$

(a)



(b)

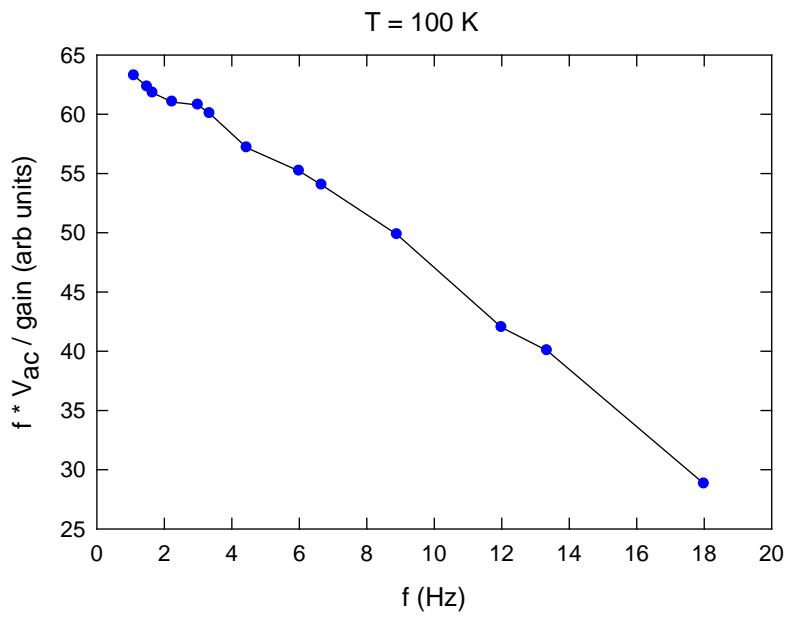


Figure 5.4  $fV_{AC}$  vs.  $f$  curve for 0.78 mg  $\text{Ca}_3\text{Ru}_2\text{O}_7$  sample at (a)  $T = 295$  K (b)  $T = 100$  K

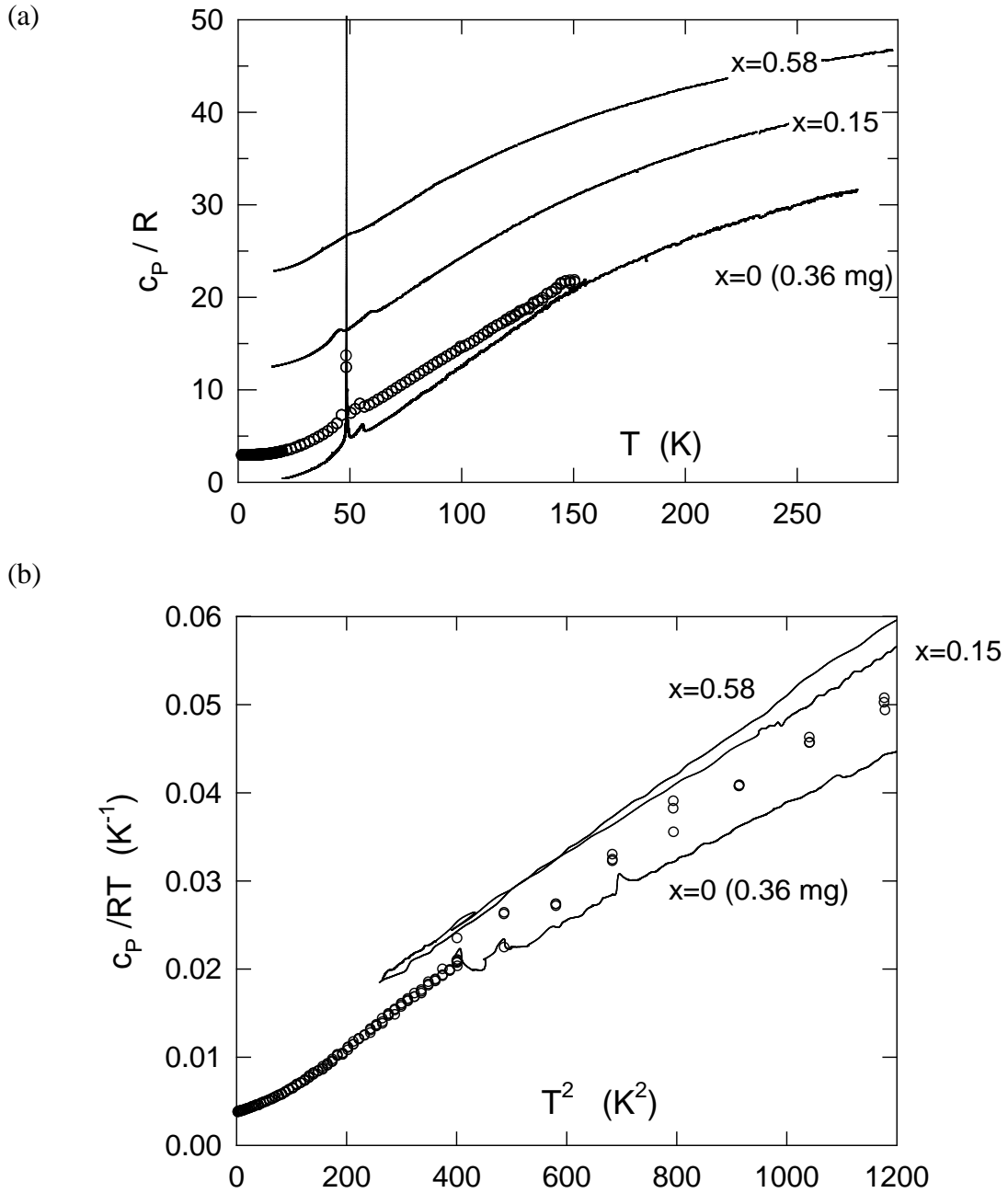


Figure 5.5 (a) The overall temperature dependence of specific heat, normalized to the gas constant  $R = 8.31 \text{ J mol}^{-1} \text{ K}^{-1}$ , of  $(\text{Ca}_{1-x}\text{Sr}_x)_3\text{Ru}_2\text{O}_7$  crystals measured with ac-calorimetry (solid curves); data for the  $x = 0.15$  and  $x = 0.58$  samples are vertically offset by 10 and 20 units, respectively. The open symbols show the PPMS results for the pure sample. (b) Enlargement of the low temperature specific heat, plotted as  $C_p/RT$  vs  $T^2$  for the same samples<sup>67</sup>.

The consequence of normalizing our ac results to the PPMS results at high temperatures is that the low temperature ac results differ from the PPMS results by  $\sim 10\%$  (as seen in Figure 5.5 (b) (and also Figure 5.7) reflecting both the uncertainty in the PPMS results and marginal sample time constants at some temperatures. For the strontium-substituted samples, which were not large enough for quantitative PPMS measurements, we normalized the data by assuming that the force constants are roughly equal in all materials so that the low temperature  $\beta \sim (\text{molecular weight})^{3/2}$  (approximately consistent with the results of Cao et al<sup>65</sup>) as also shown in Fig 5.5 (b) , with the resulting overall temperature dependences shown in Fig 5.5 (a). Hence for all samples, the normalization of the data should only be considered approximate (roughly  $\pm 20\%$ ).

### 5.2.6 Results and Discussion

PPMS and ac results near the lower transition for the pure samples are shown in Fig 5.6. There are difficulties in measuring latent heat with both ac and relaxation time calorimetry.

1. If free energy barriers are so large so that thermal hysteresis remains significant even for our slow drift speeds, the latent heat will not be observed at all with ac-calorimetry and will be improperly characterized with the PPMS measurement<sup>8</sup>.
2. More subtly, if the latent heat has a time constant much greater than  $\tau_{\text{int}}$  (away from the transition), the resulting measured latent heat can be frequency dependent<sup>2,45</sup>. However, if the hysteresis is negligible (i.e. less than  $\Delta T(\omega)$  or the step size, for ac and PPMS calorimetry respectively) and the transition “fast”, the latent heat contributes to the effective measured specific heat as  $C_{\text{p(effective)}} = c_{\text{p}} + dL/dT$  , where we assume that the latent heat is distributed over a temperature interval due to sample inhomogeneity (or experimental temperature gradients in the sample)<sup>2</sup>.

For  $\text{Ca}_3\text{Ru}_2\text{O}_7$ , we believe that we captured most of the latent heat because no significant hysteresis in the anomalies was observed ( $\Delta T < 0.1$  K) so that the free energy barrier is not large. The frequency independence of our results shows that the latent heat does not have an intrinsic time dependence other than that of the thermal degrees of freedom.

In particular, for the PPMS sample, measurements were made with several different-sized temperature steps, with very little change in the anomaly as shown in

Figure 5.4 for step sizes of 50 and 200mK, suggesting that unless the hysteresis is much wider, most of the latent heat has been captured. For the 0.36mg sample, we measured the specific heat for a variety of chopping frequencies (with  $\Delta T(\omega) \sim 1 / \omega$ ), again with negligible difference in results as shown in Figure 5.6, also indicating that the transition is not “sluggish”. For all samples, the anomaly is very sharp,  $\Delta T \sim 0.25\text{K}$ , as also observed by others<sup>6,7</sup>. The measured transition entropy,  $\Delta S \equiv \int dT \Delta C_p / T$ , is somewhat sample dependent but reasonably well defined, with an average value  $\Delta S = (0.31 \pm 0.08)\text{R}$ , very close to the value measured by McCall, et al.<sup>6</sup>. Again, the robustness of this value suggests that at least most of the latent heat is being captured in the specific heat measurements.

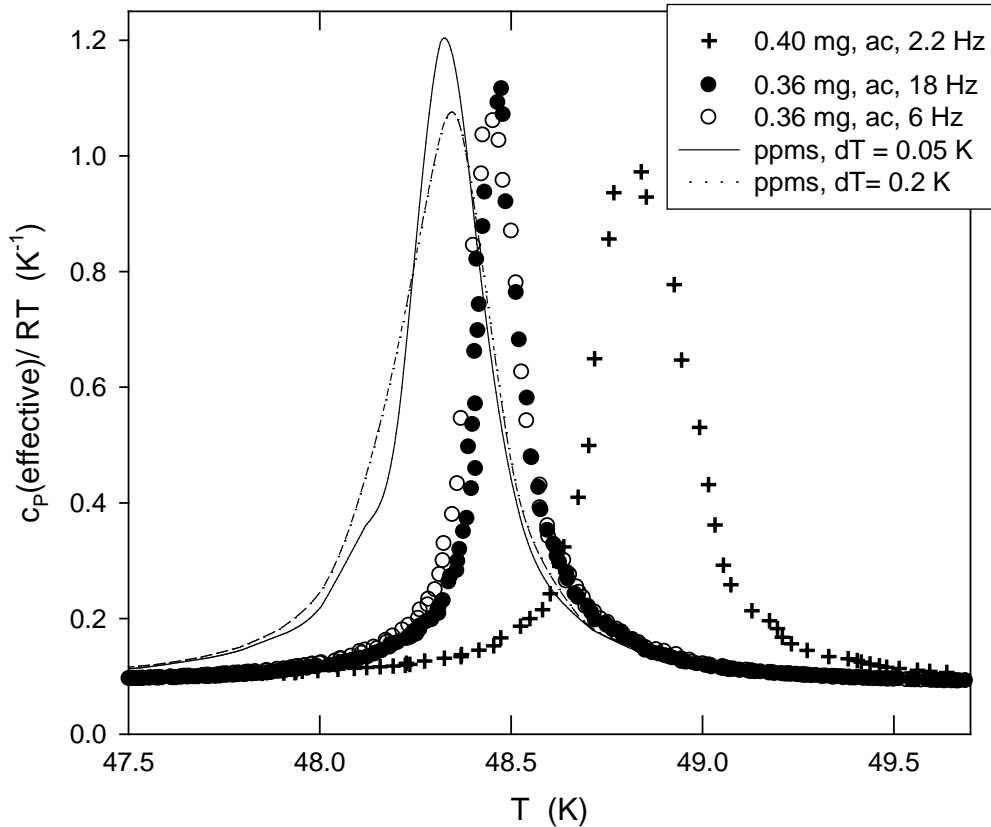


Figure 5.6 Effective specific heat (including distributed latent heat) for the pure samples, near the  $T_c$  structural transition, measured with different frequencies (ac-calorimetry) or temperature steps (PPMS measurements), as indicated<sup>66</sup>.



If this transition is due to formation of a charge-density wave as suggested by Baumberger, et al.,<sup>61</sup> then the expected entropy change  $\Delta S \sim \Delta\gamma \cdot T_c$  (assuming that fluctuation effects are negligible<sup>2,4,38</sup>, giving  $\Delta\gamma / R \sim 6 \times 10^{-3} \text{ K}^{-1}$ , i.e. the change in  $\gamma$  at the transition is significantly larger than its low temperature value, which is consistent with the low conductivity and/or lower dimensionality of the low temperature state.

Results for the transition at  $T_N$  for the pure and strontium substituted sample are shown in Figure 5.7. The anomalies are very similar. While our  $C_p$  anomalies are about twice those measured by McCall, et al.,<sup>6</sup> a simple estimate of the entropy change using the baseline shown,  $\Delta S \sim 0.036R$ , is very close to that of Reference [6]. Of course, the proximity of the large  $T_c$  anomaly makes reliably estimating an appropriate baseline difficult. It is clear, however, that  $\Delta S \ll 2R \ln(3)$ , the value expected for complete ordering of localized  $S=1$  spins. On the other hand, for antiferromagnetic ordering of itinerant spins, e.g. in a spin-density wave, we again expect  $\Delta S \sim \Delta\gamma \cdot T_N$ <sup>68, 69</sup>. Formation of a spin density wave is also consistent with the mean-field like step in the specific heat, for which we expect  $\Delta C_p \sim 1.43\Delta\gamma \cdot T_N$ . Then our measured anomaly  $\Delta C_p \sim 1.0R$  gives  $\Delta\gamma / R \sim 0.012 \text{ K}^{-1}$ . This value, greater than not only the low temperature value of  $\gamma$  but also the possible change at  $T_c$ , is much larger than expected, since the changes in conductivities at  $T_N$  are small. While the anomaly may be enhanced by low-dimensional fluctuations (effectively suppressing  $T_N$  below the mean field transition temperature<sup>4,38,67,68</sup>, this is unlikely to be a large effect here. Hence the specific heat anomaly at  $T_N$  is inconsistent with both conventional itinerant and localized pictures of antiferromagnetic ordering, suggesting a more complex spin ordering.

The effects of strontium substitution on the specific heat at  $T_c$  and  $T_N$  are shown in Fig 5.8. For the  $x = 0.15$  sample, the  $T_N$  and  $T_c$  anomalies separate to  $\sim 60 \text{ K}$  and  $45 \text{ K}$ , consistent with the magnetization data. The  $T_c$  anomaly is approximately symmetric, suggestive of a broadened first order transition; our estimate of the entropy with the baseline shown is  $\Delta S \sim 0.08 R$ , much smaller than for the pure sample, suggesting a smaller structural change and if electronic in origin, smaller change in  $\gamma$ . In contrast, the specific heat above  $T_N$  extrapolates to a lower value than that measured below  $T_N$ , as shown in the figure, so the anomaly appears to be “broadened mean-field”, with  $\Delta C_p \sim 0.7$

R, slightly smaller than for the pure sample. For the  $x = 0.58$  sample, we observe only a single “broadened mean-field” anomaly at  $T_N \sim 53$  K, with  $\Delta c_P \sim 0.4$  R. The decrease in magnitude of the  $c_P$  anomalies at  $T_N$  with Sr-substitution parallels the decrease in size of the magnetic anomalies, suggesting that Sr-substitution decreases either the magnitude or the average density of the ordering moments. The absence of a second anomaly for the  $x = 0.58$  sample suggests that the small resistance anomalies observed for this sample below 50 K are not due to thermodynamic transitions, but to changes in scattering as the spin state evolves.

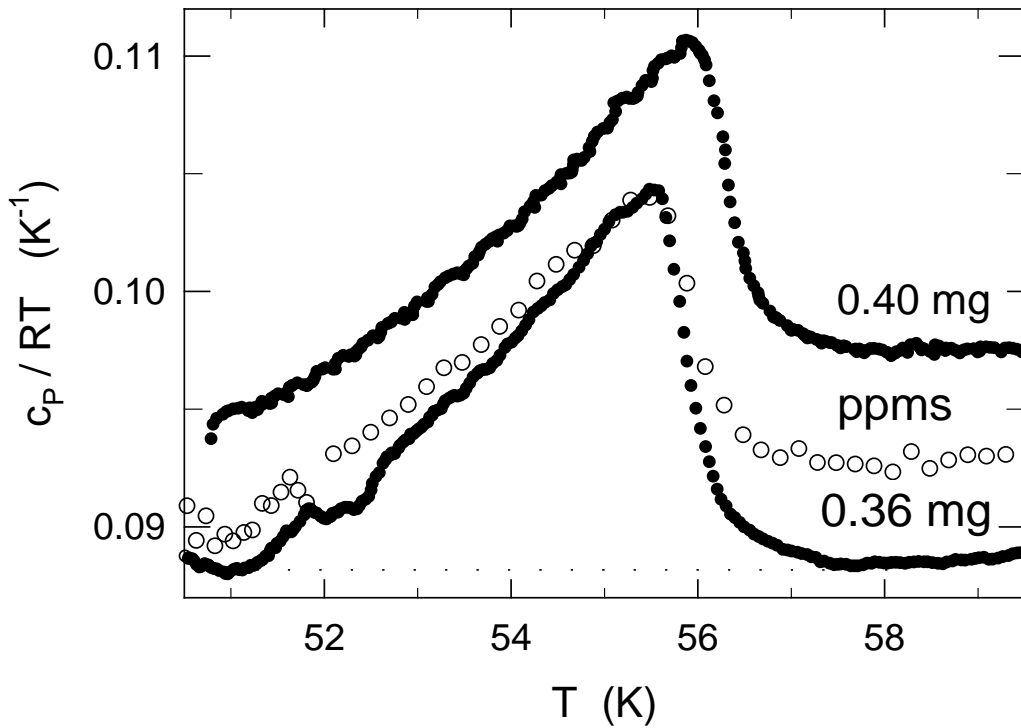


Figure 5.7 Specific heats of the pure samples near their Neel transitions. The dashed line for the 0.36 mg sample shows the background used to estimate the change in entropy<sup>66</sup>.

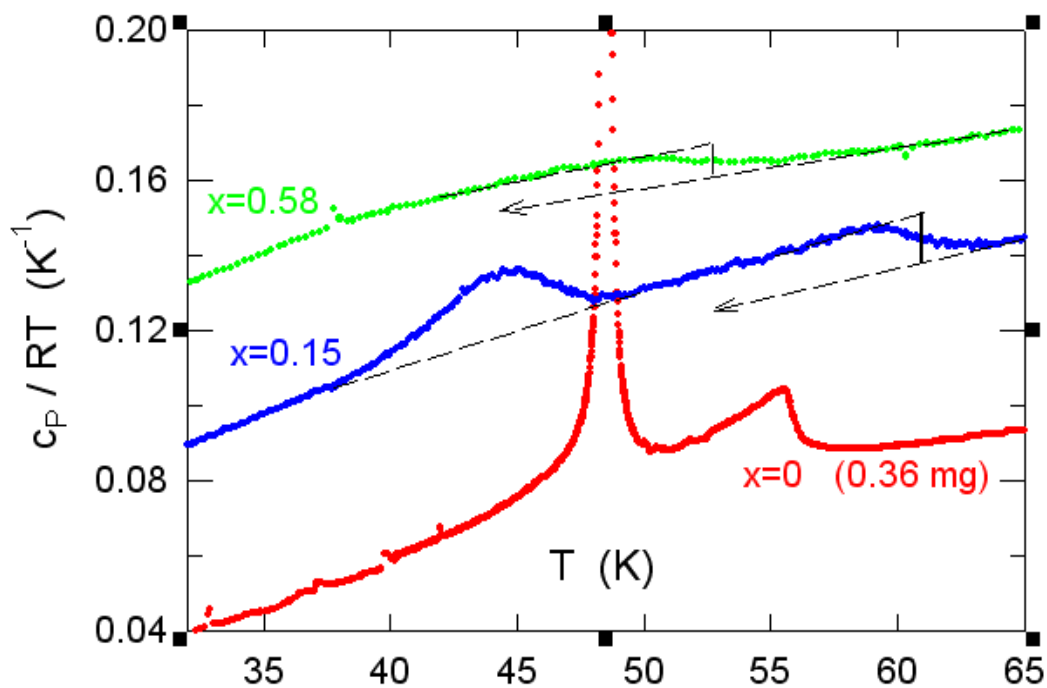


Figure 5.8 Specific heat, measured with ac-calorimetry, of pure and Sr-substituted samples, near the phase transitions. Data for the  $x = 0.15$  and  $x = 0.58$  samples are vertically offset by  $0.4 \text{ K}^{-1}$  and  $0.8 \text{ K}^{-1}$ , respectively. The dashed lines show the extrapolated temperature dependences and background used to estimate the changes in specific heats (shown by the heavy vertical lines) and entropy, respectively, for the substituted samples as discussed in the section<sup>66</sup>.

### 5.3 Specific heat of Fe<sub>2</sub>OBO<sub>3</sub> crystals

#### 5.3.1 The physical properties of Fe<sub>2</sub>OBO<sub>3</sub>

Fe<sub>2</sub>OBO<sub>3</sub> belongs to the warwickite family of compounds with chemical formula MM'OBO<sub>3</sub>, where M and M' are respectively divalent and trivalent metal ions<sup>70</sup>. The metal ions are found at the center of edge sharing oxygen octahedra which build ribbons as shown in Figure 5.9. The structures are held together by the Boron ions, which have only one crystallographic site with triangular coordination. The unit cell parameter of Fe<sub>2</sub>OBO<sub>3</sub> vary from  $a = 3.16879(8) \text{ \AA}$ ,  $b = 9.3835(3) \text{ \AA}$ ,  $c = 9.2503(3) \text{ \AA}$ ,  $\beta = 90.220(1)^\circ$  at 3K, to  $a = 3.1779(1) \text{ \AA}$ ,  $b = 9.3945(1) \text{ \AA}$ ,  $c = 9.2495(1) \text{ \AA}$ ,  $\beta = 90^\circ$  at 337K; the unit cell is orthorhombic at high temperature and becomes monoclinic at low temperature<sup>10</sup>.

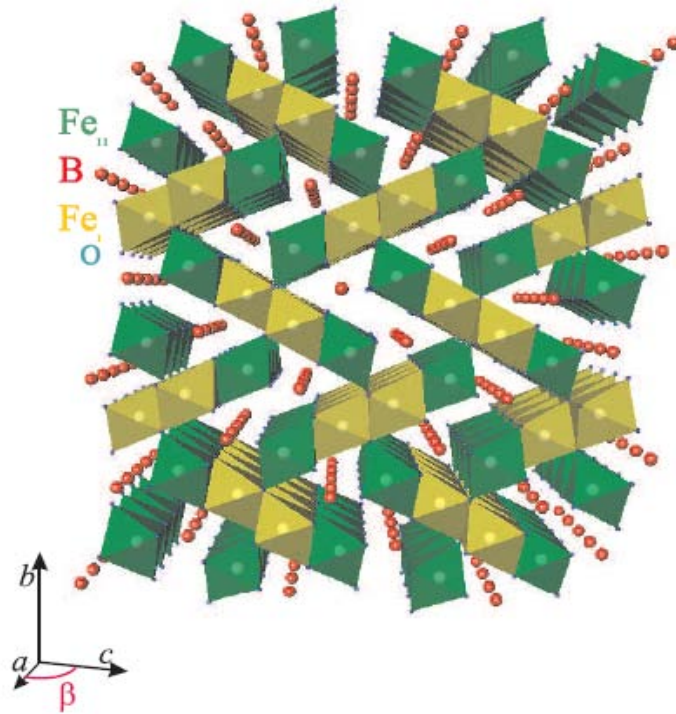


Figure 5.9 Crystal structure of Fe<sub>2</sub>OBO<sub>3</sub>. The unit cell is orthorhombic at high temperature. Structurally distinct Fe<sub>I,II</sub>O<sub>6</sub> octahedra build (Fe<sub>II</sub>-Fe<sub>I</sub>-Fe<sub>I</sub>-Fe<sub>II</sub> in the  $b$ - $c$  plane) ribbons of edge-sharing chains in the  $a$  direction<sup>71</sup>.

Mossbauer spectra on  $\text{Fe}_2\text{OBO}_3$  suggested a large, though not quantified, Fe valence separation below the onset of the monoclinic distortion of the structure at 317 K, thus suggesting that at high temperatures  $\text{Fe}^{2+}$  and  $\text{Fe}^{3+}$  cations occupy  $\text{Fe}_\text{I}$  and  $\text{Fe}_\text{II}$  sites with equal probability<sup>10</sup>.  $\text{Fe}_2\text{OBO}_3$  was therefore suggested to be an example of electrostatically driven Charge Ordering (CO)<sup>10</sup>; however, no experimental evidence of a CO superstructure was found on the available polycrystalline samples and consequently, the occurrence of CO in  $\text{Fe}_2\text{OBO}_3$  was under debate<sup>72</sup>.

### 5.3.2 Motivation

$\text{Fe}_2\text{OBO}_3$  is an interesting candidate to explore the charge ordering mechanism. This compound experiences an electrostatically driven charge ordering below 317 K<sup>69</sup> and orders antiferromagnetically below  $T_N = 155$  K. Differential Scanning Calorimetry (DSC) results from Oak Ridge indicated some feature at higher temperature (340 K) than the reported charge ordering. DSC and relaxation time calorimetry are not reliable methods to explore specific heats of sub milligram crystals, so a higher sensitivity technique is essential to examine the specific heat closely at these temperatures. We therefore used ac-calorimetry to measure the specific heat of flux grown needle shaped  $\text{Fe}_2\text{OBO}_3$  single crystals.

### 5.3.3 Sample preparation and Data

Needle-like single crystals of  $\text{Fe}_2\text{OBO}_3$  with length up to 1.5 cm were grown at Oak Ridge from a flux with a procedure similar to the growth of  $\text{Fe}_{1.91}\text{V}_{0.09}\text{OBO}_3$  reported by Balaev et al.,<sup>73</sup> except that  $\text{V}_2\text{O}_3$  was omitted from the flux to avoid V doping<sup>74</sup>.

The specific heat measurements were performed on three crystals of masses 0.31mg, 0.14mg, and on a tiny crystal of mass  $< 0.01$ mg with consistent results. The 0.31mg sample was attached to a thin (50-75 $\mu\text{m}$  diameter) Chromel-AuFe (0.07%) thermocouple using 6 $\mu\text{g}$  of silver paint. For the selection of chopping frequencies, representative frequency dependences of the ac voltage plots for the 0.31mg sample at 295 K and 110 K are shown in Figure 5.10. The typical chopping frequency used was 3 Hz. The temperature drift rate,  $|\text{dT}/\text{dt}|$  was kept under 0.1 K/min near the phase transition. The ac measurements were corrected for their addendum heat capacities (silver paint and

thermocouple) and normalized to published data by Continentino et al.,<sup>69</sup> at  $T = 200$  K and  $c_p = 0.614$  J/gK.

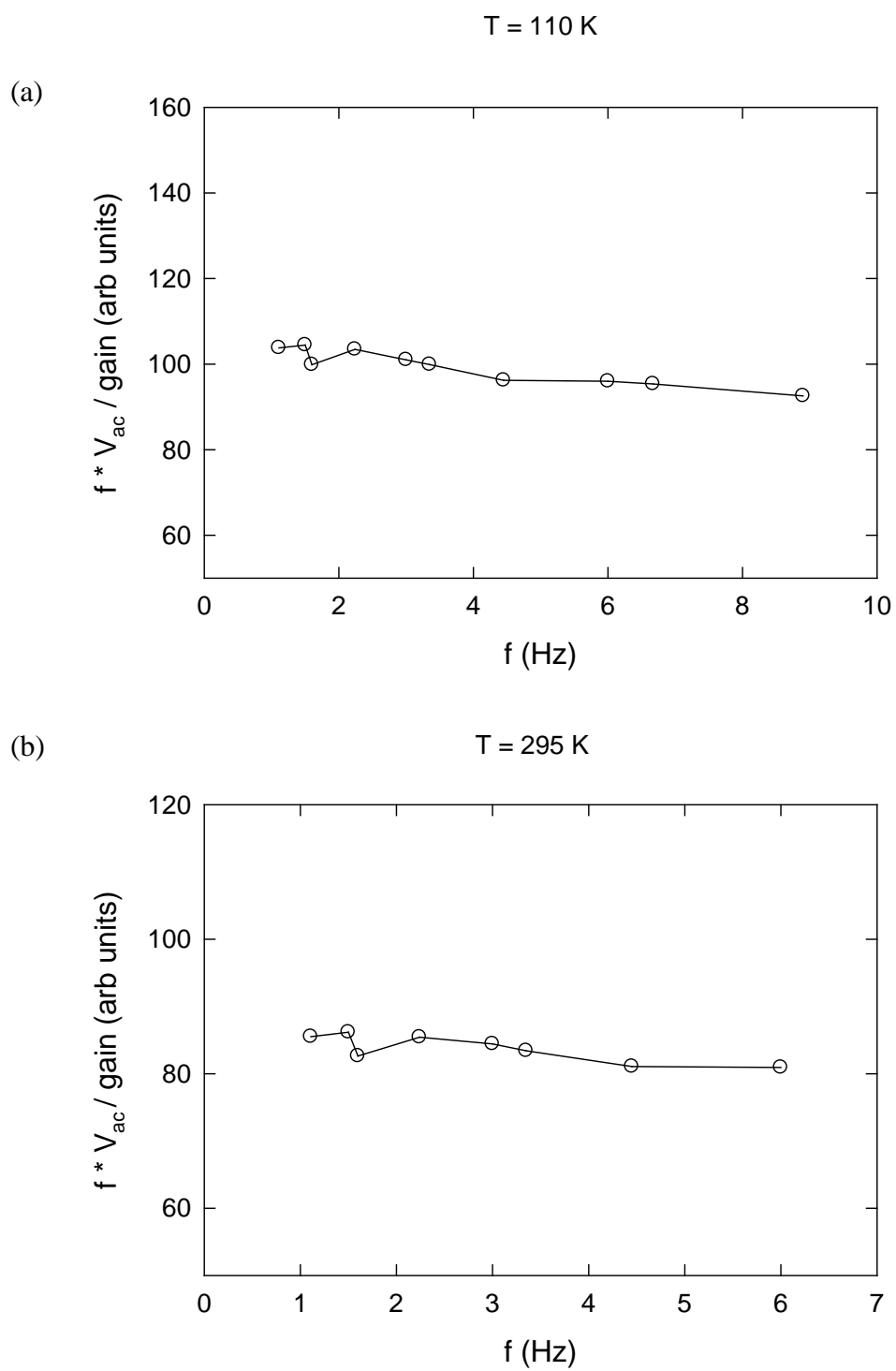


Figure 5.10 Frequency dependence of the ac voltage for 0.31mg sample.

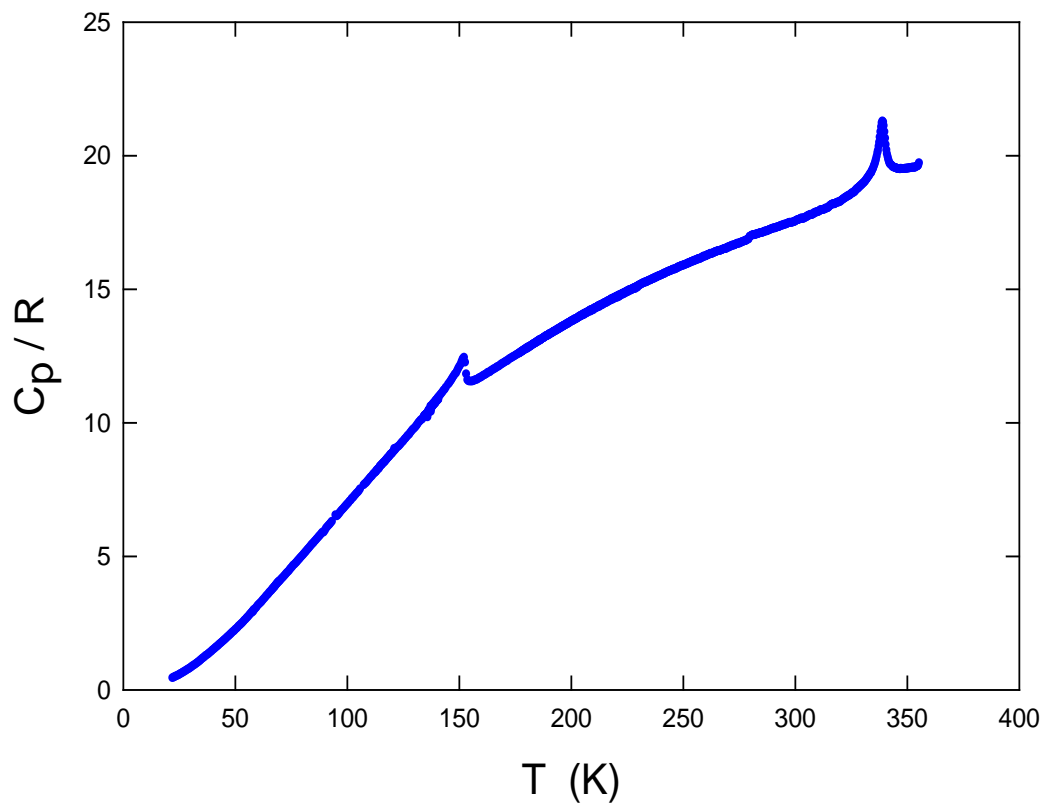


Figure 5.11 Specific heat of  $\text{Fe}_2\text{OBO}_3$  ( $m = 0.31\text{mg}$ ) over the entire measured temperature range in the units of R

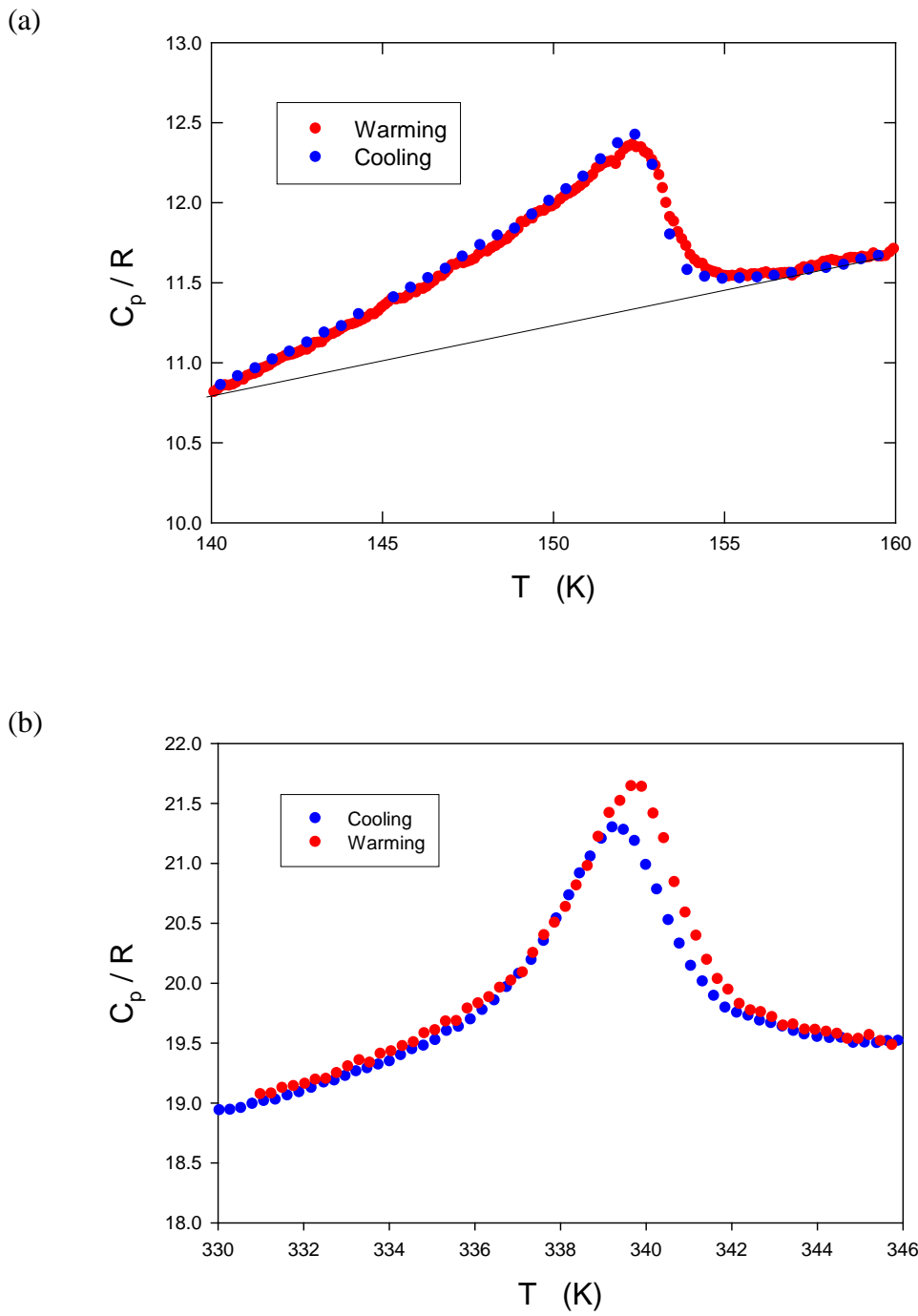


Figure 5.12 (a) Specific heat of  $\text{Fe}_2\text{OBO}_3$  ( $m = 0.31\text{mg}$ ) near the magnetic transition ( $T = 153\text{ K}$ ) (b) Specific heat of the sample near the structural transition ( $T = 340\text{ K}$ )<sup>73</sup>.



### 5.3.4 Results and Discussion

The specific heat measured with ac-calorimetry for the 0.31mg sample over the temperature range 20 K to 360 K, in the units of  $R$ , ( $R = 8.31 \text{ J/ mol K}$ ) is shown in Figure 5.11. Two anomalies were observed as shown in Figure 5.11. The anomaly at 153 K, shown in Figure 5.12(a), is associated with the magnetic transition and is similar to the results obtained by Continentino et.al.,<sup>69</sup> on polycrystalline samples. The data taken upon heating and cooling overlap and the transition looks fairly mean field with  $\Delta C_p \sim R$ .

Another striking feature observed is the transition at  $T = 340 \text{ K}$  shown in Figure 5.12 (b). It is slightly hysteretic ( $\sim 0.25 \text{ K}$ ) suggesting a weak first order phase transition which according to powder diffraction study<sup>75</sup> corresponds to the monoclinic-orthorhombic transition and which is associated with the onset of  $\text{CO}^{70}$ . We did data scans near the transition at several speeds and obtained the offset ( $\sim 0.25 \text{ K}$ ) in peak temperatures which confirms that the hysteresis is real and not instrumental. The hysteretic 340 K anomaly implies that we are observing only pre/post transition fluctuations in the specific heat. We probably are still missing any latent heat associated with the transition, which may be why the peaks observed in ac-calorimetry are smaller than those observed with DSC, which will include the latent heat. From ac-calorimetry, the estimated entropy change associated with the transition is very small  $\Delta S \sim 0.02 R$  but ac-calorimetry is sensitive only to the reversible heat flow, so will not observe hysteretic latent heat.

Differential Scanning Calorimetry (DSC) performed on crystals of the same batch (as those studied in ac-calorimetry) at the Oak Ridge Laboratory is shown in Figure 5.13 (b)<sup>76</sup>. Between 250 and 400 K, resistivity and DSC data show two separate well defined phase transitions on cooling (/warming) at 340 K and 280 (/310) K. The presence of an anomaly at 340 K is consistent with ac-calorimetry results (Fig 5.12 (b) ) but the transition at 280 (/310) K is absent in our measurements as shown in Figure 5.14. We did several scans in this region at different speeds on several crystals but our measurements did not show any anomaly. The probable reason for not observing the 280 (/310 K) anomaly is because ac-calorimetry is insensitive to irreversible contributions with hysteresis larger than the ac amplitude and indicates that the hysteresis is intrinsic and persists even at our very slow scanning speeds. In contrast, DSC is sensitive to all

contributions to the heat flow. The estimated entropy change through both transitions using DSC is  $\sim 0.6$  J/ (mol K) per Fe ion<sup>75</sup>. But even this value is  $\ll 2R \ln 2$  (first factor of 2 is because there are 2 irons/formula unit) expected for the proposed CO.

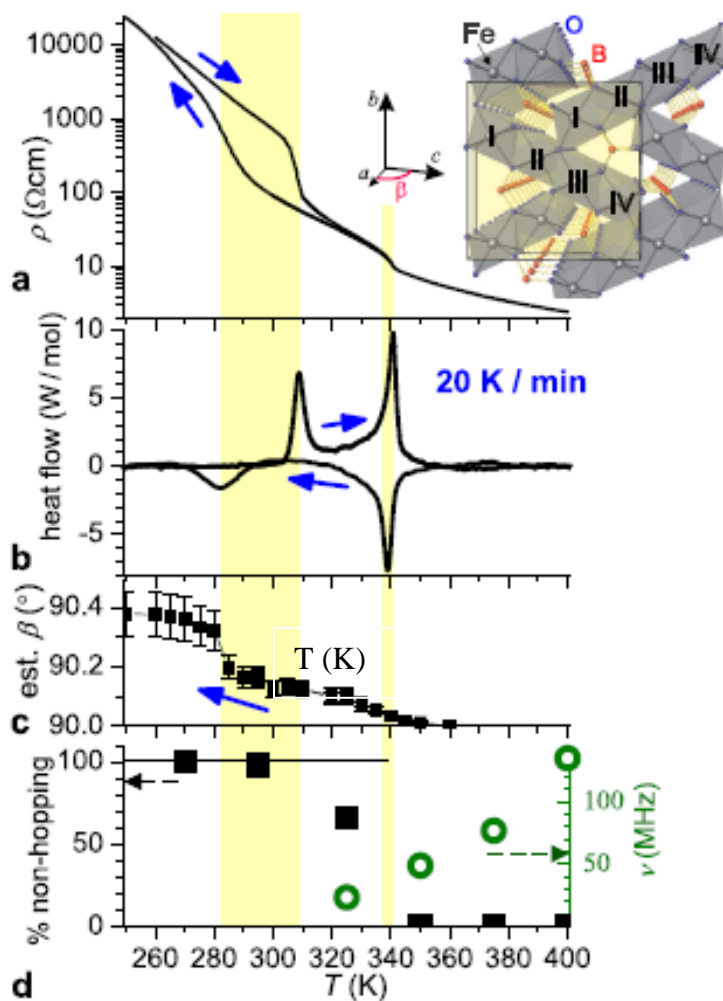


Figure 5.13 (a) Temperature dependence of resistivity  $\rho$  along a indicating two phase transitions (b) heat flow of differential scanning calorimetry (c) estimated monoclinic angle  $\beta$  (d) key parameters describing the Mossbauer spectra : fraction of the contribution to the spectra by Fe ions with no discernible electron hopping (  $\blacksquare$  , left) and hopping frequency  $\nu$  of the remainder ( $\circ$ , right). Inset in (a) Crystal structure at 355 K<sup>75</sup>.

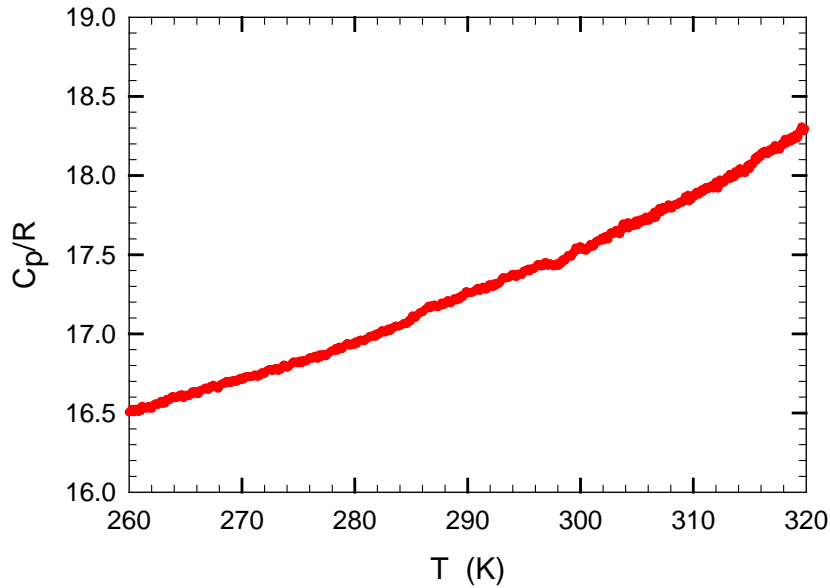


Figure 5.14 Specific heat of  $\text{Fe}_2\text{OBO}_3$  ( $m = 0.31\text{mg}$ ) single crystal between 260-320K showing no anomaly in (280/310 K) region.

After we completed our measurements on  $\text{Fe}_2\text{OBO}_3$  crystals, Dr. Angst Manuel from Oak Ridge reported the results in these crystals of X-ray diffraction, synchrotron X-ray scattering and Mossbauer spectroscopy measurements and electronic structure calculations<sup>73,75</sup>. Some important results are summarized here. Mossbauer spectra, obtained on powdered crystals using a constant-acceleration spectrometer<sup>77</sup>, indicate divalent and trivalent Fe ions distributed over two structural sites similar to previous results<sup>10,78</sup>. However, there is no discernible hopping of electrons between Fe ions at low T. In the intermediate T phase between the two transitions, e.g, at 325 K, contributions with and without electron hopping coexist as shown in Figure 5.13(d). Isomer shifts and quadrupole splitting are equal for both contributions and follow a standard T dependence.

X-ray scattering using synchrotron radiation suggests, differently ordered domains (likely up and down diagonal CO as shown in Figure 5.15(a)) of size large along  $a$  and  $b$  direction but small along  $c$  in the low T phase. These microdomains correspond to an imperfect overall CO, which is one reason for the lower-than expected entropy. In the intermediate phase, superstructure reflections are sharp along  $l$  and are split, corresponding to an incommensurate modulation with propagation vector  $(1/2, 0, \tau)$  and

$\tau(T)$  varying from about 0.4 at 340 K to 0.2 at 280 K. Above 340 K a long range ordered superstructure no longer exists, but very weak and broad reflections with  $(h+1/2, k, l+1/2)$  index indicate persistent short-range correlated fluctuations with correlations mainly along  $a$ , the chain direction. The correlations are not static, but the dynamics is relatively slow as shown in Figure 5.13(d). This dynamic short-range order likely also contributes to the missing entropy.

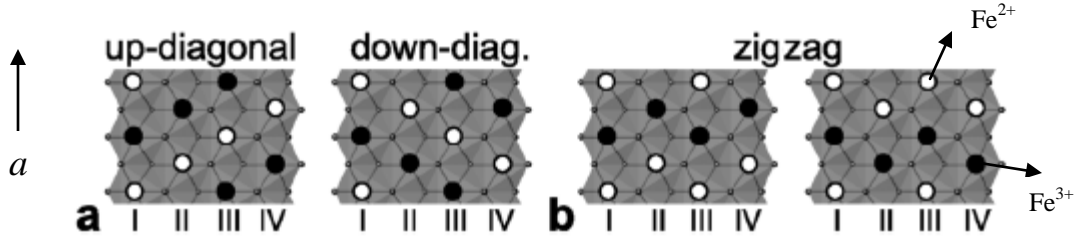


Figure 5.15 (a) The 2D lattice of chains consists of two sublattices offset from each other by  $a/2$ .  $\text{Fe}^{3+}$  and  $\text{Fe}^{2+}$  are drawn as filled and open circles respectively. Note that half the ion sites (e.g. sites II and IV on the bottom) remain intermediate valence and are not shown. Degeneracy of the two configurations leads to domain formation, with opposite sense of monoclinic distortion [41]. (b) Alternative “zigzag” CO with only slightly higher energy than the diagonal ground state. All other configurations are intermediate between diagonal and zigzag<sup>75</sup>.

Since the material is far from metallic (as seen from Figure 5.13 (a) and 5.13(d)), a nesting scenario cannot account for the incommensurate modulations in the intermediate phase. A better analogy to a case of perfect ionic CO is found in the chemical order of ions in binary alloys. In fcc-structured alloys, such as Cu-Au, incommensurate phases between chemically ordered (commensurate) and disordered phases are often observed and can be explained as a modulation with the statistical period arising from antiphase boundaries easily created due to degeneracy and frustration of the bonds on triangular networks<sup>79</sup>. Given that in the intermediate phase of  $\text{Fe}_2\text{OBO}_3$  the incommensurate modulation is in the  $c$  direction and the antiphase boundaries perpendicular to  $c$  are the ones with a small energy cost, a similar scenario may apply.

$\text{Fe}_2\text{OBO}_3$  is the first CO oxide in which the bond valence sum (BVS) analysis<sup>80</sup> indicates integer valence for both valence states. The valence separation is considerably larger than in the previously clearest examples  $\text{YBaFe}_2\text{O}_5$ <sup>81</sup> and related compounds and much larger than in the magnetites. The large valence separation suggests that  $\text{Fe}_2\text{OBO}_3$  is an ideal example of primarily electrostatic driven charge order. The reason that  $\text{Fe}_2\text{OBO}_3$  is unique among oxides in demonstrating ionic CO may be attributed to an antagonistic inductive effect<sup>82</sup> from the B-O bonds. Since B is more electronegative than Fe, O prefers to share its electrons with B, making the Fe-O bonds more ionic<sup>70</sup>. However, the CO is also affected by Jahn-Teller distortion of the  $\text{Fe}^{2+}$  octahedra.

#### 5.4 Conclusion

We have used ac-calorimetry to study the specific heat of  $(\text{Ca}_{1-x}\text{Sr}_x)_3\text{Ru}_2\text{O}_7$  and  $\text{Fe}_2\text{OBO}_3$  crystals. For  $\text{Ca}_3\text{Ru}_2\text{O}_7$  samples, we find that the large peak in effective specific heat at the  $T_C = 48\text{K}$  structural transition is independent of measurement times/frequencies suggesting a latent heat  $L \sim 0.31R$ , which decreases rapidly in magnitude with Sr substitution. The Neel transition anomaly observed at  $T_N \sim 56\text{K}$  is roughly mean-field in shape, but its magnitude ( $\Delta C_p \sim R$ ) is too large for a conventional itinerant electron spin-density-wave transition and too small to be associated with the complete spin-ordering of localized electrons. The magnitude of the anomaly decreases more slowly as Sr substitution decreases the spin order.

In the case of  $\text{Fe}_2\text{OBO}_3$ , two anomalies were observed. The transition at 155 K is mean field like with  $\Delta C_p \sim R$ . The structural transition at 340 K is slightly hysteretic ( $\sim 0.25\text{K}$ ) suggesting a weak first order phase transition which is associated with the onset of charge order. The hysteretic anomaly observed at 340 K anomaly implies that we are observing only pre/post transition fluctuations in the specific heat and we are probably still missing any latent heat associated with the transition. The transition at 280/(310 K) is not observed in ac-calorimetry because our technique is sensitive only to reversible heat flow. Superstructure reflections in  $\text{Fe}_2\text{OBO}_3$  arise from diagonal CO with two domains and Fe valence states very close to integer, suggesting that  $\text{Fe}_2\text{OBO}_3$  is an ideal example for ionic CO. An intermediate T phase of CO in the system is characterized by the coexistence of mobile and immobile carriers and by an incommensurate superstructure, the latter of which can be explained by specific antiphase

boundaries created easily due to geometrical charge frustration, similar to incommensurate chemical order

## Chapter 6

### Specific heat measurements in Magnetic Field

#### 6.1 Introduction

In this chapter, I will discuss the specific heat measurements using our in-field setup on two interesting candidates,  $\text{Sr}_4\text{Ru}_3\text{O}_{10}$  and  $\text{LaFeAsO}$ . The application of a magnetic field tends to align spins and usually suppresses spin fluctuations and hence the specific heat, but in the case of  $\text{Sr}_4\text{Ru}_3\text{O}_{10}$  there is a growing specific heat  $C$  with increasing field  $B$  at low  $T$ <sup>12</sup>. This interesting feature intrigued us to perform specific heat measurements on  $\text{Sr}_4\text{Ru}_3\text{O}_{10}$ . A detailed specific heat study on this sample is discussed in section 6.2.

$\text{LaFeAsO}$ <sup>15</sup> belongs to the iron pnictide-oxide family that has received much attention during the recent years and might be considered analogous to the cuprate high- $T_c$  superconductors. The undoped  $\text{LaFeAsO}$  is not superconducting but shows an anomaly near 150K which is believed to be due to a spin density wave (SDW) instability<sup>14,15</sup>. It would be interesting to study the progression of the SDW in the presence of a magnetic field using our new header. The specific heat study on  $\text{LaFeAsO}$  is presented in section 6.3.

#### 6.2 Specific heat measurements on $\text{Sr}_4\text{Ru}_3\text{O}_{10}$

##### 6.2.1 The physical properties of $\text{Sr}_4\text{Ru}_3\text{O}_{10}$

$\text{Sr}_4\text{Ru}_3\text{O}_{10}$  belongs to the Ruddlesden Popper Series  $\text{Sr}_{n+1}\text{Ru}_n\text{O}_{3n+1}$  with  $n=3$ . The orthorhombic unit cell of  $\text{Sr}_4\text{Ru}_3\text{O}_{10}$  is composed of triple layers of corner-shared  $\text{RuO}_6$  octahedra separated by double rock-salt layers of  $\text{Sr-O}$ <sup>5</sup>. A schematic of the crystal structure is shown in Figure 6.1, where the  $\text{RuO}_6$  layers are indicated as blue octahedra. The  $\text{RuO}_6$  octahedra in the outer two layers of each triple layer are rotated by an average of  $5.6^\circ$  around the  $c$  axis, while the octahedra of the inner layers are rotated by an average of  $11.0^\circ$  in the opposite direction<sup>5</sup>.  $\text{Sr}_4\text{Ru}_3\text{O}_{10}$  has a  $Pbam$  space group symmetry with  $a=b=0.39001$  nm and  $c=2.8573$  nm and contains two crystallographically independent triple layers<sup>5</sup>. The compound displays interesting phenomena ranging from quantum

oscillations<sup>11</sup>, unusual low temperature specific heat<sup>3</sup>, strong spin-lattice coupling<sup>83,84</sup> to switching behavior<sup>85</sup>.

Triple layered  $\text{Sr}_4\text{Ru}_3\text{O}_{10}$  is a structurally distorted ferromagnet with magnetic and resistive anomalies at  $T_C \approx 102$  K and  $T_M \approx 50$  K<sup>11</sup>. The properties of the material discovered from previous studies<sup>3,5,11-13,80,81</sup> are the following: 1) The  $c$ -axis magnetization  $M_C$  is ferromagnetic with  $T_C$  at 105 K followed by an increased spin polarization below  $T_M = 60$  K with large irreversibility upon in-field and zero-field cooling. In contrast, the  $ab$ -plane magnetization  $M_{ab}$  is much smaller and exhibits a weak cusp at  $T_C$  and a broad peak at  $T_M$ . 2) The isothermal magnetization  $M_C$  illustrates that the spins are readily polarized and saturated along the  $c$  axis at  $B = 0.2$  T, yielding a saturation moment at  $1.2 \mu_B/\text{Ru}$ . On the contrary,  $M_{ab}$  displays a first order metamagnetic transition at  $B_C$ .

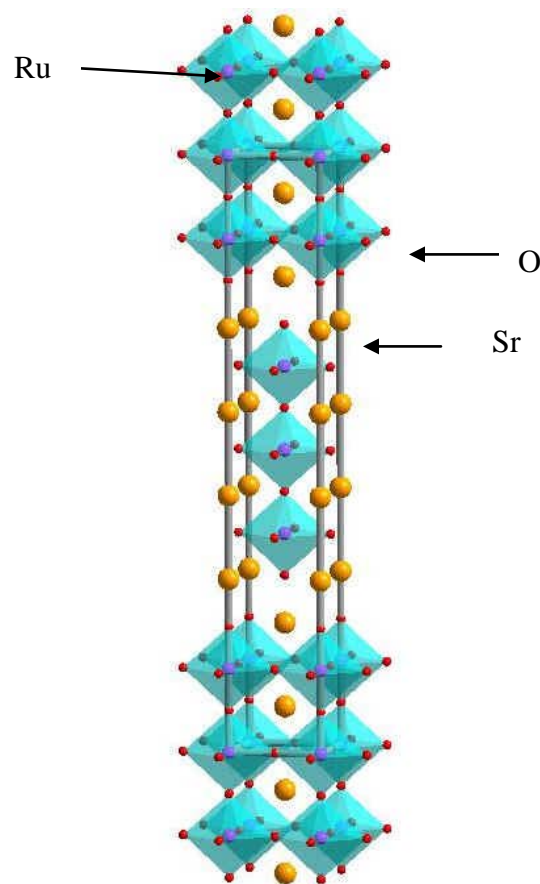


Figure 6.1 Crystal structure of  $\text{Sr}_4\text{Ru}_3\text{O}_{10}$  projected along the  $c$  axis<sup>86</sup>.



## 6.2.2 Motivation

We wanted to study a sample that has interesting features at low temperature and high magnetic field using our newly built header.  $\text{Sr}_4\text{Ru}_3\text{O}_{10}$  is one such sample that shows interesting behavior in specific heat at low temperature and high magnetic field. The key features from previous measurements<sup>12</sup> using PPMS on  $\text{Sr}_4\text{Ru}_3\text{O}_{10}$  are the following.

1. Figure 6.2(a)(b) shows  $C/T$  vs  $T$  for  $B // ab$  plane and  $B // c$  axis in the temperature range  $1.8\text{K} \leq T \leq 12\text{K}$ .  $C/T$  at low  $T$  ( $1.8\text{K} \leq T \leq 12\text{K}$ ) increases rapidly for  $B // ab$  plane, particularly in the vicinity of the metamagnetic transition, in contradiction to the anticipated behavior, implying a considerable enhancement of the quasiparticle effective mass in  $g(E_F)$ .  $C/T$  for  $B // c$  axis shows vastly different  $T$  dependence decreasing with increasing  $B$  for  $T > 6\text{K}$ , consistent with a suppression of spin fluctuations as anticipated for a regular magnetic state. However, it grows, though less drastically, for  $T < 6\text{K}$ , showing a broad peak near  $8\text{T}$ , suggesting that unexpected low-energy excitations develop in the spontaneous ferromagnetic state.
2. The unusual temperature dependence of  $C/T$  in fields is emphasized in Figure 6.2(c) for  $B // ab$  plane.  $C/T$  vs  $T^2$  shows negative curvature. The inset in the figure shows the sharp peak at  $2.5\text{K}$  for  $B = 5\text{T}$  that diminishes at higher fields and eventually evolves into a rapid downturn at  $9\text{T}$ .
3. For both  $B // ab$  plane and  $B // c$  axis,  $C/T$  for  $B \leq 2.7\text{T}$  and  $T < 10\text{K}$  follows a linear  $T$  dependence,  $C/T \sim a + bT$ . The rapid increase of  $a$  with  $B$  could be indicative of a Fermi liquid with a nearby two dimensional critical point<sup>87</sup>.

The anomalous behavior mentioned above intrigued us to examine  $\text{Sr}_4\text{Ru}_3\text{O}_{10}$  with our newly built header. After completing preliminary high temperature measurements near  $T_C$ , with  $B // c$ , however, we were not able to do low temperature measurements because we could not obtain samples with appropriate thermal time constants, especially for the more interesting  $B // ab$  – plane geometry.

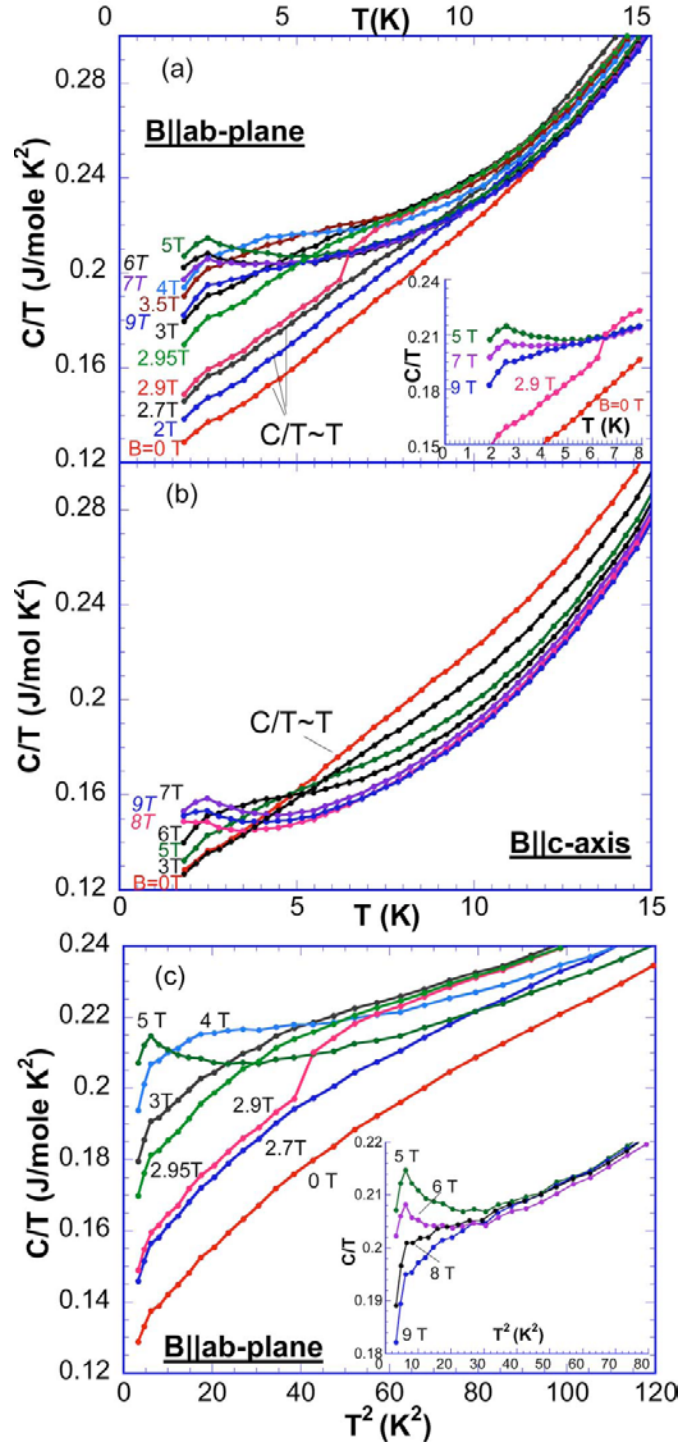


Figure 6.2 Specific heat divided by temperature ( $C/T$ ), as a function of  $T$  for (a)  $B // ab$  plane. (b)  $B // c$  axis (c)  $C/T$  for  $B // ab$  plane as a function of  $T^2$  for  $0 \leq B \leq 5T$ ; inset 1 shows  $C/T$  for  $B // a$  plane vs  $T$  for few representative fields; inset 2 shows  $C/T$  for  $B // ab$  plane vs  $T^2$  for  $5 \leq B \leq 9T$ <sup>12</sup>.

### 6.2.3 Sample preparation and characterization

The samples were grown by using the flux technique. Single crystals were grown in Pt crucibles from off-stoichiometric quantities of  $\text{SrCO}_3$ ,  $\text{RuO}_2$  and  $\text{SrCl}_2$  mixtures with  $\text{SrCl}_2$  being the self-flux<sup>12</sup>. The mixtures were first heated to 1480 °C in a Pt crucible covered by a Pt cover, soaked for 25 hours, cooled slowly at 2-3 °C to 1380 °C, then finally cooled to room temperature at 100 °C/h . These crystals are characterized by single crystal x-ray diffraction, electron dispersive X-ray (EDX) and TEM<sup>11</sup> and the results suggest that the crystals are of high quality with no impurity phases and no intergrowth.

### 6.2.4 Magnetic susceptibility data

The Figure 6.3 shows the temperature dependences of the magnetization  $M$  for the  $c$  axis and  $ab$  plane<sup>3,11</sup>.  $M$  for the  $c$  axis at  $B = 0.01$  T shows a Curie temperature  $T_C$  at 105 K, which is then followed by a sharp transition  $T_M = 50$  K. The irreversibility of  $M$  becomes large below  $T_M$ , consistent with a ferromagnetic behavior. However,  $M$  for the  $ab$  plane exhibits only a weak cusp at  $T_C$ , but a pronounced peak at  $T_M$ , resembling an antiferromagnetic like behavior and showing a much smaller irreversibility.

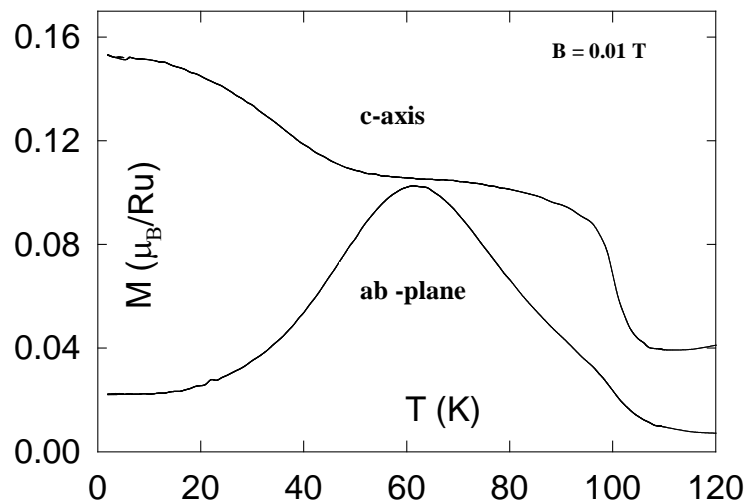


Figure 6.3 Magnetization as a function of temperature for the  $c$ -axis and  $ab$ -plane<sup>3</sup> at  $B = 0.01$  T.

The magnetic susceptibility for 150-350 K (not shown here) obeys the Curie-Weiss law, yielding highly anisotropic Pauli susceptibilities  $\chi_o$  of  $4.1 \times 10^{-3}$  and  $1.4 \times 10^{-4}$  emu/mole for the  $c$  axis and  $ab$  plane respectively<sup>11</sup>. The larger enhanced  $\chi_o$  for the  $c$  axis suggests a large density of states near the Fermi surface, in accord with the Stoner criterion for ferromagnetism that occurs along the  $c$  axis. On the other hand,  $\chi_o$  for the  $ab$  plane is more than an order of magnitude smaller than that of the  $c$  axis, implying a less energetically favorable condition for ferromagnetism.

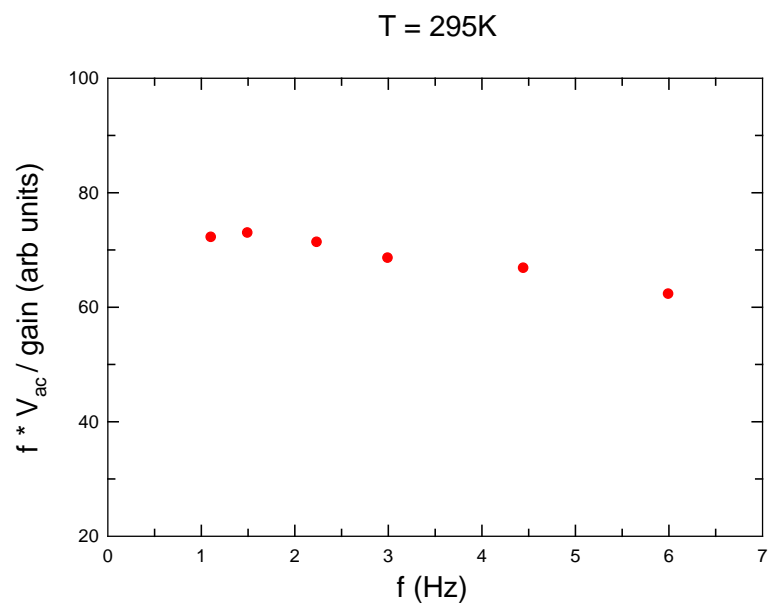
### **6.2.5 Zero field heat capacity data**

#### **6.2.5 (a) $c$ -axis sample at the magnetic transition**

Before doing measurements using the newly built header, zero field heat capacity data for the flux grown  $\text{Sr}_4\text{Ru}_3\text{O}_{10}$  single crystals were obtained using the ac calorimetry set up in our lab. A thermocouple was used as a thermometer to measure the specific heat in the temperature region 90 K–120 K. The sample of mass 0.288 mg was attached with silver paint to a flattened, 25  $\mu\text{m}$  diameter type E thermocouple junction. The typical chopping frequency used was  $\omega/2\pi \sim 1.5$  Hz. The  $fV_{AC}$  vs.  $f$  graph at  $T = 295$  K and 95 K is shown in Figure 6.4 (a) (b). The results were normalized at  $T=109.03$  K ( $C_p = 0.2280$ ) and corrected for addenda contributions with respect to the previously published results<sup>3</sup> from our lab. Figure 6.5 shows the previously published data from our lab for the image furnace and floating zone samples.

After measuring the time constants and ensuring that the data is clean, the sample holder was transferred to the new header. Figure 6.6 compares the zero field heat capacity data near the transition region  $T_C$  over the temperature range 90 K–115 K using the ac-calorimetry set up in our lab (old header) and the in-field setup (new header) in Dr.Cao's lab. The zero field measurements in the two headers are consistent, and also consistent with the previous data (Figure 6.5) from our lab.

(a)



(b)

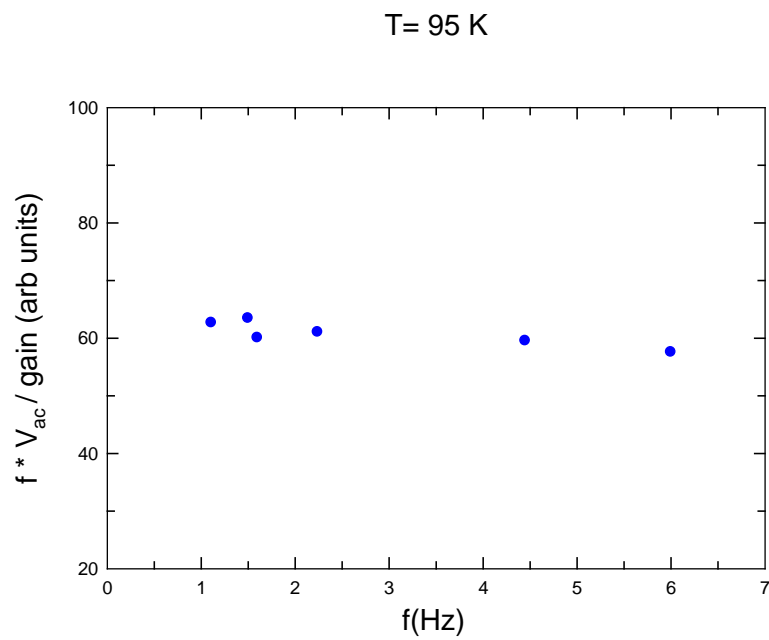


Figure 6.4 The  $fV_{AC}$  vs.  $f$  graph for  $c$ -axis at (a)  $T = 295$  K and (b)  $T = 95$  K.

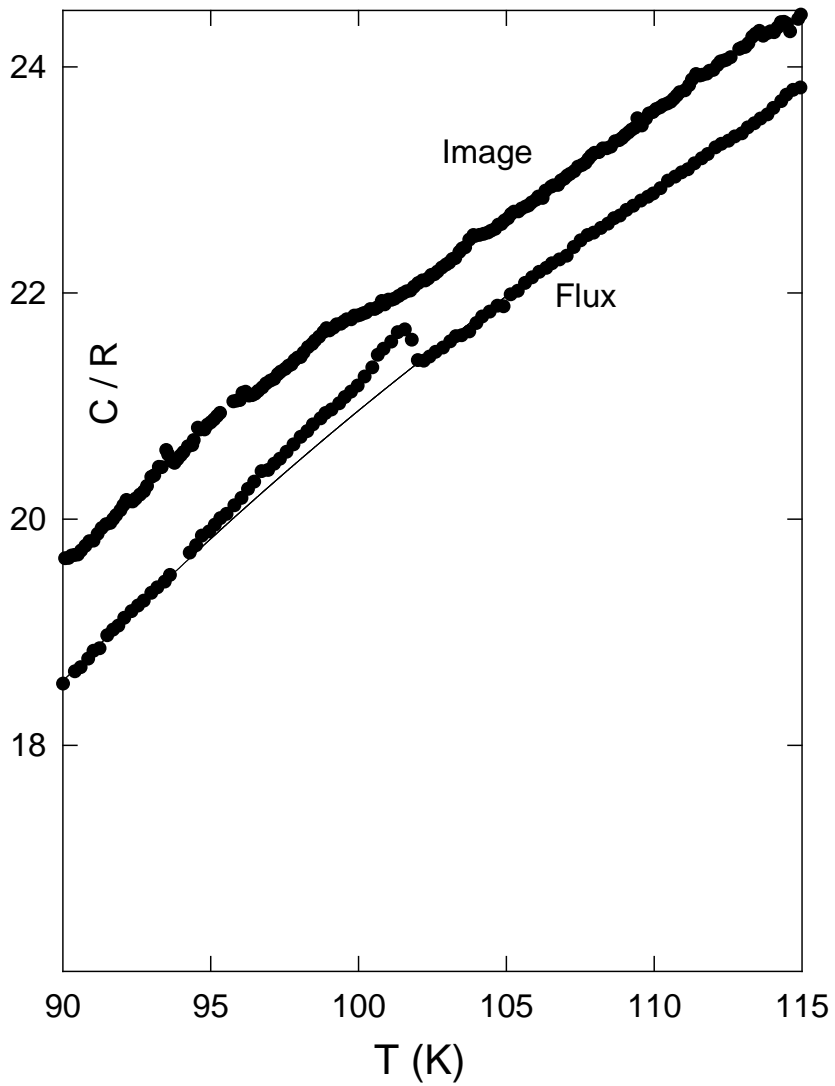


Figure 6.5 Temperature dependence of  $C_p/R$  for the image furnace and floating zone samples near  $T_C \sim 102 \text{ K}^3$ .

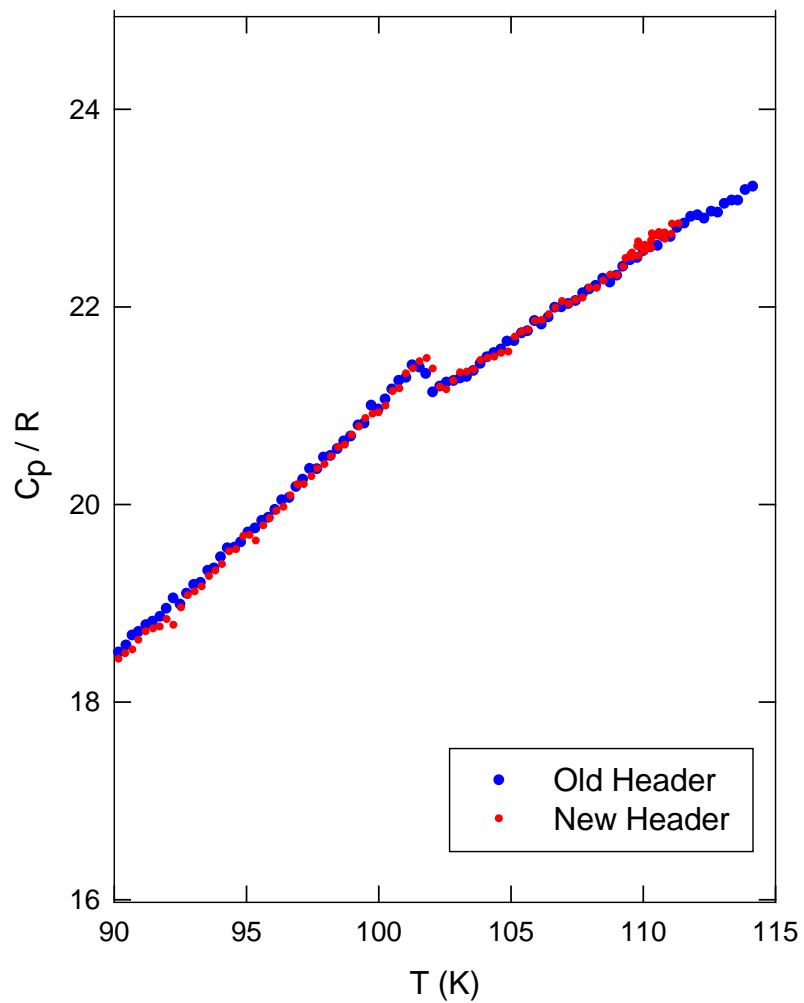


Figure 6.6 Temperature dependence of  $C_p/R$  near  $T_C \sim 102$  K for the flux grown sample along the  $c$  axis. The blue line is the measurement using the old header in our lab and the red line is the measurement in the in-field setup using the new header.

Following the zero field measurements in the in-field setup, field measurements were done on the  $c$ -axis sample. Figure 6.7 shows the temperature dependence of  $C_p/R$  near  $T_C = 102$  K for varying fields.

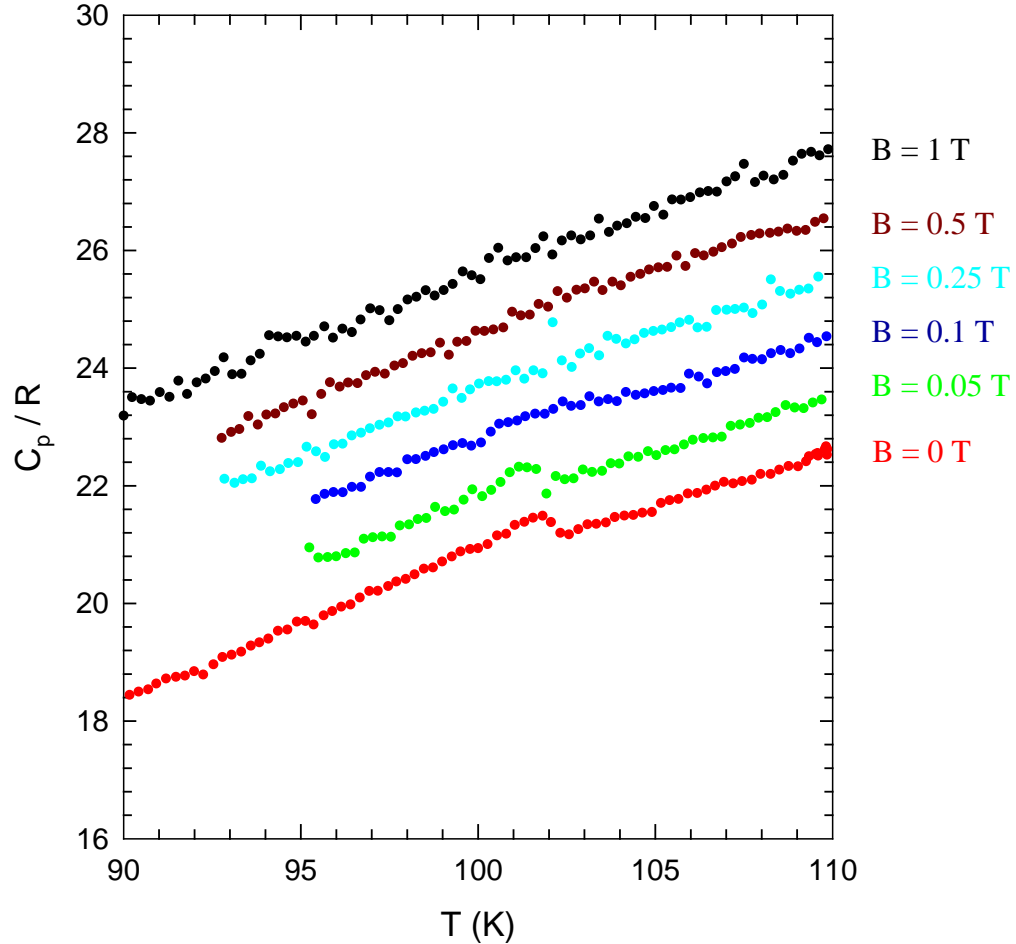


Figure 6.7 Temperature dependence of  $C_p/R$  near  $T_C = 102$  K for  $B // c$  axis. Data for  $B = 0.05$  T,  $B = 0.1$  T,  $B = 0.25$  T,  $B = 0.5$  T and  $B = 1$  T are vertically offset by 0.5, 1, 1.5, 2 and 2.5 respectively

All the in-field data were taken by warming with chopping frequency 1.5Hz. The measurements were taken according to the following procedure. Once the magnet is turned on and the current for the desired field is set, it takes a while for the magnet to reach the required field. During that time, the temperature controller is stabilized at the

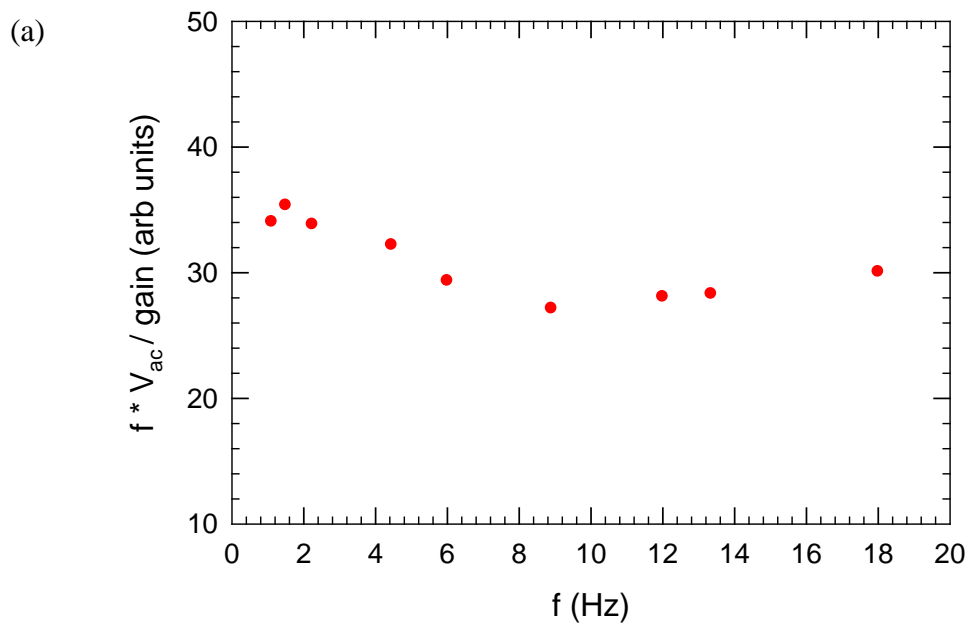


required temperature. Once the desired field is achieved, we start measuring the data from the stabilized temperature by warming. We started with 1 T, measured the heat capacity data in the temperature range 90 K–120 K; then decreased the field to 0.5 T, stabilized the temperature at 90 K and measured the second run. The field was then decreased to 0.25 T, 0.1 T, 0.05 T and the heat capacity was measured. Temperature drift rate,  $|dT / dt|$  was kept under 0.15 K/min for all the measurements. The results were normalized at  $T=109.03$  K ( $C_p = 0.2280$ ) and corrected for addenda contributions with respect to the previously published results from our lab.

### 6.2.5 (b) *ab*-plane sample at the magnetic transition

Specific heat measurements along the *ab* plane were attempted on two samples of masses 0.44 mg and 0.22 mg. The samples were attached with GE 7031 varnish to a flattened, 25  $\mu\text{m}$  diameter type E thermocouple junction. The  $fV_{AC}$  vs.  $f$  graph at  $T = 88$  K and  $T = 295$  K for mass = 0.44 mg sample is shown in Figure 6.8 (a) (b). As mentioned in chapter 3, the horizontal part of  $fV_{ac}$  vs.  $f$  curve gives the proper chopping frequency range at each temperature. We were not able to measure the heat capacity for the sample because it did not have an appropriate chopping frequency presumably because the light falling on the sample did not heat the sample as the heat got dissipated away quickly along the sides (i.e. we did not obtain one-dimensional heat flow). We measured the frequency dependence on a thinner sample (mass=0.22mg). The frequency dependence graph at  $T = 295$  K and 93 K at pressures 1 torr and 220 millitorr is shown in Fig 6.9 (a) (b). Again, we did not obtain a proper chopping frequency for this sample. We see that  $\tau_2$  is bigger and the inequality condition mentioned in chapter 3 is not satisfied and hence there is no proper chopping frequency to do the measurements for this sample along the *ab* - plane. The possible reason for not obtaining good time constant may be because the sample has a very small thermal conductivity along the *ab* - plane.

T = 88 K



T = 295 K

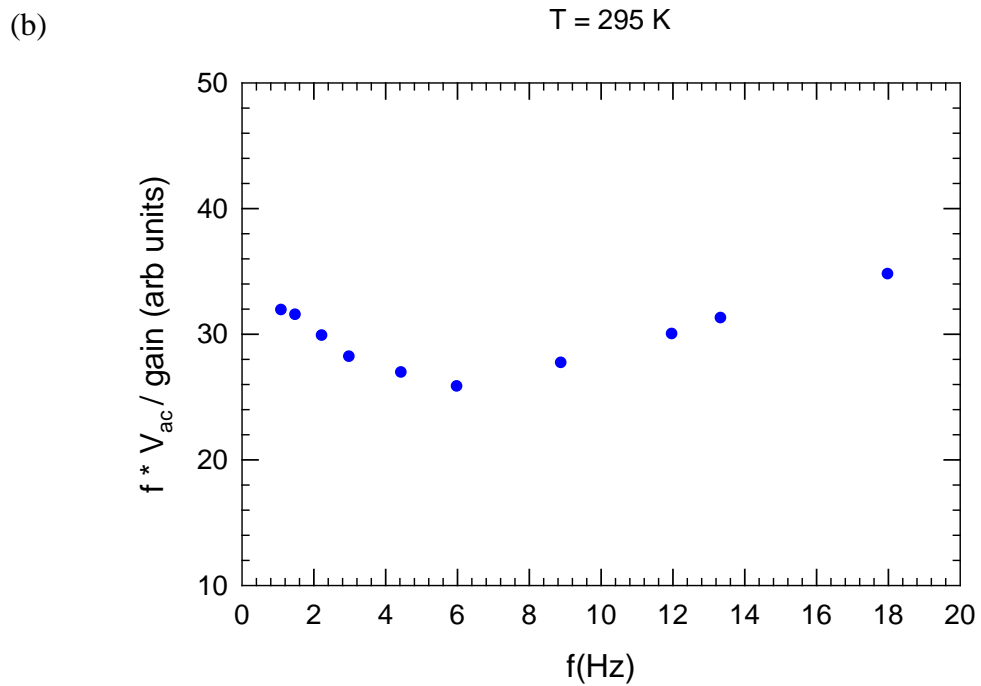


Figure 6.8 The  $fV_{AC}$  vs.  $f$  graph for  $ab$  plane at (a)  $T = 88$  K and (b)  $T = 295$  K for 0.44 mg sample

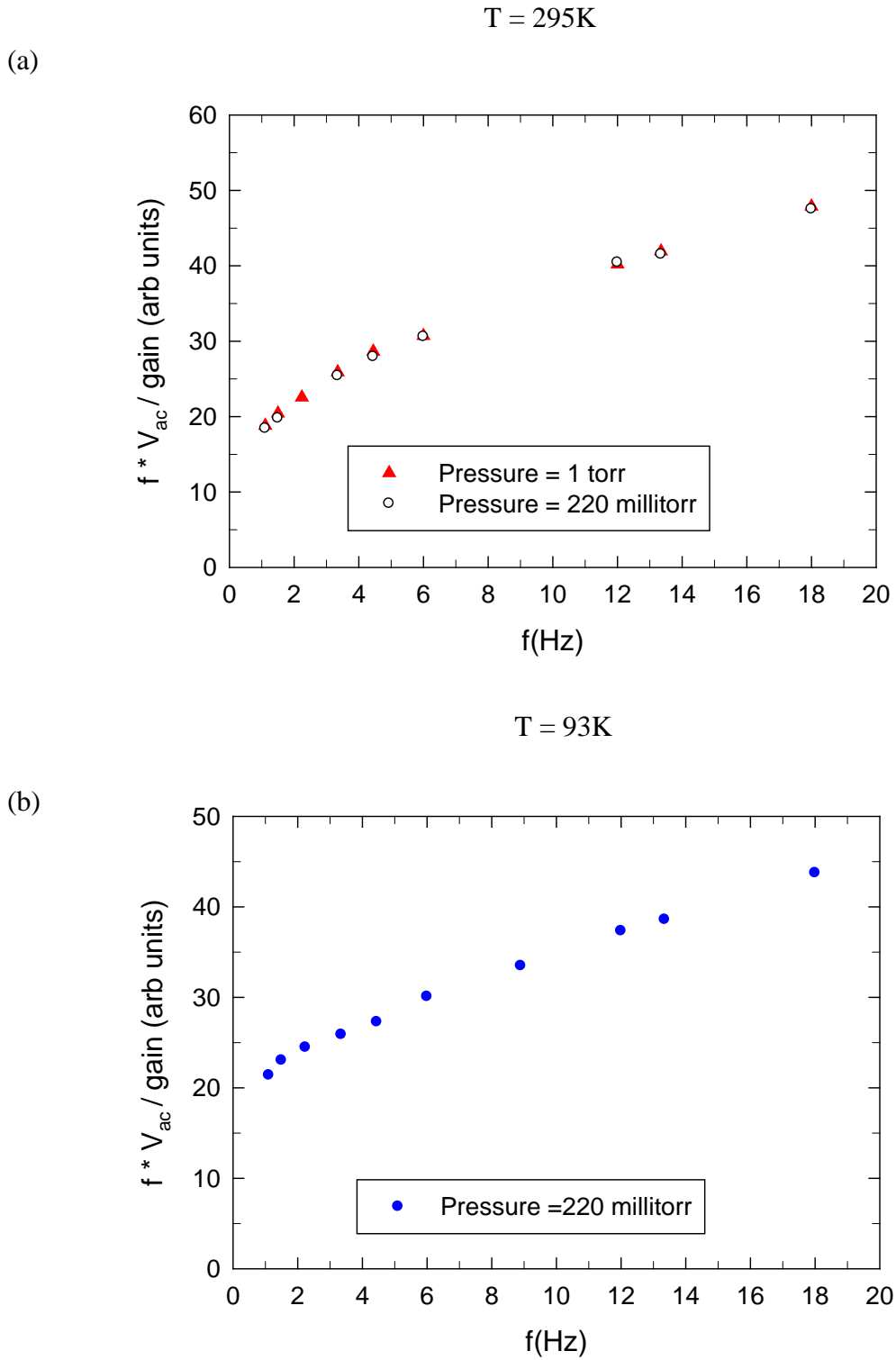


Figure 6.9 The  $fV_{AC}$  vs.  $f$  graph at  $T = 88K$  and  $T = 295 K$  for mass = 0.22mg

### 6.2.5 (c) *c*-axis and *ab*-plane sample at low temperature

In order to obtain low temperature measurements ( $< 20$  K), a Cernox 1050 BC type thin film resistance sensor is used. The *c* axis sample of mass 0.288 mg was attached to the sensor using GE 7031 varnish. The time constants for this sample were decent for 18 K, 12 K and 6 K but the zero field heat capacity data came out noisy for several repeated runs and so we did not pursue any field measurements.

Since, we did not obtain good time constants for the *ab*-plane sample, we did not do any field measurements as envisaged.

### 6.2.6 Discussion

The zero field temperature dependence of  $C_p/R$  near  $T_C \sim 102$  K for the *c* axis sample ( $m=0.288$  mg) is shown in Figure 6.10. An estimate of the entropy can be obtained from zero field measurement by drawing a baseline as shown in Figure 6.9. The sample exhibits a sharp mean- field-like step  $\Delta C_p \sim 0.4R$  at  $T_C \sim 102$  K. An approximate lower limit on  $\Delta S$  can be obtained by fitting the specific heat away from the transition to a smooth curve (shown in Figure 6.8) and measuring the area under the anomaly; in this case, we obtain  $\Delta S > 0.04R$ . On the other hand, an upper limit can be estimated from  $\Delta S \sim \Delta C_p$  ( $\sim 0.4R$ ), as expected for a mean field anomaly. For  $S=1$  system we expect the entropy to be  $R \ln 3$ . If all three spins/formula unit order, the expected entropy change is  $\Delta S = 3.3R$ . However, the estimated entropy change from the background chosen in the figure is an order of magnitude smaller than expected for complete spin ordering, suggesting that either the spin ordering is not spatially uniform or that only a small component of the spins order. It is noted that the magnetic entropy removal at  $T_C$  is generally small for weakly ferromagnetic metals, chiefly due to spin fluctuations.

Specific heat measurements using our newly built header in the presence of a field for  $B // c$  axis is shown in Figure 6.7 along with zero field measurements. A step in the specific heat is seen at 102 K for small values of the applied field (as low as 0.05 T). At an applied field of 0.1 T, the anomaly disappears. We expect the anomaly to broaden when  $\mu B \sim (\Delta S)T_C$ , which suggests that for  $\mu \sim 1.13\mu_B$  (reference 65),  $B \sim 53$  Tesla is the expected field where the anomaly should vanish. However, as seen in Figure 6.6, the anomaly vanishes at a much smaller field (0.1 T). This suggests that the the spin structure must be very complex (e.g. canted or helical structure).

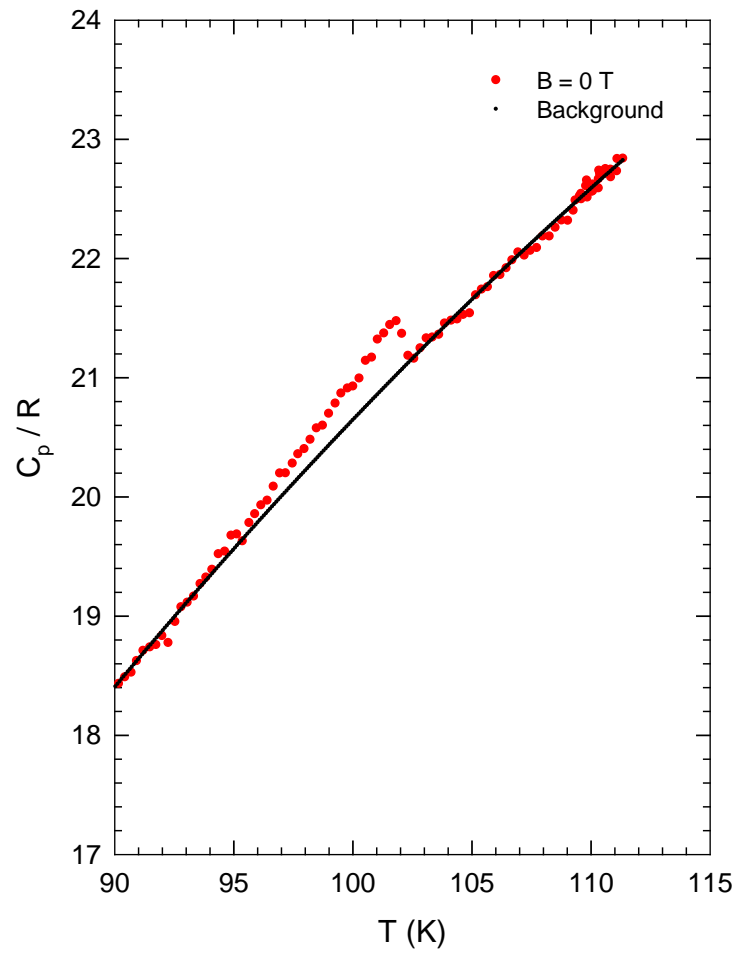


Figure 6.10 Temperature dependence of  $C_p/R$  near  $T_C \sim 102$  K for the flux grown sample ( $m = 0.288$ mg) along the  $c$  axis

## 6.3 Specific heat measurements on LaFeAsO

### 6.3.1 The physical properties of LaFeAsO

LaFeAsO belongs to  $\text{LnT}_M\text{PnO}$  family, where Ln represents 4f rare earth element,  $T_M$  – a transition metal element with a more than half-filled 3d shell, Pn– a pnico gen element and  $\Theta$  oxygen atom<sup>88</sup>. The parent compound in the family LaFeAsO crystallizes in the tetragonal ZrCuSiAs structure (space group  $P4/nmm$ ) with alternating FeAs and LaO sheets, where the Fe atoms are arranged on a simple square lattice as shown in Figure 6.11<sup>89</sup>. The lattice constants obtained for this material are  $a = 4.035(3.996)$  Å and  $c = 8.741(8.636)$  Å<sup>85</sup>. The compound involves different types of chemical bonding, which is strongly ionic in the LaO layers and rather covalent in the FeAs layers respectively. LaFeAsO undergoes a structural phase transition at low temperatures below 155K from tetragonal ( $P4/nmm$ ) to orthorhombic ( $Cmme$ )<sup>84</sup>. However, some confusion exists regarding the symmetry of the low-temperature structure<sup>84,90</sup>. It has been reported in both primitive monoclinic and c-centered orthorhombic space groups. In the monoclinic description, the atoms are very close to positions which would give orthorhombic symmetry. The orthorhombic description is probably correct since no indication of deviation from orthorhombic symmetry is observed in PXRD data<sup>91</sup>. The observed magnetic moment per Fe atom has been reported to range from  $0.25 \mu_B$ <sup>92</sup> to  $0.36 \mu_B$ <sup>86</sup> and lies in the ab plane. Such a low value of the magnetic moment is not expected because any application of Hund's rule to the Fe d states results in a moment of at least  $2 \mu_B$ . A theory proposed by Wu et.al<sup>93</sup> suggest that the combined effects of spin orbit, monoclinic distortion and p-d hybridization in tetrahedrally coordinated Fe in LaFeAsO invalidate the Hund's rule filling of the Fe d levels. The two highest occupied levels have one electron each, but as a result of differing p-d hybridizations, the upper level is more itinerant, while electrons in the lower level are more localized and hence the resulting magnetic moment is highly anisotropic.

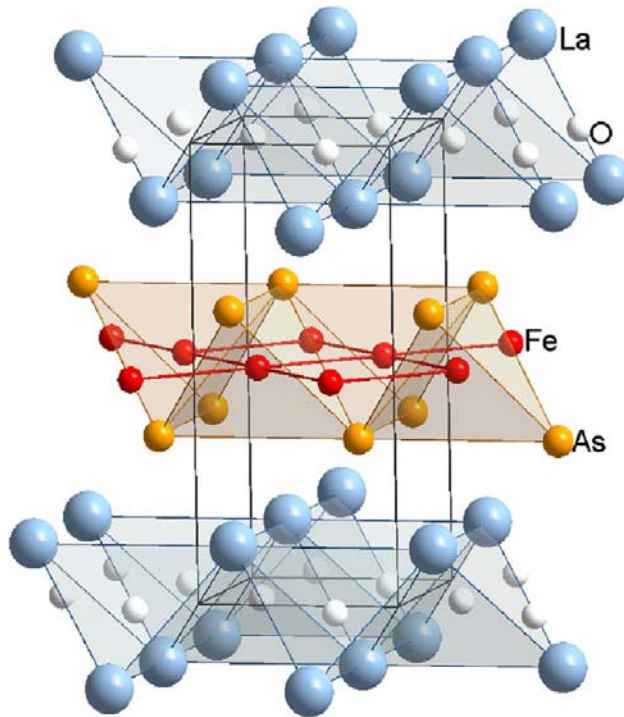


Figure 6.11 The structure of LaFeAsO consisting of alternating Fe-As and La-O layers. Fe and O atoms sit at the center of slightly distorted As and La tetrahedra<sup>85</sup>.

### 6.3.2 Motivation

The undoped parent material LaFeAsO has also been reported to undergo a spin density wave (SDW) transition near 150 K<sup>14,15</sup>. Structural measurements have indicated that the structure changes from tetragonal to orthorhombic at  $T_1=155$  K, while magnetic measurements indicated a magnetic transition into a spin-density wave state characterized by small periodic spatial oscillations of the iron spins at a slightly lower temperature<sup>14,15</sup>. At first it was assumed that these were the same transition, with different temperatures associated with different samples and measurement techniques and in fact calorimetric measurements with a commercial calorimeter could not resolve them as shown in Figure 6.12. A higher resolution technique is essential to examine the specific heat closely at these temperatures. We therefore used ac-calorimetry to measure the specific heat of LaFeAsO sample. In addition to zero field measurements, we did field measurements in this sample to investigate the progression of SDW in the application of field.

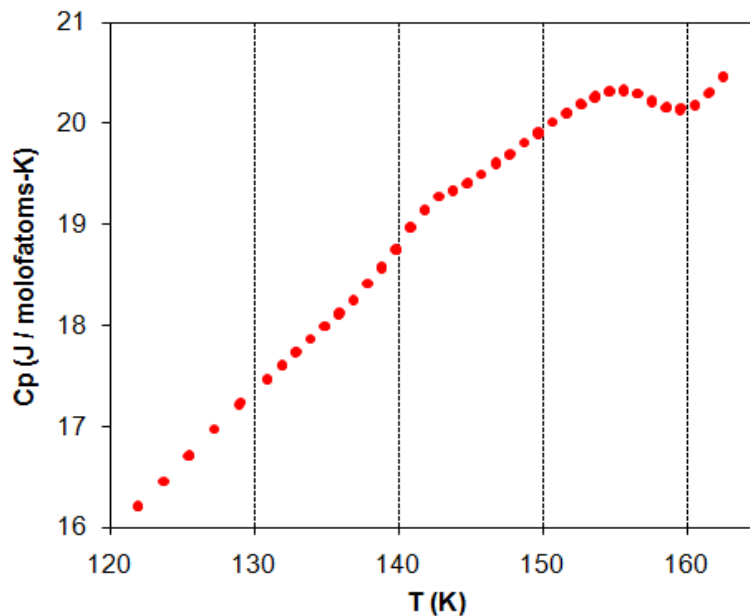


Figure 6.12 Specific heat measurement using PPMS on the LaFeAsO sample in which the two anomalies could not be resolved <sup>94</sup>.

### 6.3.3 Sample preparation and characterization

LaFeAsO was synthesized by Dr. McGuire at the Oak Ridge Laboratory by two methods<sup>87</sup>. The first method used finely ground stoichiometric mixture of LaAs, Fe (99.998%) and Fe<sub>2</sub>O<sub>3</sub> (99.998%) pressed into a pellet, wrapped in Ta foil and heated in a sealed silica tube partially backfilled with UHP Ar and with small piece of Zr and heated at 1200°C for about one day. Powder X-ray diffraction (PXRD) analysis showed the product to be nearly single phase LaFeAsO. The only other phases observed by PXRD were Fe and La<sub>2</sub>O<sub>3</sub>, while neutron diffraction experiments detected Fe<sub>2</sub>As. Rietveld analysis <sup>82,95,96</sup> indicates that the amount of impurities was less than 5%. Typical impurity phases in LaFeAsO samples are La<sub>2</sub>O<sub>3</sub> and FeAs probably due to unintentional excess oxygen in the starting materials. A second route used a finely ground mixture of FeAs, La<sub>2</sub>O<sub>3</sub> and La pressed into a pellet, sealed in a silica tube partially backfilled with UHP Ar and heated at 1200 °C for 30-36 hours. This method produced purer samples, sometimes with no impurities observable by PXRD. Materials prepared using the first method were used for zero field heat capacity measurements.



### 6.3.4 Heat capacity data

Zero field heat capacity measurements using ac calorimetry were performed on a 3.18 mg polycrystalline sample, using 4.5 Hz chopped light as a heating source in our lab. For the selection of chopping frequencies, representative frequency dependences of the ac voltage plots for the sample at 295 K and 103 K are shown in Figure 6.13 (a) (b).

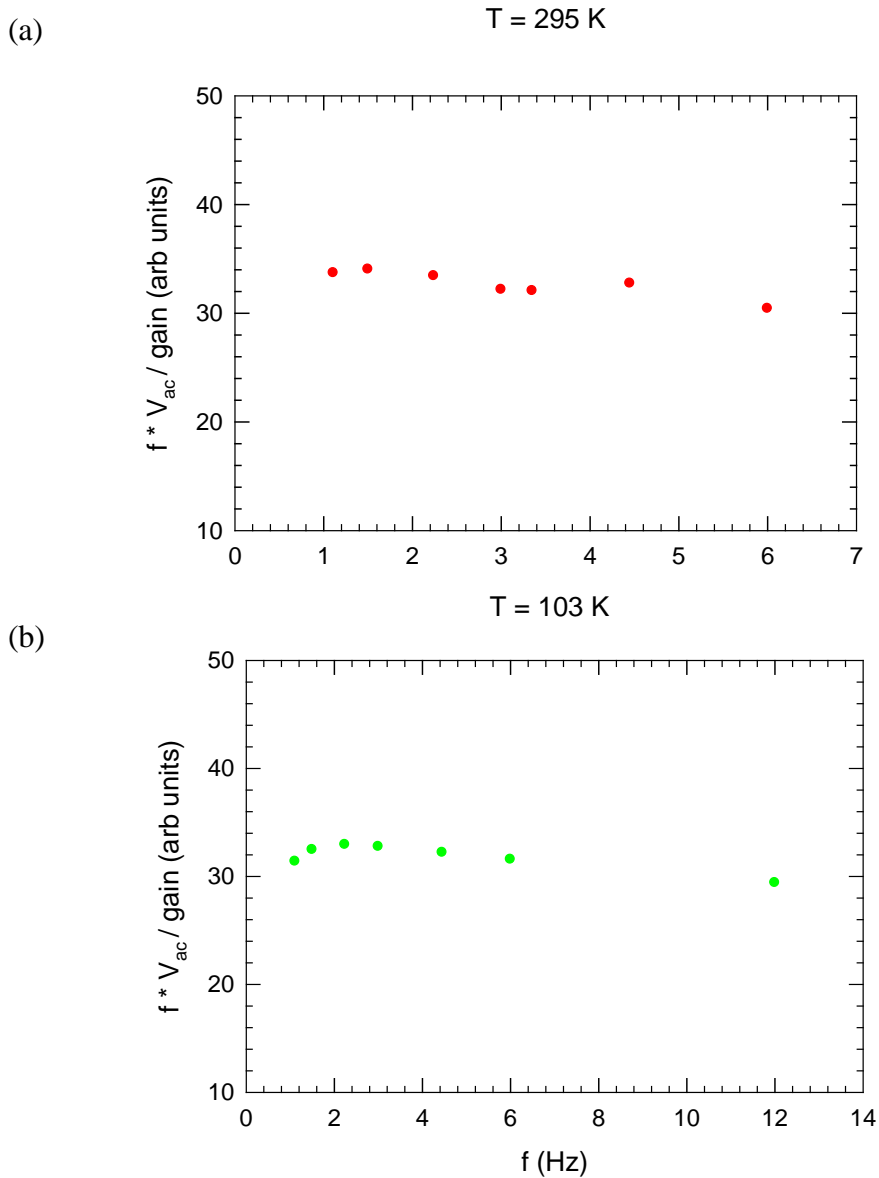


Figure 6.13 Frequency dependence of the ac voltage for 3.18 mg sample at a)  $T = 295 \text{ K}$  and b)  $T = 103 \text{ K}$

The average and oscillating temperatures of the back surface of the sample were measured with a 25 $\mu$ m diameter type-E thermocouple attached with varnish. The temperature drift rate,  $|dT/dt|$  was kept under 0.5 K/min near the phase transition. The molar heat capacity measured with ac-calorimetry for the 3.18 mg sample over the temperature range 120 K to 180 K, in the units of R, ( $R = 8.31$  J/ mol K) is shown in Figure 6.14. The data was then corrected for the addendum (thermocouple wire plus GE 7031 varnish) heat capacity, which was  $\sim 2.5$  % of the sample's in the temperature region measured. The ac measurements were normalized to the PPMS results obtained from Oak Ridge at  $T=127$  K. Since the PPMS results for this material have not been reliable, the normalization is only approximate, and giving a specific heat value of 90% of the Dulong-Petit value near room temperature.

We could not later perform field measurements on this sample since the zero field specific heat measurements using our new header did not show any anomaly and the data was inconsistent with our old header measurements. The reason for the inconsistent data may be because the sample properties changed when transferred from the old header to the new header, e.g. the sample absorbed moisture during that time as the sample has the tendency to absorb moisture when kept long at room temperature.

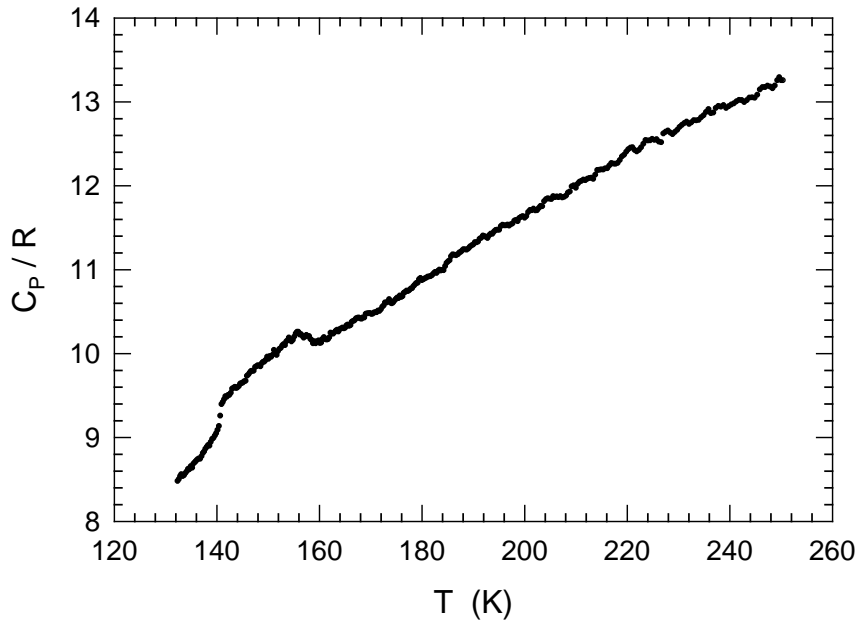


Figure 6.14 Specific heat of LaFeAsO ( $m = 3.18$  mg) over the temperature range 120K – 180K in the units of R.

Field measurements were performed in Dr. Cao's lab with our newly built header on a 13.45 mg polycrystalline sample attached to a 25 $\mu$ m diameter type E thermocouple with varnish. The chopping frequency used was 1.5 Hz. The  $fV_{AC}$  vs.  $f$  graph at 180 K and 130 K for the 13.45 mg sample using our newly built header is shown in Figure 6.15 (a) (b).

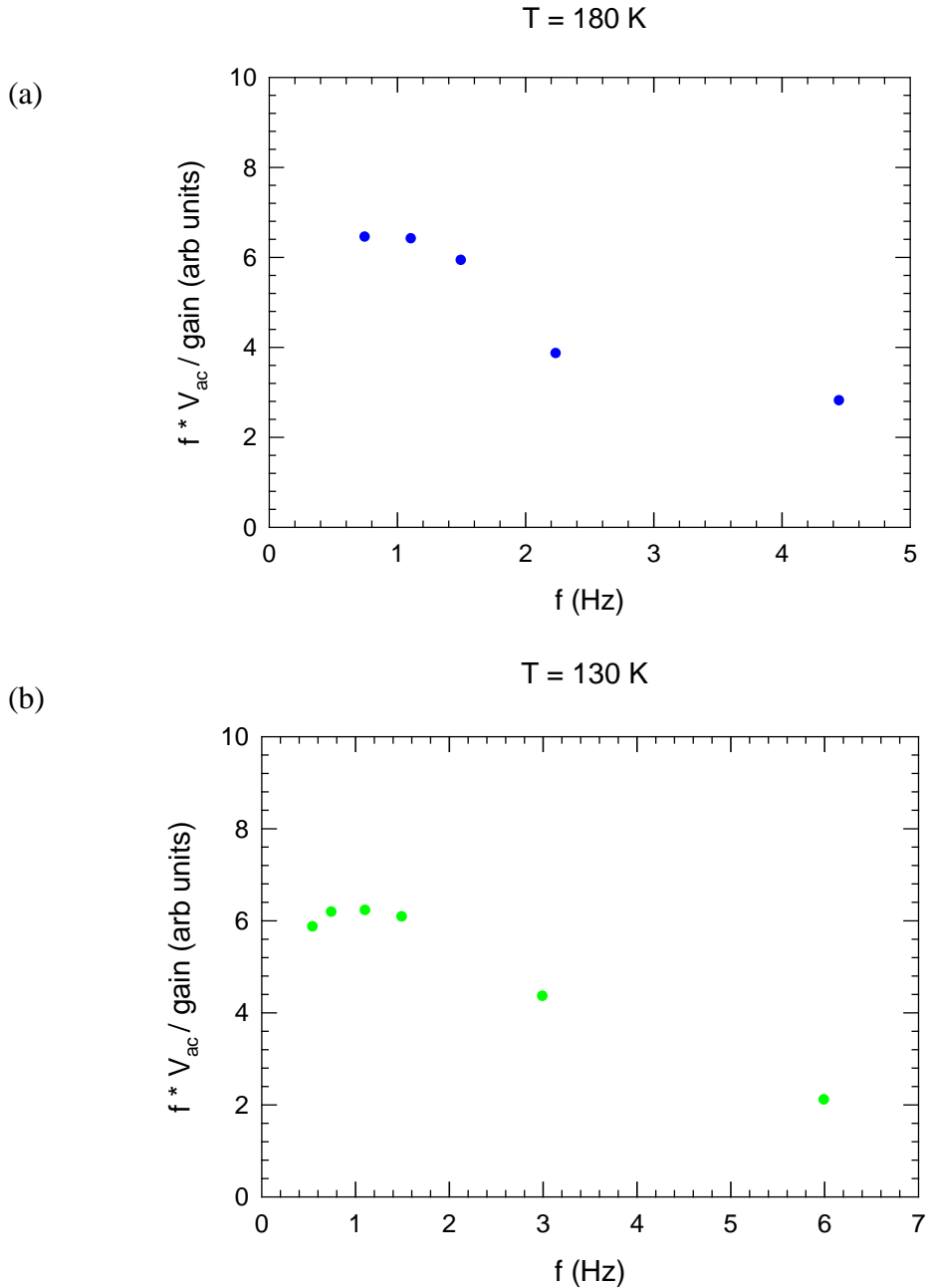


Figure 6.15 Frequency dependence of the ac voltage for 13.45 mg sample at a) T = 180 K and b) T = 130 K

After doing zero field measurement on the 13.45 mg sample, we switched on the magnet and raised the field to 11 T. The specific heat measured for this sample over the temperature range 120 K to 180 K, in units of R, ( $R = 8.31 \text{ J/mol K}$ ) for  $B = 0 \text{ T}$  and  $B = 11 \text{ T}$  is shown in Figure 6.16. The ac measurements were corrected for their addendum heat capacities (varnish and thermocouple) and normalized to PPMS results obtained from Oak Ridge at  $T=170.6 \text{ K}$ . The relative sizes of the anomalies in the two samples used in zero field and field measurements suggest that there may be sample dependence.

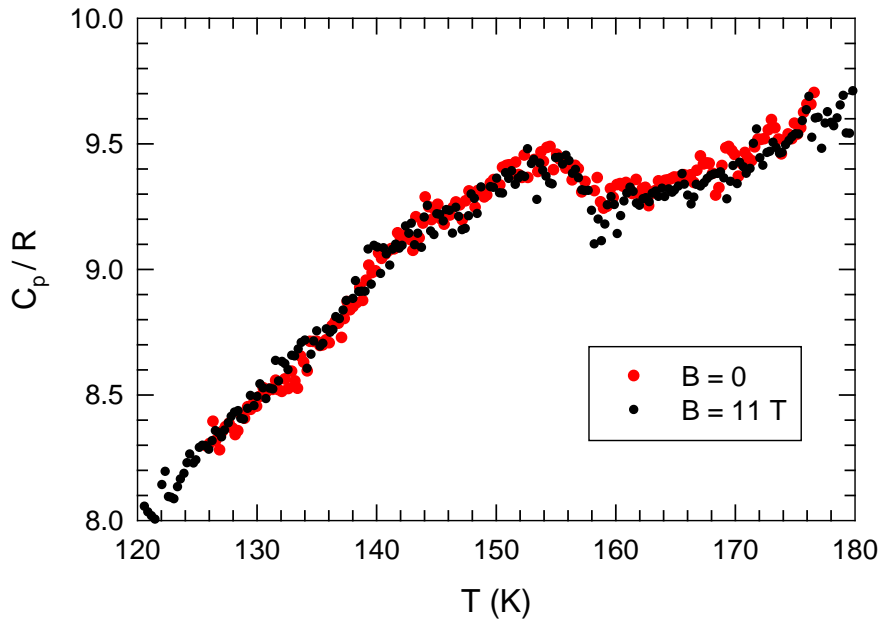


Figure 6.16 The specific heat of LaFeAsO ( $m = 13.45 \text{ mg}$ ) using our newly built header in zero magnetic field and in the presence of 11 T magnetic field.

### 6.3.5 Results and Discussion

The heat capacity of LaFeAsO of mass 3.18 mg sample in the vicinity of the structural and magnetic transitions is shown in Figure 6.14. Two broad overlapping anomalies are observed. The background was estimated by a polynomial fit to the data above and below the transition region as shown in Figure 6.17. The subtracted data in Figure 6.18(a) clearly show two peaks, one associated with the structural transition

centered at 155 K and one due to the magnetic transition centered at 143 K. The coincidence of these two peaks with the structural and magnetic phase transition temperatures strongly suggest that these are indeed separate anomalies, and not a single transition smeared by, for example, in homogeneities. The lack of thermal hysteresis ( $\Delta T_C < 0.1$  K) in these measurements suggests that the phase transitions are second order or only weakly first order. The anomalies do not look very mean-field like. The upper anomaly looks mean-field like above 150 K, but then it seems to get “cut off” by the lower anomaly. The entropy change determined by integration of the subtracted heat capacity data is shown in Figure 6.14(b), although, entropy estimates depend critically on choice of baseline. A total entropy of 0.032 R is determined by the integration. This is a very small entropy change for a structural transition, where roughly one might expect  $\Delta S \sim R$ . However, this small change in entropy is consistent with the Powder X-ray diffraction (PXRD) and Resonant ultrasound spectroscopy (RUS) results discussed in Reference [87] which suggest that the structural distortion occurs over a very broad temperature range and that the sharp transition at  $T_{T-O}$  makes only a small contribution to the overall crystallographic phase change. The feature at 155 K may indeed be more closely related to the behavior of the conduction electrons at  $T_{T-O}$  than the lattice. For the lower transition, if we assume mean-field theory with  $0.25R \sim \Delta c_p \sim \Delta\gamma T_C$ , we obtain  $\Delta\gamma \sim 10 \text{ mJ mol}^{-1} \text{ K}^{-1}$ . With the baseline shown in the Figure 6.13, it appears as if about one-third of the entropy is associated with the lower (magnetic) transition and two-third with the upper (structural) transition.

Specific heat measurements on the 13.45mg sample in zero magnetic field and  $B = 11$  T are shown in Figure 6.16. As seen in the figure, the applied magnetic field does not cause any significant change in the specific heat anomalies which implies that neither the structural transition nor the magnetic transition is affected much by the magnetic field. The application of magnetic field can cause two effects. On one hand, the applied magnetic field could depress the SDW order and decrease magnetic fluctuations. On the other hand, magnetic field might favor the Fermi surface nesting directly and then enhance the SDW gapping, which can lead to a decrease in the density of free charge carriers.

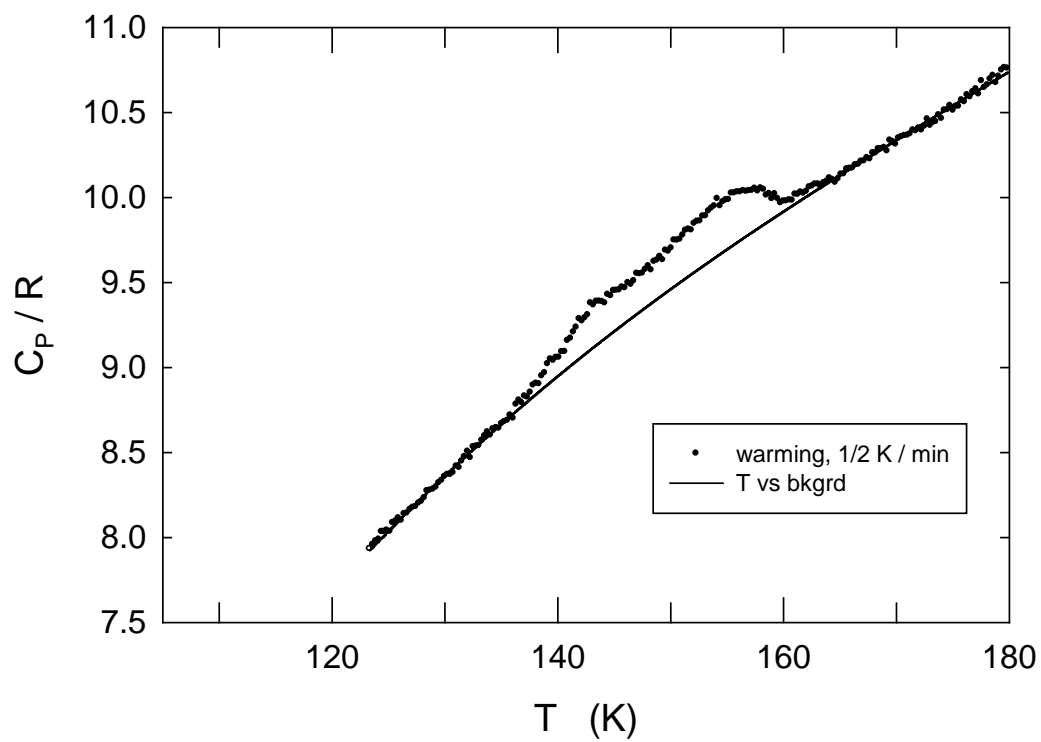
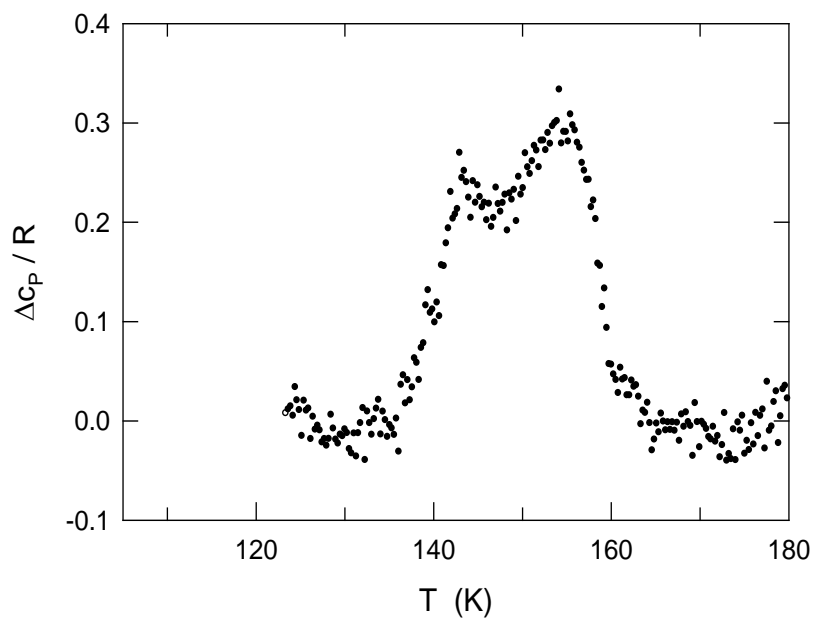


Figure 6.17 The specific heat of LaFeAsO ( $m = 3.18$  mg) with the background (solid black line). The background was estimated by a polynomial fit to the data above and below the transition region.

a)



b)

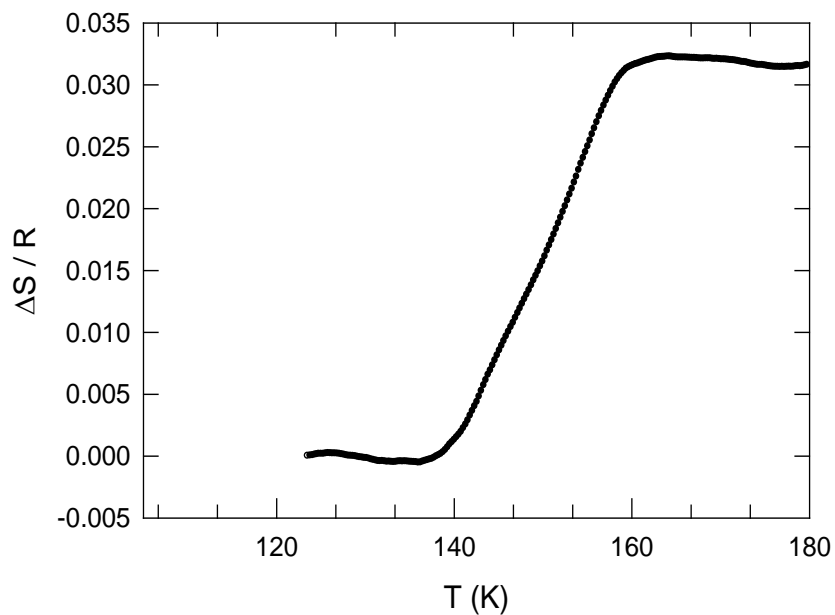


Figure 6.18 (a) The subtracted data of LaFeAsO ( $m=3.18$  mg) show two peaks, one associated with the structural transition centered at 155 K and the other due to the magnetic transition centered at 143 K. (b) The entropy change of LaFeAsO determined by integration of the subtracted heat capacity data.

According to a recent localized model proposed by Chen Fang et.al.<sup>97</sup>, there is a narrow range of temperatures above the magnetic ordering temperature, in which nematic order persists. The tendency toward nematic order lifts spin frustration and permits coupling. The nematic transition temperature  $T_N$  is determined by the following equation in the limit,  $J_Z \ll J_2$  [99] where  $J_Z$  is the interlayer coupling and  $J_2$  is the next-nearest-neighbor in-plane coupling

$$\frac{2\pi J_2}{T_N} = \ln \frac{J_2/T_N}{\sqrt{\left(\frac{K}{4\pi J_2}\right)^2 + \left(\frac{J_Z}{T_N}\right)^2 + \frac{K}{4\pi J_2}}} \quad (6.1)$$

where  $\vec{K} \sim 0.13 \vec{J}_1^2 S^2 / \vec{J}_2$  and  $\vec{J}_1$  is the nearest-neighbor coupling.

Let,

$$\lambda \equiv \sigma_{SDW} + J_Z/T \quad (6.2)$$

where  $\lambda$  is the Lagrangian multiples for  $\varphi_{n,\alpha}(\mathbf{r})$  and  $\sigma_{SDW}$  is the nematic order. Then the SDW transition temperature,  $T_{SDW}$  is determined by the following equations

$$\frac{\sigma_{SDW}}{2K} = \frac{1}{8\pi J_2} \ln \frac{2\sigma_{SDW} + \frac{J_Z}{T_{SDW}} + 2\sqrt{\sigma_{SDW}^2 + \frac{\sigma_{SDW} J_Z}{T_{SDW}}}}{J_Z/T_{SDW}} \quad (6.3)$$

$$\frac{\sigma_{SDW}}{2K} + \frac{1}{2T_{SDW}} = \frac{1}{4\pi J_2} \ln \frac{J_2}{J_Z} \quad (6.4)$$

Solving the above two equations, the model has two second order phase transitions. The nematic transition temperature  $T_N$  is always larger than the SDW transition temperature  $T_{SDW}$ .

From equation 6.4, we obtain  $T_{SDW} \sim \frac{J_2}{\ln(J_2/J_Z)} \ll J_Z$ . Since  $\vec{J}_Z$  is small,

( $\vec{J}_Z \sim 10^{-4} \vec{J}_2$ ), reduces  $T_{SDW}$ , while field as high as  $B \sim J_z / \mu \sim 10 \text{ k T}_{SDW} / \mu \sim 65 \text{ T}$



taking  $\mu \sim 0.35 \mu_B$ , is expected to cause a change in the anomaly. This is consistent with what we observed in our experiment, where the application of 11 T did not cause any obvious change in the specific heat anomalies.

After we completed our measurements on the LaFeAsO sample, Dr. McGuire from OakRidge reported the results in this sample on neutron diffraction, transport and magnetic properties<sup>87</sup>. Some important results are summarized here. Neutron diffraction data indicates additional scattering below 150 K in LaFeAsO consistent with a commensurate ordering wavevector of (0.5, 0.5, 0.5). This indicates a doubling of the conventional unit cell along both a-axes and along the c-axis and is also consistent with previous reported measurements by Dong et al<sup>15</sup>. The results of resistivity measurements are shown in Figures 6.19. The electrical resistivity is seen to drop dramatically at the SDW transition. At room temperature  $\rho$  has a value of 4 m $\Omega$ cm and decreases upon cooling. This is typical of a low carrier concentration metal or heavily doped semiconductor<sup>87</sup>.

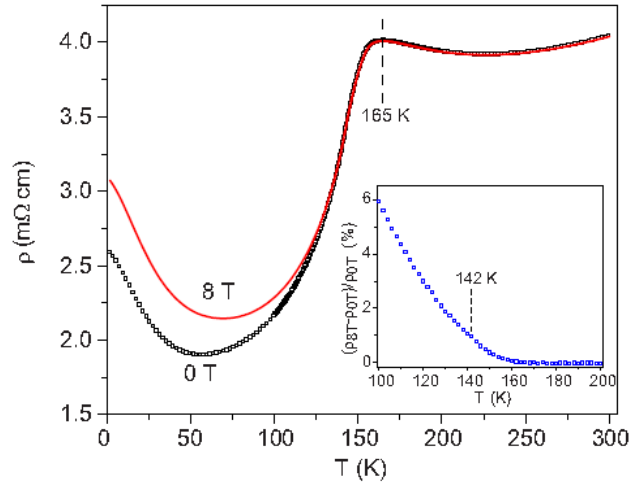


Figure 6.19 The temperature dependence of the electrical resistivity with no applied magnetic field and with an applied field of 8 T. The inset shows the magnetoresistance calculated from the resistivity data<sup>87</sup>.

Hall effect measurements<sup>87</sup> in Figure 6.20 show a corresponding sharp decrease in the apparent carrier concentration ( $n$ ) by an order of magnitude through the transition. This suggests that many of the charge carriers present in the high temperature phase are

localized at  $T_{T-O}$  due to the structural transition. This is likely related to the local moment formation and subsequent magnetic ordering observed below  $T_{T-O}$ . Near room temperature the Hall coefficient is negative and nearly temperature independent, indicating conduction by electrons with an inferred concentration  $n = 3 \times 10^{21} \text{ cm}^{-3}$ .

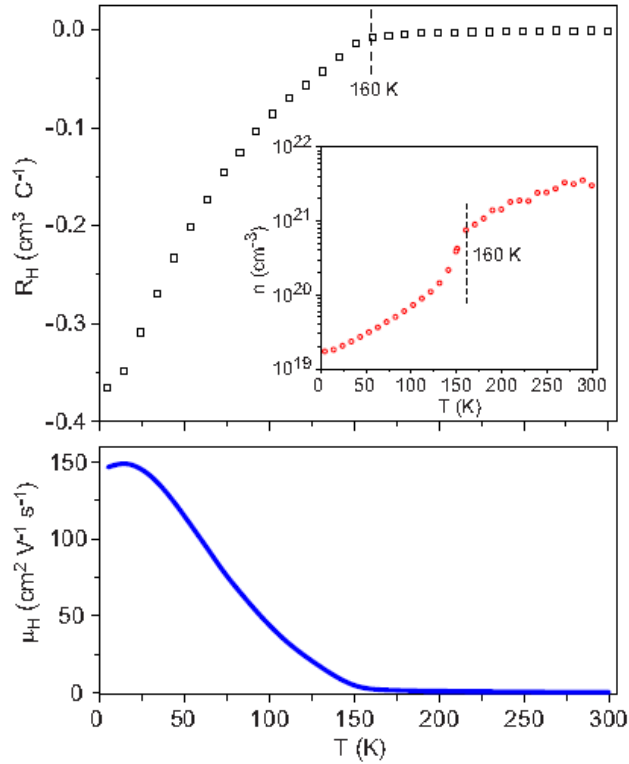


Figure 6.20 Results of Hall-effect measurements on LaFeAsO showing the remarkable decrease in inferred carrier concentration and high mobility at low temperatures is shown in the top panel. The measured Hall coefficient and inferred carrier concentration is shown in the top panel inset. The bottom panel shows the Hall mobility calculated from the carrier concentration<sup>87</sup>.

The Figure 6.21 shows the thermal and thermoelectric transport properties of LaFeAsO. The thermal conductivity increases abruptly below the  $T_{SDW}$ , but otherwise follows the behavior of typical crystalline materials. The increase in thermal conductivity cannot be attributed to the change in electronic thermal conduction as the thermal conductivity in this low carrier concentration material is dominated by phonons. Thus the

observed behavior must be attributed to an increase in the thermal conductivity of the lattice. This could be due to a decrease in electron-phonon scattering below the transition, suggesting that above 150 K the charge carriers which participate in the SDW interact strongly with the phonons. The Seebeck coefficient is negative over the entire temperature range, indicating that electrons dominate the electrical conduction. This is consistent with the negative Hall coefficient<sup>87</sup>.

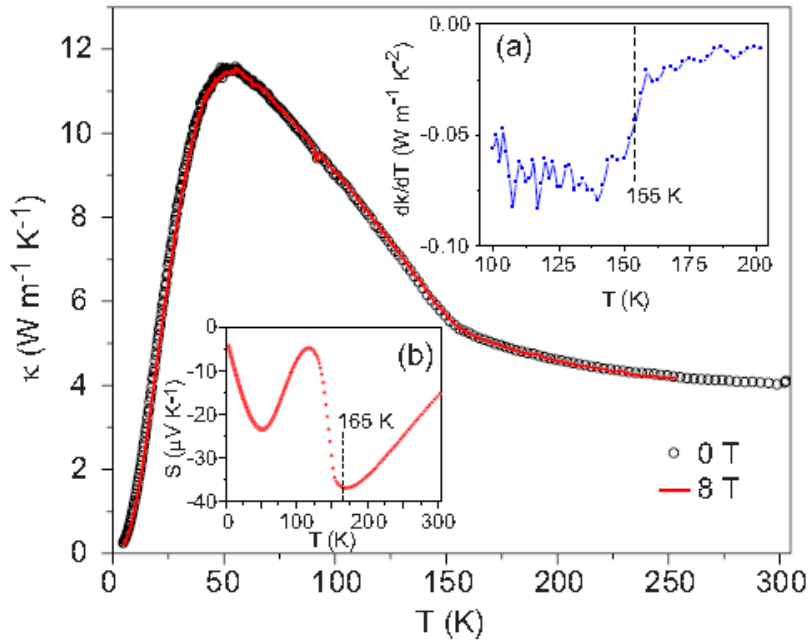


Figure 6.21 Thermal and thermoelectric transport properties of LaFeAsO. The thermal conductivity measured in zero applied magnetic field and in a field of 8 T, shows an abrupt change in slope (inset a) as the structure transforms from tetragonal to orthorhombic upon cooling. Inset (b) shows the dramatic changes in the Seebeck coefficient that occur below the transition temperatures<sup>87</sup>.

Magnetization measurement shows a drop in  $M/H$  through the phase transition region, a signature of the spin density wave formation. The magnetization shows little temperature dependence above and below the transition region. At  $H = 7$  T and  $T = 1.8$  K the measured moment corresponds to only  $9 \times 10^{-3} \mu_B$  per Fe atom<sup>87</sup>. This behavior suggests that some slight canting of the antiferromagnetically ordered moments occurs in

this material. Calculations suggest that a small moment in the z-direction ( $0.06 \mu_B$ ) may exist in the ordered phase<sup>98</sup>. This could support the canted antiferromagnet mode. The magnetic behavior of this material is complex and not yet well characterized or well understood<sup>87</sup>.

After the published results on the 3.18mg LaFeAsO sample, subsequent measurements on LaFeAsO using PPMS were used to do a comparison study on the rare-earth elements PrFeAsO, NdFeAsO and CeFeAsO<sup>16</sup>. Figure 6.22 shows the subsequent results using PPMS on LaFeAsO [123] and our ac calorimetry measurements on the 3.18mg sample. A comparison of the  $\Delta C_p$  results for the LaFeAsO sample using PPMS and ac-calorimetry shows that the size and the shape of the anomaly are comparable.

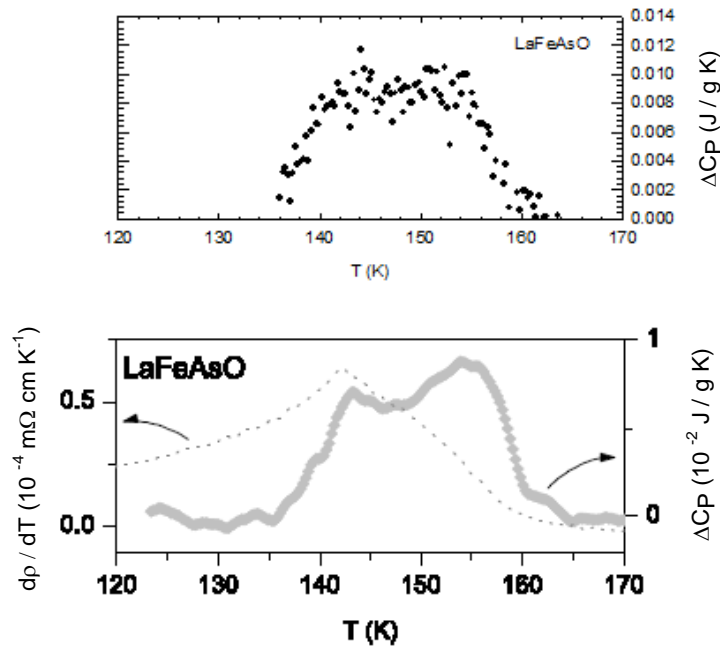


Figure 6.22 A comparison of the  $\Delta C_p$  results for the LaFeAsO sample using ac calorimetry setup in our lab and PPMS results by McGuire et al<sup>16</sup>.

## 6.4 Conclusion

In summary, we measured the specific heat of  $\text{Sr}_4\text{Ru}_3\text{O}_{10}$  crystals along the  $c$  axis at its magnetic transition both in the presence and absence of a field. A comparison of zero

field measurement from our lab with respect to the data from the in-field setup was consistent. The estimated entropy change is an order of magnitude smaller than expected for complete spin ordering, suggesting that either the spin ordering is not spatially uniform or only a small component of the spins order. At an applied field of 0.1 T, the specific heat anomaly disappears. There were no signs of broadening of the specific heat peaks due to the external magnetic field. While the effect of fluctuations is unlikely to be a large effect here, the specific heat anomaly at  $T_C$  suggests a more complex spin ordering.

Our low temperature measurements for the  $c$  axis sample came out noisy for several repeated runs and hence we did not pursue any field measurement for this sample. As for the specific heat measurements along the  $ab$  plane for this crystal, we did not obtain good time constant presumably because the sample had a very small thermal conductivity along this direction and hence did not pursue the specific heat measurements in the presence and absence of a field.

The heat capacity of LaFeAsO was measured using ac-calorimetry in the presence and absence of magnetic field. The structural transition centered at 155 K and the magnetic transition centered at 143 K is observed. The coincidence of these two peaks with the structural and magnetic phase transition temperatures strongly suggest that these are indeed separate anomalies, and not a single transition. The application of magnetic field as high as 11 T did not show any changes in the anomalies consistent with very anisotropically coupled spins as described in Reference [93]. At high temperatures, LaFeAsO is a low carrier concentration metal with conduction dominated by electrons and with no local magnetic moment. This is supported by measurements of electrical resistivity, Hall coefficient and carrier concentration and Seebeck coefficient. Strong electron-phonon coupling exists in the high temperature tetragonal phase, as evidenced by the behavior of the mobility, thermal conductivity and Seebeck coefficient through the phase transition region.

## Chapter 7

### Specific Heat Measurements on other Fe-As based systems

#### 7.1 Introduction

The recent discovery of superconductivity in the rare earth iron based superconductors has generated enormous interest because these materials are the first non-copper-oxide superconductors with  $T_C$ 's up to 55 K. Soon after the discovery of superconductivity in the doped RFeAsO and AFe<sub>2</sub>As<sub>2</sub> families, studies of the undoped materials revealed interesting structural and magnetic properties. All of the parent compounds (RFeAsO, R = La, Ce, Nd, Pr; AFe<sub>2</sub>As<sub>2</sub>, A=Ba, Ca and Sr) of the iron based superconductors investigated so far display a similar antiferromagnetic phase transition accompanying a tetragonal to orthorhombic structural distortion on cooling from 250 K to 100 K<sup>16,17,87,99,100</sup>. At room temperature the RFeAsO family materials adopt the ZrCuSiAs structure type (tetragonal, space group *P4/nmm*) and their structure can be visualized as a stacking of flat square nets of single atom types in the sequence 2O-R-As-2Fe-As-R. The Fe and O nets are rotated 45° with respect to the As and R nets and are twice as dense. The stacking of these layers gives tetrahedral coordination to Fe and O whereas R and As are in square antiprismatic coordination<sup>87</sup>. The AFe<sub>2</sub>As<sub>2</sub> compounds crystallize in the tetragonal ThCr<sub>2</sub>Si<sub>2</sub> type structure at room temperature<sup>101</sup> which consists of alternate stacking of edge sharing Fe<sub>2</sub>As<sub>2</sub> tetrahedral layers and R<sub>2</sub>O<sub>2</sub> tetrahedral layers along the c axis. Superconductivity is induced in the RFeAsO system, by doping with fluorine<sup>102</sup>, cobalt<sup>103</sup>, thorium<sup>104</sup>, strontium<sup>105</sup> and oxygen<sup>106</sup>. In the case of the AFe<sub>2</sub>As<sub>2</sub> system, the compounds become superconductors if appropriately modified by substitutions on the A site by alkali metals<sup>107,108</sup> or direct substitution within the Fe<sub>2</sub>As<sub>2</sub> slab by Co<sup>17, 109,110,111</sup> or Ni<sup>112</sup>.

It would be interesting to examine compounds from these two different families and do a comparative study. In Chapter 6, I discussed the LaFeAsO material in detail. In this chapter, PrFeAsO, a material belonging to the same family as LaFeAsO is studied. Also, SrFe<sub>1.8</sub>Co<sub>0.2</sub>As<sub>2</sub>, a doped system from the AFe<sub>2</sub>As<sub>2</sub> family is perused.

## 7.2 SDW transition in PrFeAsO

### 7.2.1 The physical properties of PrFeAsO

PrFeAsO crystallizes into the ZrCuSiAs structure type at room temperature with space group  $P4/nmm$  and lattice parameters  $a=3.985 \text{ \AA}$ ,  $c = 8.595 \text{ \AA}$ <sup>113</sup>. The lattice and magnetic structure of PrFeAsO is shown in Figure 7.1. The material undergoes a structural distortion near 150 K and the SDW develops below about 140 K<sup>16,95,96</sup>. Upon further cooling the Pr magnetic moments order antiferromagnetically near  $T_N = 14 \text{ K}$  with Pr moments aligned along the  $c$ -axis<sup>95</sup>. When this occurs there is evidence of a reorientation of the Fe moments, suggesting significant interactions between the magnetism in the Pr and the Fe sub lattices<sup>16</sup>. Interplay between Fe and Pr moments have also been proposed based on anomalous low temperature thermal expansion<sup>96</sup>.

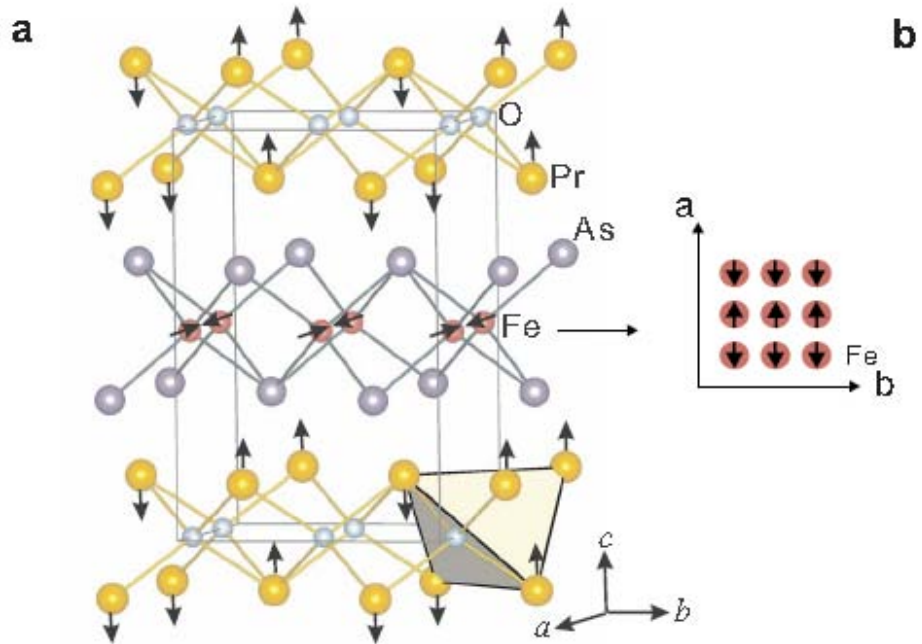


Figure 7.1 Lattice and magnetic structure of PrFeAsO a) The three dimensional antiferromagnetic structures of Fe as determined by neutron diffraction data b) The magnetic structure of Fe in the FeAs plane<sup>95</sup>.

### 7.2.2 Motivation

Having studied the LaFeAsO sample, we wanted to understand the role that the lanthanide played in determining the physical properties of RFeAsO based materials, so we wanted to investigate the specific heat of PrFeAsO at its structural and magnetic transition and do a comparative study with the LaFeAsO compound. A Subsequent measurement on PrFeAsO using a PPMS calorimeter was published recently by McGuire et al<sup>16</sup>. A comparison of our measurements with PPMS results is also included.

### 7.2.3 Sample preparation

The sample was prepared by McGuire at the Oak Ridge National Laboratory. PrFeAsO was made from PrAs, Fe<sub>2</sub>O<sub>3</sub> and Fe powders. Rare-earth arsenides and FeAs starting materials were prepared, similarly to the preparation of LaFeAsO material (discussed in chapter 6) and a detailed description about the preparation of starting materials is published by McGuire et al<sup>87</sup>. Stoichiometric mixtures of the starting materials were ground and mixed thoroughly in a helium-filled glove box, pressed into one half-inch diameter pellets and sealed in silica tubes under about 0.3 atm ultra - high purity argon. The pellets were heated at 1200°C for 30 h. The crystal was characterized using powder x-ray diffraction at the Oak Ridge lab and the results are published<sup>16</sup>.

### 7.2.4 Heat Capacity data

The specific heat measurements were performed on a polycrystalline sample of mass = 12.41mg using the ac-calorimetry setup in our lab. The sample was attached with GE varnish to a flattened, 25 μm diameter type-E thermocouple junction. The chopping frequency used to heat the sample was 2.25 Hz. Since there were not any previous quantitative measurements on this sample, the molar specific heat was approximately normalized to that of LaFeAsO at T = 130 K (i.e. C<sub>p</sub> / R= 8.3556) and correcting for addenda contributions. Hence the normalization of the data should only be considered approximate. However, the atomic mass of La (m = 138.9) and Pr (m = 140.9) are close and the Debye temperatures and specific heats are expected to be similar. The temperature dependence of specific heat, normalized to the gas constant R = 8.314 J mol<sup>-1</sup>



$K^{-1}$  of the PrFeAsO sample is shown in Figure 7.2 (a). Two broad overlapping anomalies were observed one centered at 143 K and the other at 137 K.

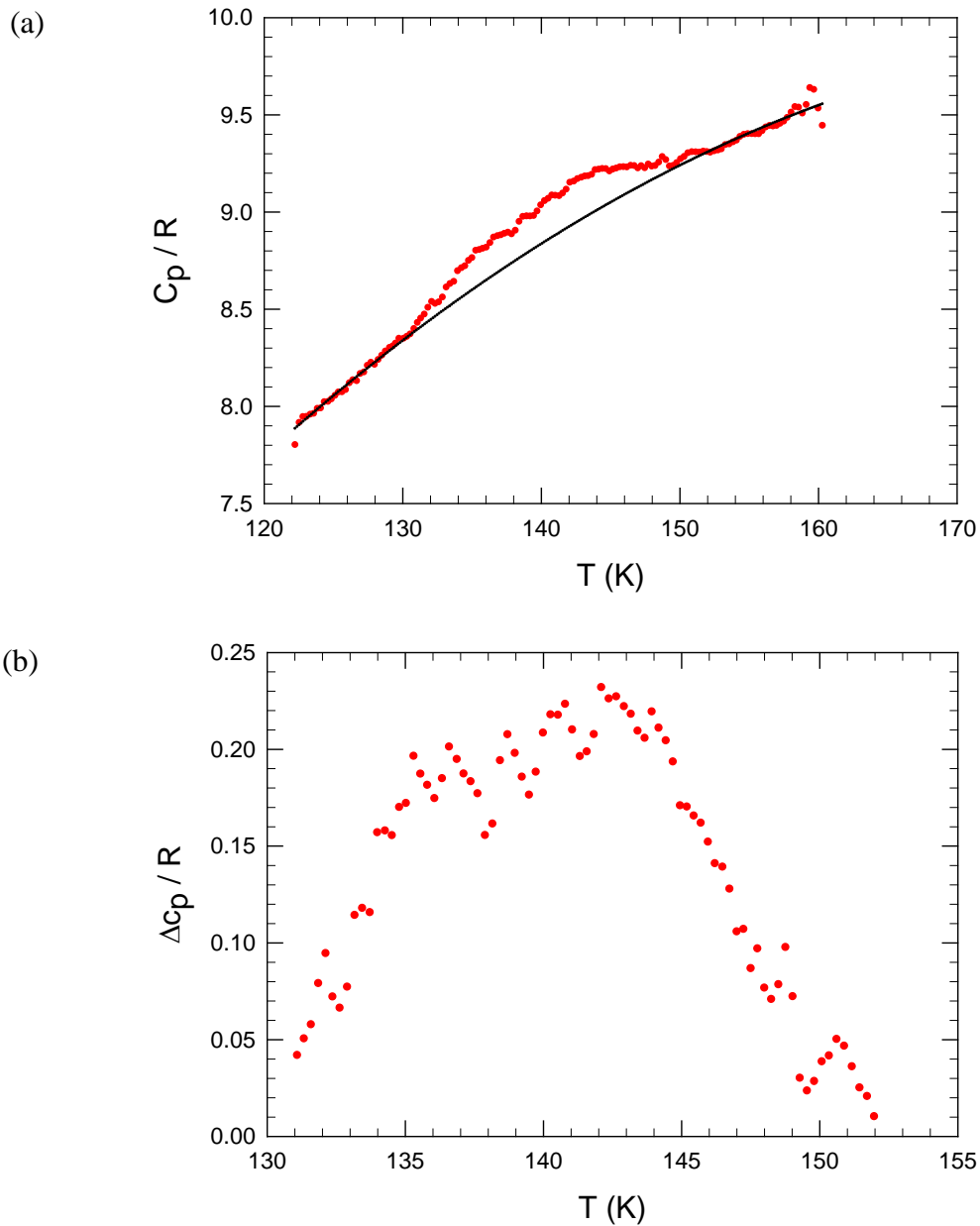


Figure 7.2 (a) The temperature dependence of specific heat normalized to the gas constant  $R = 8.314 \text{ J mol}^{-1}\text{K}^{-1}$  of PrFeAsO sample. The black line shows the background used to estimate the change in entropy. (b) The subtracted data of PrFeAsO show two peaks, one associated with the structural transition centered at 143 K and the other due to the magnetic transition centered at 137 K.

### 7.2.5 Results and Discussion

As shown in Figure 7.2 (a) two broad anomalies are observed. The background was estimated by a polynomial fit to the data above and below the transition region as seen in Figure 7.2 (a). The subtracted data shows two noisy peaks in the Figure 7.2 (b), one associated with the structural transition ( $T_C = 143$  K) and one due to the magnetic transition at  $T = 137$  K.

The lack of thermal hysteresis ( $\Delta T < 0.1$  K) in these measurements suggests that the phase transitions are second order or only weakly first order. The anomalies do not look very mean-field like. A simple estimate of the total entropy change using the baseline shown is  $\Delta S \sim 0.02 R$ . It should be noted that for LaFeAsO, the total entropy obtained was  $0.032R$ . These are very small entropy changes for structural transitions, where roughly one might expect  $\Delta S \sim R$ . For the magnetic transition in PrFeAsO, if we assume mean-field theory with  $0.20R \sim \Delta c_p \sim \Delta\gamma T_c$ , one attains  $\Delta\gamma \sim 12 \text{ mJ mol}^{-1}\text{K}^{-1}$ .

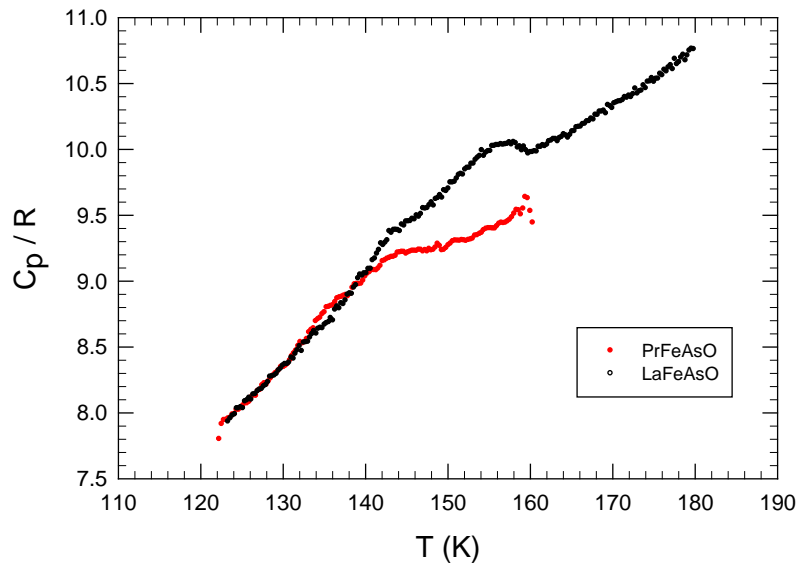


Figure 7.3 The specific heat of LaFeAsO (black curve) and PrFeAsO (red curve) samples over the temperature range 110 K – 190 K in the units of R. PrFeAsO is normalized to LaFeAsO at  $T = 130$  K.

The specific heat measurement of LaFeAsO and PrFeAsO in the temperature range 110K – 190K are shown in Figure 7.3. Taking the cusps in the specific heat as estimates of the transition temperatures, we see that, the magnetic ordering temperature increases from 137 K for PrFeAsO to 143 K for LaFeAsO. The structural transition increases from 143 K for PrFeAsO to 155 K for LaFeAsO.

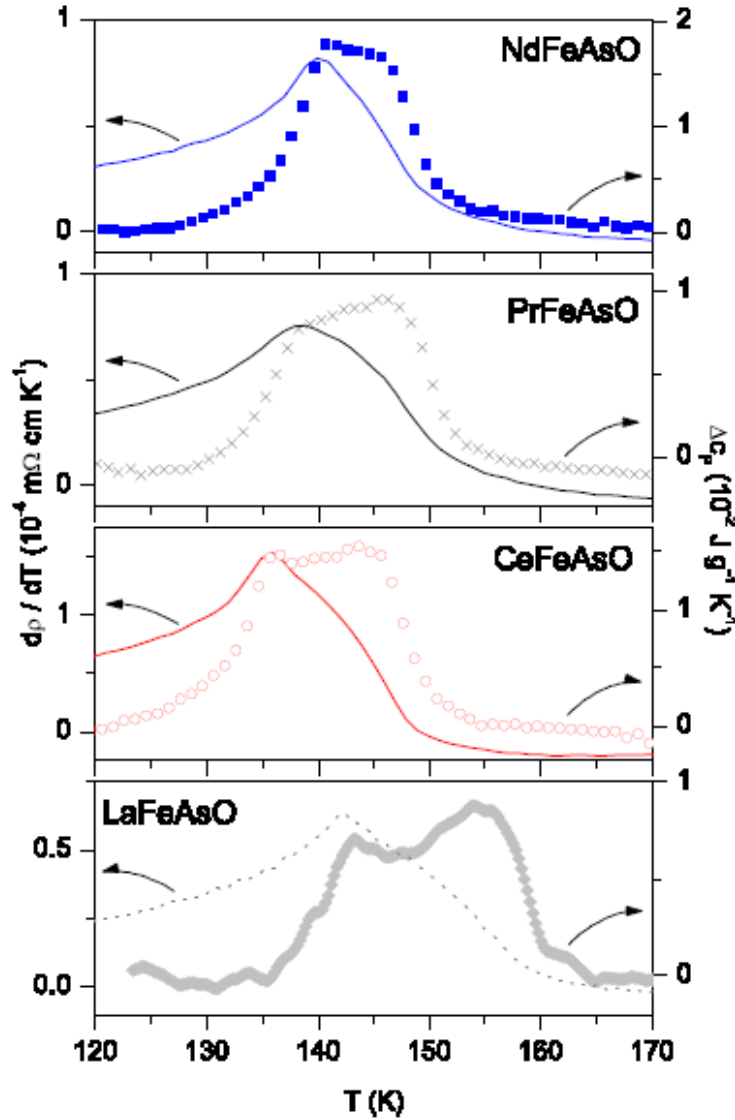


Figure 7.4 The temperature derivative of the resistivity ( $d\rho/dT$ ) and the background subtracted heat capacity ( $\Delta C_p$ ), of the RFeAsO series measured with a PPMS calorimeter<sup>16</sup>.

According to a recent study by McGuire et al<sup>16</sup> on the RFeAsO series, the magnetic ordering temperature increases from 136 K for CeFeAsO to 139 K for PrFeAsO to 141 K for NdFeAsO (as shown in Figure 7.4). The structural transition varies somewhat less strongly across the series from 144 K for CeFeAsO to 146 K for both PrFeAsO and NdFeAsO. The different behavior between materials containing non-magnetic and magnetic rare earth elements suggests that the presence of the magnetic moment on the R site influences the structural distortion and magnetic ordering.

A comparison of our results on PrFeAsO with the subsequent PPMS data by McGuire et al is shown in Figure 7.5. The structural transition temperature and the magnetic ordering temperature observed using PPMS by McGuire et al are slightly higher (~3K) than we measure. This suggests that the results may be sample dependent, but the difference may be instrumental. The size and shape of the anomalies of the PrFeAsO samples are very similar. Since PPMS is suitable for measuring larger size samples, cleaner data was obtained with PPMS than ac-calorimetry. AC-calorimetry is suitable for sub-milligram crystals but for this measurement we used 12.41mg polycrystalline sample, which decreases our ac signal and may be a reason for the noisy data. We did not try to cleave the sample as it was crumbly in nature, and hence we used the large sample provided by McGuire to do our measurements.

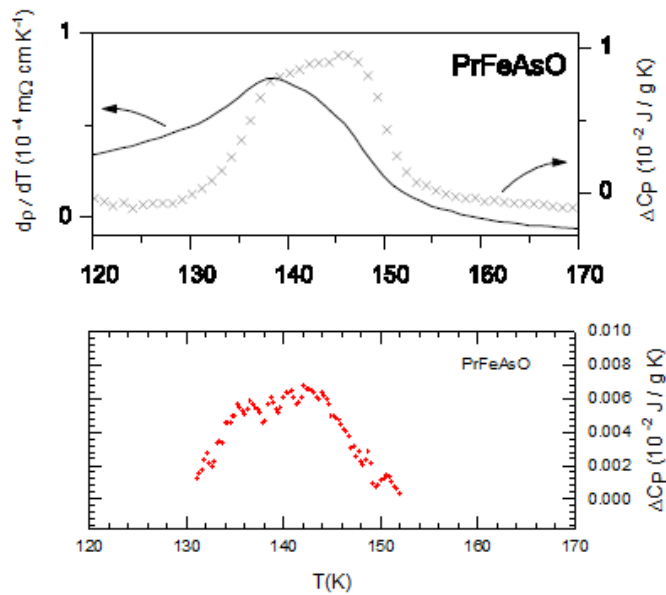


Figure 7.5 A comparison of the  $\Delta C_p$  results for the PrFeAsO sample using ac calorimetry setup in our lab (bottom) and PPMS results by McGuire et al<sup>16</sup> (top)

## 7.3 Superconducting transition in SrFe<sub>1.8</sub>Co<sub>0.2</sub>As<sub>2</sub>

### 7.3.1 The physical properties of SrFe<sub>1.8</sub>Co<sub>0.2</sub>As<sub>2</sub>

Soon after the discovery of superconductivity in doped RFeAsO (R = rare-earth element) materials<sup>14</sup>, investigations also focused on the structurally related AFe<sub>2</sub>As<sub>2</sub> compounds (A=alkaline, alkaline-earth or rare-earth metal). While pure SrFe<sub>2</sub>As<sub>2</sub><sup>114</sup> undergoes a lattice distortion and antiferromagnetic (AFM) ordering at T<sub>o</sub>= 205 K, a small amount of Co substitution leads to a rapid decrease of T<sub>o</sub>, followed by the onset of bulk superconductivity in the concentration range 0.2 ≤ x ≤ 0.4 with a maximum T<sub>c</sub> ≈ 20K<sup>17</sup>. SrFe<sub>1.8</sub>Co<sub>0.2</sub>As<sub>2</sub> belongs to BaAl<sub>4</sub>-type structure<sup>115</sup>, space group *I4/mmm*, and lattice constants  $a = 3.9278(2) \text{ \AA}$ ,  $c = 12.3026(2) \text{ \AA}$ <sup>17</sup>.

### 7.3.2 Motivation

The motivation of this specific heat measurement was to study the crystal in the absence and presence and of a field and examine the superconducting transition.

### 7.3.3 Heat Capacity data

The sample used in this work was prepared by McGuire from Oak Ridge Laboratory. In this work, we use the ac-calorimetry setup in our lab and the in-field magnetic setup to examine the specific heat at low temperature (4 K ≤ T ≤ 20 K). The specific heat measurements were first performed using the ac-calorimetry setup in our lab. Measurements were made on a single crystal of mass 0.62 mg. The sample was attached to a Cernox sensor with 9.7 μg of GE varnish. The chopping frequency used was 16.6 Hz. Absolute values of the total heat capacity were obtained using the results of Leithe-Jasper et al<sup>17</sup> at T = 8 K and C<sub>p</sub> = 0.4096 J /mol K. It should be noted that the normalization to PPMS results is only approximate; it gives a specific heat that is 90% of the Dulong-Petit value near room temperature. We also assume that the actual compositions of our sample and the Leithe-Jasper sample are at their nominal values and therefore similar. After doing measurements using our old header, the sample holder was transferred to the new header and measurements were performed in the in-field setup in the temperature range (4 K ≤ T ≤ 20 K). Figure 7.6 shows a plot of C<sub>p</sub>/T vs T<sup>2</sup> for this sample on the old and new headers. The low temperature data (4 K < T < 8 K) in the new

header (black and blue dataset) differ from the old header (red data) results by ~10%, reflecting the uncertainty in the sample time constants at these temperatures.

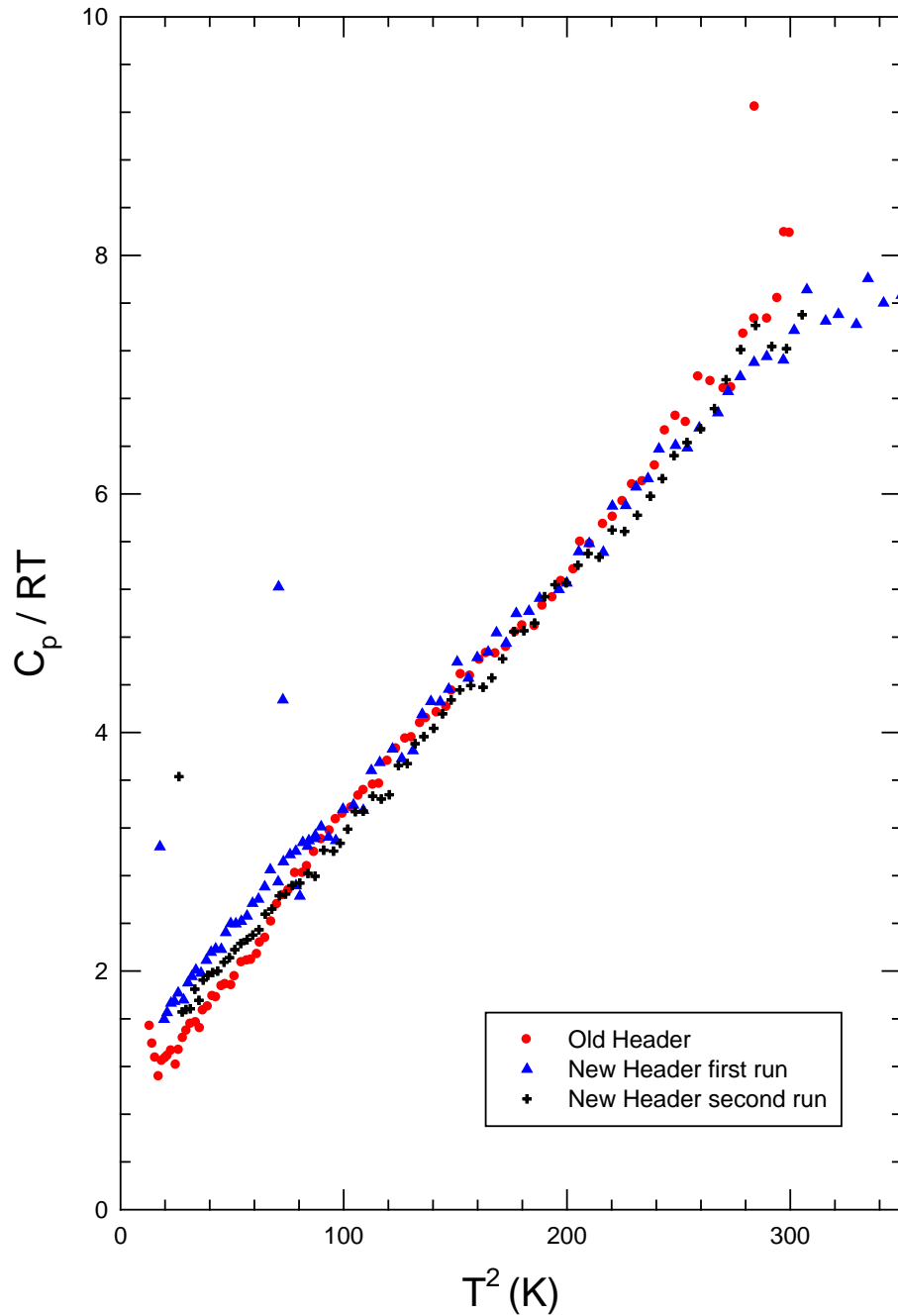


Figure 7.6 A plot of  $C_p/T$  vs  $T^2$  using the old and new header for the 0.62 mg sample. (Inset) The specific heat measured using our old header and new header over the temperature range 4 K to 18 K, in the units of R, ( $R = 8.31$  J/ mol K).

### 7.3.4 Results and Discussion

According to McGuire, the superconducting transition observed for this crystal was at  $T \sim 13$  K, and it is the nature of these single crystals to show a broad/small anomaly<sup>116</sup>. The measurements using our old header shown in Figure 7.7 showed a gradual bump near the proposed transition temperature. Though it is expected for these materials to show a broad/small anomaly, it was difficult to distinguish the anomaly out of the noise from our measurements. We did several runs using our old header; they all had a similar bump and were noisy.

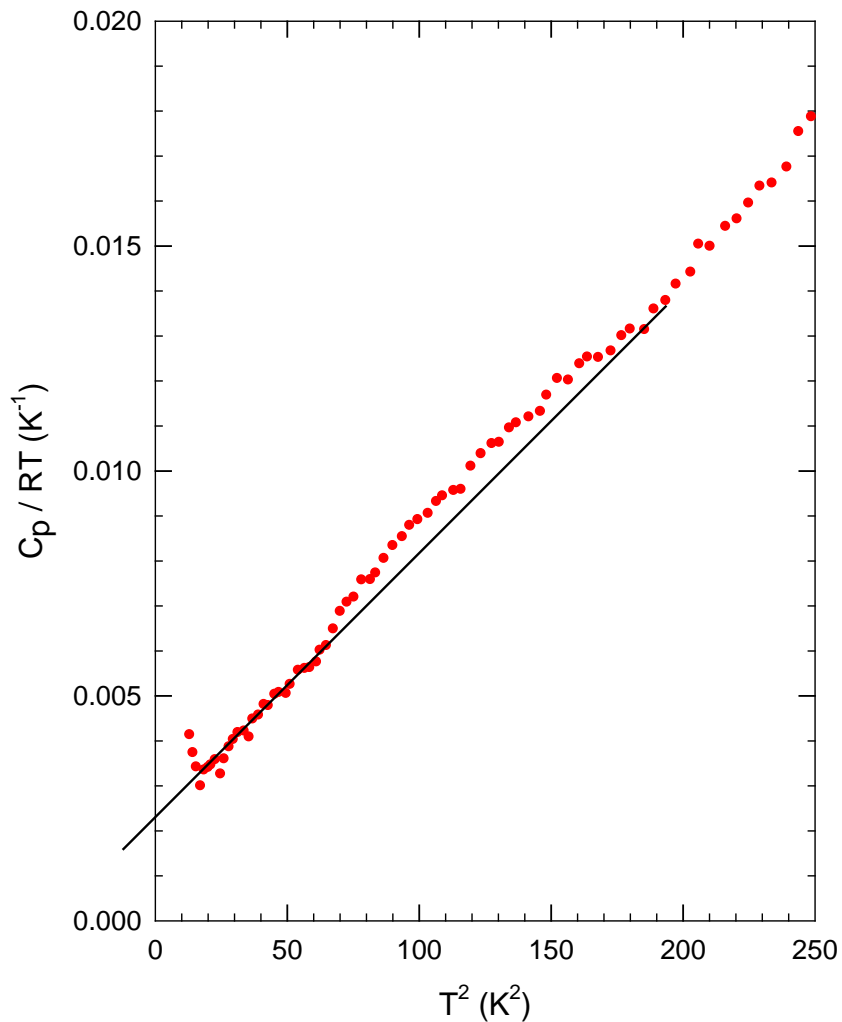


Figure 7.7 The low temperature specific heat, plotted as  $C_p/RT$  vs.  $T^2$  for the  $SrFe_{1.8}Co_{0.2}As_2$  sample. The intercept of the solid black line gives the  $\gamma$ .

A fit of our low temperature result to  $C_p = \gamma T + \beta T^3$  for  $3 \text{ K} < T < 20 \text{ K}$  (as shown in Figure 7.7) gives values of  $\gamma/R \sim 0.002 / \text{K}$  and  $\beta/R \sim 6.67 \times 10^{-5} / \text{K}^3$  corresponding to a Debye temperature of  $\Theta = 260 \text{ K}$ . The results obtained are within 10% of the results of Leithe-Jasper et.al<sup>17</sup>. The value of  $\gamma$  should be zero in the superconducting state, however, various groups have claimed a non-zero  $\gamma$  term<sup>117,118,119</sup>. Leithe-Jasper et.al<sup>17</sup> obtained a non-zero  $\gamma$  term for this material and our result agrees with their published value. It is argued that the residual  $\gamma$  may be induced by defects<sup>120</sup> or because of an intrinsic contribution due to ungapped parts of the Fermi surface<sup>121</sup> and needs to be elucidated by further experiments.

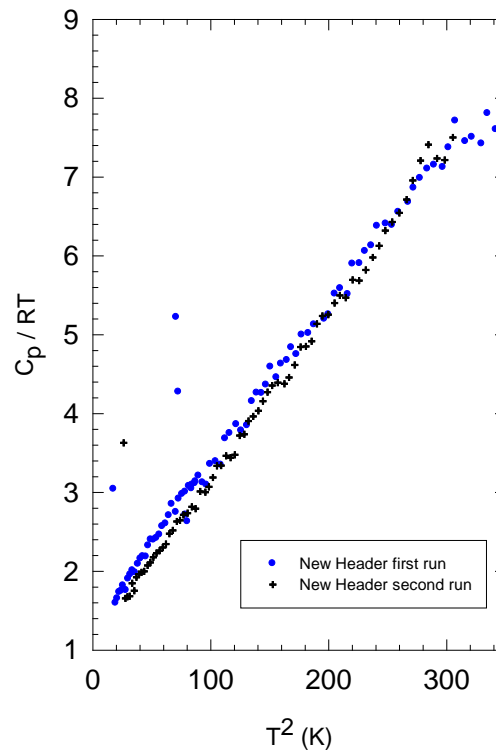


Figure 7.8 A plot of  $C_p/T$  vs  $T^2$  using new header. The blue and black data are measurements using our new header for two different runs.

Figure 7.8 shows a plot of  $C_p/RT$  vs  $T^2$  using the new header. The blue and black data shown are measurements using our new header for two different runs. No obvious specific heat anomaly was observed using our new header as shown in Figure 7.8, i.e. we



could not reproduce the bump as seen using the ac-calorimetry set up in our lab. The possible reasons for not seeing the anomaly/bump in the new header could be because either the sample properties changed when they were exposed to air during moving or there is no anomaly. Since it is unlikely for the sample property to have changed, we conclude that there is no anomaly at the proposed transition temperature and the broad peak noticed in our measurement using our old header was really noise. Since the data using our new header did not show any anomaly near the proposed superconducting transition ( $T \sim 13$  K) we did not pursue our field measurements.

#### **7.4 Conclusion**

Our systematic investigation into the effects of the structural and magnetic phase transitions in PrFeAsO and LaFeAsO revealed that the transition temperatures of PrFeAsO are significantly lower than those in LaFeAsO suggesting a strong influence of the rare-earth magnetic moment on the behavior of the FeAs layers<sup>16</sup>. However, the total entropy estimated was small for both the compounds. The different behavior between these rare earth elements suggests that the presence of the magnetic moment on the R site influences the structural distortion and magnetic ordering. To date, no real consensus has been reached among theorists concerning the electronic nature of these complex materials and their phase transitions. This is especially true concerning the Fe magnetism in the orthorhombic phase.

As for the SrFe<sub>1.8</sub>Co<sub>0.2</sub>As<sub>2</sub> crystal, the specific heat measurements using our old header showed a gradual bump near the proposed superconducting transition at  $T \sim 13$  K whereas measurements using our new header did not show any anomaly. We conclude that our data became noisy near the transition temperature when using our old header and there was no anomaly at the proposed transition temperature. We obtained  $\gamma$ ,  $\beta$  and the Debye temperature  $\Theta$  by fitting our low temperature data. The results obtained were consistent with the published data by Leithe-Jasper et al.

## Chapter 8

### Concluding Remarks

In my thesis, I have focused on the specific heat properties of strongly correlated electron systems in the absence and presence of magnetic field. In this broad category of strongly correlated electron systems, I have studied materials from different families starting with the  $\text{Ca}_{1-x}\text{Sr}_x\text{Ru}_3\text{O}_7$  and  $\text{Sr}_4\text{Ru}_3\text{O}_{10}$  crystals from the Ruddlesden Popper series,  $\text{Fe}_2\text{OBO}_3$  from the oxyborate family,  $\text{LaFeAsO}$ ,  $\text{PrFeAsO}$  and  $\text{SrFe}_{1.8}\text{Co}_{0.2}\text{As}_2$  from the pnictide family. The crystals from these families show different properties ranging from antiferromagnetism, charge ordering, spin density wave and ferromagnetism to name a few. The materials studied were categorized in terms of specific heat properties in the absence of magnetic field and in the presence of magnetic field. In order to study the specific heat of the materials in the presence of a magnetic field, we designed and built a new probe that could fit in a liquid helium Dewar with a 14 T magnet. Most of my work was involved in the design and construction of the probe for specific heat measurements in the magnetic field. Though it was a challenge to work with a small area, we succeeded in building the probe and make it operate for heat capacity measurements in the presence of a field. Using the new probe, we measured the specific heat of  $\text{Sr}_4\text{Ru}_3\text{O}_{10}$  and  $\text{LaFeAsO}$  samples.

The specific heat measurements on  $(\text{Ca}_{1-x}\text{Sr}_x)_3\text{Ru}_2\text{O}_7$  crystals using ac-calorimetry technique were measured in our lab, using our old header in the absence of magnetic field.  $\text{Ca}_3\text{Ru}_2\text{O}_7$  crystal showed a large peak in the effective specific heat at  $T_c = 48$  K structural transition which was independent of measurement/times/frequencies suggesting a latent heat  $L \sim 0.31 R$ , which decreases rapidly in magnitude with Sr substitution. In addition we have quantitatively measured the mean-field like step at  $T_N$  for the first time. The Neel anomaly observed at  $T_N \sim 56$  K is roughly mean-field in shape, but its magnitude ( $\Delta C_p \sim R$ ) was too large for a conventional itinerant electron spin-density-wave transition and too small to be associated with the complete spin-ordering of localized electrons. The magnitude of the anomaly decreases more slowly as Sr substitution decreases the spin order.

For  $\text{Fe}_2\text{OBO}_3$ , a member of the oxyborate family, the transition at 155 K was mean field like with  $\Delta C_p \sim R$ . The structural transition observed at 340K indicates the onset of charge order. The anomaly was slightly hysteretic indicating a weakly first order transition, so that we may be missing latent heat associated with the transition. We did not observe any anomaly at 280(310 K) using our ac-calorimetry technique since our technique is sensitive only to reversible heat flow. Superstructure reflections in  $\text{Fe}_2\text{OBO}_3$  arise from diagonal CO with two domains and Fe valence states very close to integer, suggesting that  $\text{Fe}_2\text{OBO}_3$  is an ideal example for ionic CO.

The specific heat of  $\text{Sr}_4\text{Ru}_3\text{O}_{10}$  crystals along the  $c$  axis at its magnetic transition were measured using our old header and new header. A comparison of zero field measurement from our lab with respect to the data from the in-field setup was consistent. The estimated entropy change is an order of magnitude smaller than expected for complete spin ordering, suggesting that either the spin ordering is not spatially uniform or only a small component of the spins order. At an applied field of 0.1 T, the specific heat anomaly disappears. There were no signs of broadening of the specific heat peaks due to the external magnetic field. The original motivation was to to examine  $\text{Sr}_4\text{Ru}_3\text{O}_{10}$  with our newly built header for B //  $c$  axis and B //  $ab$  plane 1) at its magnetic transition  $T_C$  (~102 K) and 2) at low temperature (2 K – 20 K). We succeeded in measuring the specific heat of  $\text{Sr}_4\text{Ru}_3\text{O}_{10}$  for B// $c$  axis at its magnetic transition but our low temperature measurements for the  $c$  axis sample came out noisy for several repeated runs and hence we did not pursue any field measurement for this sample. As for the specific heat measurements along the  $ab$  plane for this crystal, we did not obtain good time constant presumably because the sample had a very small thermal conductivity along this direction and hence did not pursue the specific heat measurements in the presence and absence of a field.

Following the measurements of  $\text{Sr}_4\text{Ru}_3\text{O}_{10}$ , we measured the specific heat of  $\text{LaFeAsO}$  using our new header. For  $\text{LaFeAsO}$ , the structural transition at 155 K and the magnetic transition at 143 K was observed. The coincidence of these two peaks with the structural and magnetic phase transition temperatures strongly suggest that these are indeed separate anomalies, and not a single transition. The application of magnetic field as high as 11 T did not show any changes in the anomalies. Theoretical analysis predicts

that a nematic order persists above the magnetic ordering temperature. At high temperatures LaFeAsO is a low carrier concentration metal with conduction dominated by electrons and with no local magnetic moment. This is supported by measurements of electrical resistivity, Hall coefficient and carrier concentration and Seebeck coefficient. Strong electron-phonon coupling exists in the high temperature tetragonal phase, as evidenced by the behavior of the mobility, thermal conductivity and Seebeck coefficient through the phase transition region.

Having studied the LaFeAsO sample, we wanted to understand the role that the lanthanide played in determining the physical properties of RFeAsO based materials, so we investigated the specific heat of PrFeAsO at its structural and magnetic transition. The structural and magnetic phase transitions in PrFeAsO and LaFeAsO revealed that the transition temperatures of PrFeAsO are significantly lower than those in LaFeAsO suggesting a strong influence of the rare-earth magnetic moment on the behavior of the FeAs layers. The total entropy estimated was small for both the compounds. The different behavior between these rare earth elements suggests that the presence of the magnetic moment on the R site influences the structural distortion and magnetic ordering. To date, theorists are exploring concerning the electronic nature of these complex materials and their phase transitions.

The specific heat measurements on the  $\text{SrFe}_{1.8}\text{Co}_{0.2}\text{As}_2$  crystal using the setup in our lab showed a gradual bump near the proposed superconducting transition at  $T \sim 13\text{K}$  but the measurements using our in-field setup did not show any anomaly. We conclude that our data became noisy near the transition temperature when using our old header and there was no anomaly at the proposed transition temperature.

## References

- <sup>1</sup> U Mizutani, Introduction to the electron theory of metals, Cambridge University Press, UK, 2001
- <sup>2</sup> M Chung, E Figueroa, Y K Kuo, Y Wang, J W Brill, T Burgin, L K Montgomery, Phys. Rev. B, **48**, 9256 (1993)
- <sup>3</sup> X N Lin, V A Bondarenko, G Cao, J W Brill, Solid State Communication, **130**, 151 (2004)
- <sup>4</sup> J W Brill, M Chung, Y K Kuo, X Zhan, E Figueroa, G Mozurkewich, Phys. Rev. Lett., **74**, 1182 (1995)
- <sup>5</sup> M Crawford, R L Harlow, W Marshall, Z Li, G Cao, R L Lindstrom, Q Huang and J W Lynn, Phys. Rev. B, **65**, 214412 (2002)
- <sup>6</sup> S McCall, G Cao, J E Crow, Phys. Rev. B, **67**, 094427 (2003)
- <sup>7</sup> Y Yoshida, I Nagai, S I Ikeda, N Shirakawa, M Kosaka, N Mori, Phys. Rev. B, **69**, 220411 (2004)
- <sup>8</sup> J C Lashley, M F Hundley, A Migliori, J L Sarrao, P G Pagliuso, T W Darling, M Jaime, J C Cooley, W L Hults, L Morales, D J Thoma, J L Smith, J Boerio-Goates, B F Woodfield, G R Steward, R A Fisher, N E Philips, Cryogenics, **43**, 369 (2003)
- <sup>9</sup> Stephen Blundell, Magnetism in Condensed Matter, Oxford University Press, 2004
- <sup>10</sup> J P Attfield, A M T Bell, L M Rodriguez-Martinez, J M Greneche, R J Cernik, J F Clarke, D A Perkins, Nature (London), **396**, 655 (1998)
- <sup>11</sup> G Cao, L Balicas, W H Song, Y P Song, Y P Sun, Y Xin, V A Bondarenko, J W Brill, S Parkin, X N Lin, Phys. Rev. B, **68**, 174409 (2003)
- <sup>12</sup> G Cao, S Chikara and J W Brill, Phys. Rev. B, **75**, 024429 (2007)
- <sup>13</sup> G Cao, S K McCall and J E Crow, Phys. Rev. B, **56**, 10 (1997)
- <sup>14</sup> Y Kamihara, T Watanabe, M Hirano and H Hosono, J. Am. Chem. Soc., **130**, 3296 (2008)
- <sup>15</sup> J Dong et al., Europhys. Lett, **83**, 27006 (2008)
- <sup>16</sup> M A McGuire, R P Hermann, A S Sefat, B C Sales, R Jin, D Mandrus, F Grandjean, G J Long, New J. Phys., **11**, 025011 (2009)

- <sup>17</sup> A Leithe-Jasper, W Schnelle, C Geibel and H Rosner, Phys. Rev. Lett., **101**, 207004 (2008)
- <sup>18</sup> M W Zemansky, Heat and Thermodynamics, McGraw-Hill, NewYork, 1957
- <sup>19</sup> C Kittel, Thermal Physics, John Wiley and Sons Inc., NewYork, 1969
- <sup>20</sup> J L Ginzburg and L D Landau, Zh. Eksp. Teor. Fiz., **20**, 1064 (1950)
- <sup>21</sup> J Bardeen, L N Cooper and J R Schrieffer, Phys. Rev. B, **108**, 1175 (1957)
- <sup>22</sup> J Samuel Smart, Effective Field theories of Magnetism, W B Saunders Company, Philadelphia & London, 1966
- <sup>23</sup> R L Carlin & A J VanDuyneveldt, Magnetic Properties of Transition Metal Compounds, Springer-Verlag NewYork Inc., NewYork 1977
- <sup>24</sup> V Durairaj, Ph.D Thesis (unpublished), 2008
- <sup>25</sup> E C Stoner, Proc. R. Soc. Lond. A, **169**, 339 (1939)
- <sup>26</sup> A W Overhauser, Phys. Rev. B, **3**, 128 (1962)
- <sup>27</sup> Patrik Fazekas, Lecture Notes on Correlation and Magnetism, World Scientific Publishing Co. Pte. Ltd, 1999
- <sup>28</sup> N Matsunaga, K Yamashita, H Kotani and K Nomura, Phys. Rev. B, **64**, 052405 (2001)
- <sup>29</sup> G Montambaux, Phys. Rev. B, **38**, 4788 (1988)
- <sup>30</sup> N Ashcroft and N D Mermin, Solid State Physics, Holt, Rinehart and Winston, Philadelphia 1976
- <sup>31</sup> A Tari, The Specific Heat of Matter at Low Temperatures, Imperial College Press, London, 2003
- <sup>32</sup> H J Goldsmid, Problems in Solid State Physics, Academic Press Inc., NewYork, 1968
- <sup>33</sup> S K Ma, Modern Theory of Critical Phenomena, Benjamin/Cummings, Reading, Massachusetts, 1976

- <sup>34</sup> H E Stanley, Introduction to Phase Transitions and Critical Phenomena, Oxford University Press, New York, 1971
- <sup>35</sup> R A Craven and S F Meyer, Phys. Rev. B, **16**, 4583 (1977)
- <sup>36</sup> R S Kwok and S E Brown, Phys. Rev. Lett., **63**, 895 (1989); R S Kwok, G Gruner and S E Brown, Phys. Rev. Lett., **65**, 365 (1990)
- <sup>37</sup> W L McMillan, Phys. Rev. B, **16**, 643 (1977)
- <sup>38</sup> Y Wang, M Chung, T N O'Neal and J W Brill, Synth. Met., **46**, 307 (1992)
- <sup>39</sup> P A Lee, T M Rice, P W Anderson, Phys. Rev. Lett., **31**, 462 (1973)
- <sup>40</sup> M Chung, E Figueroa, Y K Kuo, Y Wang, J W Brill, T Burgin, L K Montgomery, Phys. Rev. B, **48**, 9256 (1993)
- <sup>41</sup> M Chung, Ph.D Thesis (unpublished), University of Kentucky (1993)
- <sup>42</sup> L Hatta and A J Ikushima, Jpn. J. App. Phys., **20**, 1995 (1981)
- <sup>43</sup> M B Salamon, Phys. Rev. B, **2**, 214 (1970)
- <sup>44</sup> P R Garnier, Ph.D Thesis (unpublished), University of Illinois, (1972)
- <sup>45</sup> J D Baloga and C W Garland, Rev. Sci. Instrum , **48**, 105 (1977)
- <sup>46</sup> P R Garnier, M B Salomon, Phys. Rev. Lett., **27**, 1523 (1971)
- <sup>47</sup> <http://www.precisioncryo.com/dewarvapo.html>
- <sup>48</sup> <http://www.oxford-instruments.com/products/low-temperature/Superconducting-magnets/solenoid-magnets/Pages/Standard-solenoid-magnets.aspx>
- <sup>49</sup> Variable Temperature Insert Operating Manual – Oxford Instruments
- <sup>50</sup> <http://spectroscopy.web.psi.ch/rita2/htdocs/auxequip/magnet/9teslamanbig.htm#>
- <sup>51</sup> <http://www.lakeshore.com/temp/sen/spack.htm>
- <sup>52</sup> J W Ekin, Experimental techniques for low temperature measurements, Oxford University Press
- <sup>53</sup> Y Kuo, Ph.D Thesis (unpublished), University of Kentucky (1995)

- <sup>54</sup> G Cao, K Abboud, S McCall, J E Crow, R P Guertin, Phys. Rev. B, **62**, 998 (2000)
- <sup>55</sup> G Cao, L Balicas, Y Xin, J E Crow et al., Physica B, **246**, 144 (1998)
- <sup>56</sup> Y V Sushko, B DeHarak, G Cao, G Shaw, D K Powell, J W Brill, Solid State Communication, **56**, 5387 (1997)
- <sup>57</sup> S I Ikeda, Y Maeno, S Nakatsuji, M Kosaka, Y Uwatoko, Phys. Rev. B, **62**, R6089 (2000)
- <sup>58</sup> D J Singh, S Auluck, Phys. Rev. Lett., **96**, 097203 (2006)
- <sup>59</sup> G Cao, S McCall, J E Crow, R P Guertin, Phys. Rev. Lett., **78**, 1751 (1997)
- <sup>60</sup> X N Lin, Z X Zhou, V Durairaj, P Schlottmann, G Cao, Phys. Rev. Lett., **95**, 017203 (2005)
- <sup>61</sup> Y Yoshida, S I Ikeda, H Matsuhata, N Shirakawa, C H Lee, S Katano, Phys. Rev. B, **72**, 054412 (2005)
- <sup>62</sup> F Baumberger, N J C Ingle, N Kikugawa, M A Hossain, W Meevasana, R S Perry, K M Shen, D H Lu, A Damascelli, A Rost, A P Mackenzie, Z Hussain, Z X Shen, Phys. Rev. Lett., **96**, 107601 (2006)
- <sup>63</sup> E Ohmichi, Y Yoshida, S I Ikeda, N Shirakawa, T Osada, Phys. Rev B, **70**, 104414 (2004)
- <sup>64</sup> J W Brill, M Chung, Y K Kuo, X Zhan, E Figueroa, G Mozurkewich, Phys. Rev. Lett., **74**, 1182 (1995)
- <sup>65</sup> G Cao, S C McCall, J E Crow, R P Guertin, Phys. Rev. B, **56**, 5387 (1997)
- <sup>66</sup> G Cao, C S Alexander, S McCall, J E Crow, R P Guertin, Mat. Sci. Eng. B, **63**, 76 (1999)
- <sup>67</sup> V Varadarajan, S Chikara, V Durairaj, X N Lin, G Cao, J W Brill, Solid State Communication, **141**, 402 (2007)
- <sup>68</sup> J Coroneus, B Alavi, S E Brown, Phys. Rev. Lett., **70**, 2332 (1993)
- <sup>69</sup> D K Powell, K P Starkey, G Shaw, Y V Sushko, L K Montgomery, J W Brill, Solid State Communication, **119**, 637 (2001)



- <sup>70</sup> M A Continentino, A M Pedreira, R B Guimaraes, M Mir, J C Fernandes, Phys. Rev. B, **64**, 014406 (2001)
- <sup>71</sup> M Angst, Charge and magnetic order of Fe<sub>2</sub>OBO<sub>3</sub> crystals (unpublished)
- <sup>72</sup> J Garcia and G Subias, Phys. Rev. B, **74**, 176401 (2006); I Leonov et al., ibid. **74**, 176402 (2006)
- <sup>73</sup> A D Balaev et al., J. Exp. Theor. Phys., **97**, 989 (2003)
- <sup>74</sup> M Angst, P Khalifah, R P Hermann, H J Xiang, M H Whangbo, V Varadarajan, J W Brill, B C Sales and D Mandrus, Phys. Rev. Lett., **99**, 086403 (2007)
- <sup>75</sup> A Payzant (unpublished document)
- <sup>76</sup> M Angst, R P Hermann, W Schweika, J W Kim, P Khalifah, H J Xiang, M H Whangbo, D H Kim, B C Sales and D Mandrus, Phys. Rev. Lett., **99**, 256402 (2007)
- <sup>77</sup> R P Hermann et al., Phys. Rev. B, **70**, 214425 (2004)
- <sup>78</sup> A P Douvalis et al., J. Phys. Condes. Matter, **12**, 177 (2000)
- <sup>79</sup> A T Paxton and H M Polatoglou, Phys. Rev. Lett., **78**, 270 (1997)
- <sup>80</sup> I. D. Brown and D. Altermatt, Acta Cryst. B 41, (1985) 244; N. E. Brese et al, ibid. **47**, 192,1991
- <sup>81</sup> P M Woodward and P Karen, Inorg. Chem, **42**, 1121 (2003)
- <sup>82</sup> F Menil, J. Phys. Chem. Solids, **46**, 763 (1985)
- <sup>83</sup> B Gupta, M Kim, H Bharath, S L Cooper and G Cao, Phys. Rev. Lett., **96**, 067004 (2006)
- <sup>84</sup> S Chikara, V Durairaj, W H Song, Y P Sun, X N Lin, A Douglass, G Cao and P Schlottmann, Phys. Rev. B, **73**, 224420 (2006)
- <sup>85</sup> J Rodriguez-Carvajal, Full Prof Suite 2005, Version 3.30, June 2005, ILL
- <sup>86</sup> [www.phys.psu.edu/~liu/EM\\_alex.htm](http://www.phys.psu.edu/~liu/EM_alex.htm)
- <sup>87</sup> A J Millis, A J Schofield, G G Lonzarich, S A Grigera, Phys. Rev. Lett., **88**, 217204 (2002)

- <sup>88</sup> T Nomura, S W Kim, Y Kamihara, M Hirano, P V Sushko, K Kato, M Takata, A L Shluger and H Hosono, *Supercond. Sci. Tech.*, **21**, 125028 (2008)
- <sup>89</sup> L Boeri, O V Dolgov and A A Golubov, *Phys. Rev. Lett.*, **101**, 026403 (2008)
- <sup>90</sup> C Cruz, Q Huang, J W Lynn, J Li, W Ratcliff II, J L Zarestky, H A Mook, G F Chen, J L Luo, N L Wang, P Dai, *Nature*, **453**, 07057 (2008)
- <sup>91</sup> M A McGuire et al., *Phys. Rev. B*, **78**, 094517 (2008)
- <sup>92</sup> H H Klauss et al., *Phys. Rev. Lett.*, **101**, 077005 (2008)
- <sup>93</sup> J Wu, P Phillips and A H Castro Neto, *Phys. Rev. Lett.*, **101**, 126401 (2008)
- <sup>94</sup> M A McGuire (unpublished document)
- <sup>95</sup> B H Toby, *J. Appl. Cryst.*, **34**, 210 (2001)
- <sup>96</sup> A C Larson and R B V Dreele, General Structural Analysis System (GSAS), Los Alamos National Laboratory Report LAUR (2004) 86-748
- <sup>97</sup> C Fang, H Yao, W Tsai, J Hu and S A Kivelson, *Phys. Rev. B*, **77**, 224509 (2008)
- <sup>98</sup> J Wu, P Philips and A H Castro Neto, cond-mat/0805.2167
- <sup>99</sup> J Zhao, Q Huang, C Dela Cruz, J W Lynn, M D Lumsden, Z A Ren, J Yang, X Shen, X Dong, Z Zhao, P Dai, *Phys. Rev. B*, **78**, 132504 (2008)
- <sup>100</sup> S A J Kimber, D N Argyriou, F Yokaichiya, K Habicht, S Gerischer, T Hansen, T Chatterji, R Klingeler, C Hess, G Behr, A Kondrat, B Buechner, *Phys. Rev. B*, **78**, 140503(R) (2008)
- <sup>101</sup> D Kasinathan, A Ormeci, K Koch, U Burkhardt, W Schnelle, A Leithe-Jasper and H Rosner, *New J. Phys.*, **11**, 025023 (2009)
- <sup>102</sup> A S Sefat et al, *Phys. Rev. B*, **77**, 174503 (2008)
- <sup>103</sup> A S Sefat, A Huq, M A McGuire, R Jin, B C Sales, D Mandrus, *Phys. Rev. B*, **78**, 104505 (2008)
- <sup>104</sup> C Wang et al, *Europhys. Lett.*, **83**, 67006 (2008)
- <sup>105</sup> K Kasperkiewicz, J W G Bos, A N Fitch, K Prassides and S Margadonna, *Chem. Communication*, 707 (2009)

- <sup>106</sup> Z Ren, G Che, X Dong, J Yang, W Lu, W Yi, X Shen, Z Li, L Sun, F Zhou, Z Zhao, *Europhys. Lett.*, **83**, 17002 (2008)
- <sup>107</sup> M Rotter, M Tegel and D Johrendt, *Phys. Rev. Lett.*, **101**, 107006 (2008)
- <sup>108</sup> G F Chen, Z Li, G Li, W Z Hu, J Dong, J Zhou, X D Zhang, P Zheng, N L Wang and J L Luo, *Chin. Phys. Lett.*, **25**, 3403 (2008)
- <sup>109</sup> A S Sefat, R Jin, M A McGuire, B C Sales, D J Singh and D Mandrus, *Phys. Rev. Lett.*, **101**, 117004 (2008)
- <sup>110</sup> N Kumar, R Nagalakshmi, R Kulkarni, P L Paulose, A K Nigam, S K Dhar and A Thamizhavel, arxiv:0810.0848v1 (2008)
- <sup>111</sup> G Cao, C Wang, Z Zhua, S Jiang, Y Luo, S C Z Ren, Q Tao, Y Wang and Z Xu, arxiv:0807.1304v2 (2008)
- <sup>112</sup> L J Li, Q B Wang, Y K Luo, H Chen, Q Tao, Y K Li, X Lin, M He, Z W Zhu, G H Cao and Z A Xu, arxiv:0809.2009v1 (2008)
- <sup>113</sup> P Quebe, L J Terbue, W Jeitschko, *J. Alloys Compound.*, **302**, 70 (2008)
- <sup>114</sup> C Krellner, N Caroca-Canales, A Jesche, H Rosner, A Ormeci and C Geibel, *Phys. Rev. B*, **78**, 100504(R) (2008)
- <sup>115</sup> K R Andress and E Alberti, *Z. Metallkunde*, **27**, 126 (1935)
- <sup>116</sup> M A McGuire et al., (unpublished document)
- <sup>117</sup> Y P Feng, A Jin, D Finotello, K A Gillis and M H W Chan, *Phys. Rev. B*, **38**, 7041 (1988)
- <sup>118</sup> M E Reeves, T A Friedmann and D M Ginsberg, *Phys. Rev. B*, **35**, 7202 (1987)
- <sup>119</sup> M Hiroi, H Sato, M Sera and N Kobayashi, *Solid State Communication*, **92**, 579 (1994)
- <sup>120</sup> G Triscone and A Junod, *Bismuth-Based High-Temperature Superconductors*, edited by H Maeda and K Togano, Marcel Dekker, New York, pp.33-74,1996
- <sup>121</sup> S L Drechsler et al., *Physica (Amsterdam) B*, **329**, 1352 (2003)

## Vijayalakshmi Varadarajan

### Personal Details

**Date of Birth:** 11<sup>th</sup> Jan 1979

**Place of Birth:** Chennai, India

### Education

**Ph.D. (Physics)**, University of Kentucky, Lexington, KY, USA, Dec 2009 (Expected)

*Thesis:* Specific heat measurements on strongly correlated electron systems

*Advisor:* Dr. Joseph W Brill, Professor in Physics, University of Kentucky, KY, USA

**M.S. (Physics)**, University of Kentucky, Lexington, KY, USA, Dec 2006

**M.Sc. (Physics)**, Pondicherry University, Pondicherry, PY, India, May 2001

**B.Sc. (Physics)**, University of Madras, Chennai, TN, India, May 1999

### Professional Experience

**Graduate Research Assistant**, Low Dimensional Materials Lab, 2005-2009

*Advisor:* Dr. Joseph W Brill, Professor in Physics, University of Kentucky, Lexington, USA

**Graduate Teaching Assistant**, 2003-2007

Department of Physics and Astronomy, University of Kentucky, Lexington, USA

**Junior Research Fellow**, Space Physics Lab (A unit of Indian Space Research Organization), 2001-2003

*Supervisor:* Dr. Sridharan, Director, Space Physics Laboratory, Vikram Sarabhai Space Center, Thiruvananthapuram, India

**Visiting Research Student**, Inter-University Center for Astronomy and Astrophysics, 2000

*Supervisor:* Dr. Thanu Padmanabhan, IUCAA, Pune, India

### Academic Awards/Honors

- Graduate Research and Teaching Assistanships, Department of Physics and Astronomy – include Kentucky Graduate Scholarship by University of Kentucky, Lexington, KY, USA, 2003-2009
- Huffacker Travel Scholarship, University of Kentucky, Lexington, KY, USA, 2007
- Domestic Travel Student Support Award, University of Kentucky, Lexington, KY, USA 2007
- SNS-HFIR Users Meeting Scholarship, Oak Ridge National Laboratory, Oak Ridge, USA, 2005
- Junior Research Fellowship, ISRO, Department of Space, Government of India, 2001-2003

### Professional Affiliations

American Physical Society (APS)

### Publications

1. **V Varadarajan**, S Chikara, V Durairaj, XN Lin, G Cao, and J W Brill – *Specific Heat of  $(Ca_{(1-x)}Sr_x)_3Ru_2O_7$  – **Solid State Communications 141, 402 (2007)***
2. M Angst, P Khalifah, R P Hermann, H J Xiang, M H Whangbo, **V Varadarajan**,

J W Brill, B C Sales, D Mandrus – Charge Order Superstructure with Integer Iron Valence in  $\text{Fe}_2\text{OBO}_3$  – *Phys. Rev. Lett.* **99**, 086403 (2007)

3. M A McGuire, A D Christianson, A S Sefat, B C Sales, M D Lumsden, R Jin, E A Payzant, D Mandrus, Y Luan, V Keppens, **V Varadarajan**, J W Brill, R P Hermann, M T Sougrati, F Grandjean, G J Long – Phase transitions in  $\text{LaFeAsO}$ : Structural, magnetic, elastic and transport properties, heat capacity and Mossbauer spectra – *Phys. Rev. B* **78**, 094517 (2008)

#### Presentation in Seminars/Conferences

1. **V Varadarajan**, S Chikara, V Durairaj, X N Lin, M Angst, G Cao, J W Brill – ‘Specific heat measurements on novel electronic crystals’– *The 4<sup>th</sup> Annual Departmental Research Poster Session, University of Kentucky, Lexington, USA, 18 Aug 2007*– Poster
2. **V Varadarajan**, S Chikara, V Durairaj, XN Lin, G Cao, and JW Brill – ‘Specific Heat of  $(\text{Ca}_{1-x}\text{Sr}_x)_3\text{Ru}_2\text{O}_7$  single crystals’ – *APS March Meeting, Denver, CO, 6-9 Mar 2007*
3. **V Varadarajan** – ‘Reduction of spin ordering: ac-calorimetry measurements on  $(\text{Ca}_{1-x}\text{Sr}_x)_3\text{Ru}_2\text{O}_7$  single crystals’ – *Graduate Student Post-Doc Seminar, Department of Physics and Astronomy, University of Kentucky, Lexington, USA, 05 Dec 2006*
4. **V Varadarajan** – ‘ac-calorimetry measurements on Mott-like  $\text{Ca}_3\text{Ru}_2\text{O}_7$  and charge ordered  $\text{Fe}_2\text{OBO}_3$ ’ – *Condensed Matter Seminar, Department of Physics and Astronomy, University of Kentucky, Lexington, KY, 28 Nov 2006* – Invited
5. X N Lin, V Durairaj, Z X Zhou, S Chikara, A Douglass, **V Varadarajan**, V A Bondarenko, J W Brill, P Schlottmann, G Cao – ‘Observation of oscillatory magnetoresistance periodic in  $1/B$  and  $B$  in  $\text{Ca}_3\text{Ru}_2\text{O}_7$ ’ – *APS March Meeting, Baltimore, MD, 13-17 Mar 2006*
6. S Mukhopadhyay, J N Orce, S Choudry, **V Varadarajan**, A Kumar, M T McEllistrem, S W Yates – ‘Search for multi phonon and mixed symmetry states in  $^{127}\text{I}$ ’ – *Proceedings of the Twelfth International Conference on Capture Gamma-ray Spectroscopy and Related Topics (CGS12), Notre dame, IN, 4-9 Sept 2005* – Poster
7. S N Choudry, J N Orce, S Mukhopadhyay, **V Varadarajan**, D Bandyopadhyay, A Kumar, S R Leshner, S W Yates, M T McEllistrem – ‘Study of charge symmetry in  $^{18}\text{O}$ ’ – *Proceedings of the Twelfth International Conference on Capture Gamma-ray Spectroscopy and Related Topics (CGS12), Notre dame, IN, 4-9 Sept 2005*
8. T K Pant, D Tiwari, V Varadarajan, K S Subbarao, C V Devasia, R Sridharan, R Sekar – ‘Daytime optical and radar measurements of the equatorial MLTI region: New results’ – *34<sup>th</sup> Committee on Space and Research (COSPAR) Scientific Assembly, The Second World space Congress, Houston, TX, 10-19 Oct 2002*
9. **V Varadarajan** – ‘ Daytime measurements on airglow emissions using

multiwavelength daytime photometer' – *Colloquium, Space Physics Lab, Vikram Sarabhai Space Research Center, Thiruvananthapuram, India, 6 Sep 2002*

10. **V Varadarajan** – 'Perturbative effect on stars' – *Colloquium, Raman School of Physics, Pondicherry University, Pondicherry, India, 6 Aug 2000 – Invited*

11. **V Varadarajan** – 'Galactic Dynamics' – *Seminar, Vacation Students Programme, Inter-University Center for Astronomy and Astrophysics, Pune, India, 5 Jul 2000*

### **Unpublished Theses**

- **Vijayalakshmi Varadarajan**, 'Specific heat measurements on strongly correlated electron systems' - Advisor: Dr. J W Brill, Director of Graduate Studies, Department of Physics and Astronomy, University of Kentucky, Lexington, KY 40508, Dec 2009 (Proposed) - Ph.D dissertation
- **Vijayalakshmi Varadarajan**, 'Chandra observations on NGC 7582: AGN-Starburst connection' - Advisor: Dr. Nancy A Levenson, Professor in Physics, University of Kentucky, Lexington, KY 40508, May 2004 – unpublished document
- **Vijayalakshmi V**, 'Studies on Semiconductor Lasers' - Advisor: Dr. Mohan, Head of Department in Physics, Pondicherry University, Pondicherry, India - M.Sc dissertation, May 2001